2013

# Development Of Thulium Fiber Lasers For High Average Power And High Peak Power Operation

Robert Sims
*University of Central Florida*

# DEVELOPMENT OF THULIUM FIBER LASERS FOR HIGH AVERAGE POWER AND HIGH PEAK POWER OPERATION

by

ROBERT ANDREW SIMS
B.S. Samford University, 2007
M.S. University of Central Florida, 2009

A dissertation submitted in partial fulfillment of the requirements
for the degree of Doctor of Philosophy
in the College of Optics and Photonics
at the University of Central Florida
Orlando, Florida

Spring Term
2013

Major Professor: Martin Richardson

# ABSTRACT

High power thulium fiber lasers are useful for a number of applications in both continuous-wave and pulsed operating regimes. The use of thulium as a dopant has recently gained interest due to its large bandwidth, possibility of high efficiency, possibility of high power and long wavelength ~1.8 – 2.1 μm. The longer emission wavelength of Tm-doped fiber lasers compared to Yb- and/or Er-doped fiber lasers creates the possibility for higher peak power operation due to the larger nonlinear thresholds and reduced nonlinear phase accumulation.

One primary interest in Tm-doped fiber lasers has been to scale to high average powers; however, the thermal and mechanical constraints of the fiber limit the average power out of a single-fiber aperture. One method to overcome the constraints of a single laser aperture is to spectrally combine the output from multiple lasers operating with different wavelengths into a single beam. In this thesis, results will be presented on the development of three polarized 100 W level laser systems that were wavelength stabilized for SBC. In addition to the development of the laser channels, the beams were combined using bandpass filters to achieve a single near diffraction-limited output.

Concurrently, with the development of high average power systems there is an increasing interest in femotosecond pulse generation and amplification using Tm- doped fiber lasers. High peak power sources operating near 2 μm have the potential to be efficient pump sources to generate mid-infrared light through supercontinuum generation or optical parametric oscillators. This thesis focuses on the development of a laser system utilizing chirped pulse amplification (CPA) to achieve record level energies and peak powers for ultrashort pulses in Tm-doped fiber.

A mode-locked oscillator was built to generate femtosecond pulses operating with pJ energy. Pulses generated in the mode-locked oscillator were limited to low energies and contained spectral modulation due to the mode-locking mechanism, therefore, a Raman-soliton self-frequency shift (Raman-SSFS) amplifier was built to amplify pulses, decrease the pulse duration, and spectrally clean pulses. These pulses were amplified using chirped pulse amplification (CPA) in which, limiting factors for amplification were examined and a high peak power system was built. The primary limiting factors of CPA in fibers include the nonlinear phase accumulation, primarily through self-phase modulation (SPM), and gain narrowing. Gain narrowing was examined by temporally stretching pulses in a highly nonlinear fiber that both stretched the pulse duration and broadened the spectrum. A high peak power CPA system amplified pulses to 1 μJ energy with 300 fs compressed pulses, corresponding to a peak power >3 MW. High peak power pulses were coupled into highly nonlinear fibers to generate supercontinuum.

To my family,

# ACKNOWLEDGMENTS

I would like to thank my advisor Dr. Martin Richardson for his guidance that has been integral to development of the thulium fiber laser program, as well as the opportunity to be involved in this program. I would like to thank Dr. Larry Shah, for the almost daily guidance and advice of the work presented in this thesis. Thanks to my committee members Dr. Chow, Dr. Delfyett, and Dr. Schülzgen for the guidance throughout my candidacy, proposal, and dissertation process.

I would like to acknowledge contributions to the experimental work presented in this thesis. Within the Laser Plasma laboratory I acknowledge, Dr. Timothy McComb, Dr. Lawrence Shah, Pankaj Kadwani, and Christina Willis. I would like to thank members of the fiber optics laboratory within CREOL, namely Clémence Jollivet and Peter Hofmann for the hours of discussion and use of their groups' splicer and other equipment that was both integral to the building of systems and characterization of fibers. I would like to acknowledge the countless of hours of work with Soroush Shabahang to generate Mid-IR supercontinuum. I would like to acknowledge the work of our collaborators and friends and Clemson University, Dr. Eric Johnson, Dr. Menelaos Poutous, Zachary Roth, and Aaron Pung for the development of components used in this work.

I would also like to thank the members of the Laser and Plasma Laboratories for their friendship and assistance for the past 5 years. These individuals include: Dr. Timothy McComb, Dr. Michael Hemmer, Dr. Troy Anderson, Dr. Ji Yeon Choi, Dr. Rob Bernath, Dr. Simi George, Nick Barbieri, Mattieu Baudelet, Nathan Bodnar, Josh Bradford, Chris Brown, Christian Gaida,

Martin Gebhardt, Andrew Houseman, CheonHa Jeon, Pankaj Kadwani, Reuvani Kamtaprasad, Khan Lim, Yuan Liu, Erik McKee, Mark Ramme, Omar Rodriguez, Alex Sincore, Vikas Sudesh, John Szilagyi, Tony Teerawattanasook, Andreas Vaupel, Ben Webb, Matt Weidman, and Christina Willis. A acknowledge the work and discussions with Richard Zotti, and his guidance in working in the machine shop. His guidance in the machine shop was integral to the development of all the laser systems presented in this dissertation. Thank you to the entire faculty, students at CREOL for the professional learning environment and friendships I have developed.

TABLE OF CONTENTS

# LIST OF FIGURES

# LIST OF TABLES

# LIST OF ABBREVIATIONS

| | |
|---|---|
| ASE | Amplified spontaneous emission |
| CBG | Chirped Bragg grating |
| CR | Cross relaxation |
| CW | Continuous wave |
| DCF | Double-clad fiber |
| DIAL | Differential absorption LIDAR |
| EOM | Electro-optic modulator |
| ETU | Energy transfer up-conversion |
| FBG | Fiber Bragg grating |
| FWHM | Full width at half maximum |
| GMRF | Guided mode resonance filter |
| GVD | Group velocity dispersion |
| HWP | Half wave plate |
| LIBS | Laser induce breakdown spectroscopy |
| LMA | Large mode area |
| MFA | Mode field adaptor |
| MFD | Mode field diameter |
| MOF | Micro-structured optical fiber |
| MOPA | Master Oscillator power amplifier |
| NA | Numerical aperture |
| NLSE | Nonlinear Schrödinger equation |
| NPE | Nonlinear polarization evolution |
| OPO | Optical parametric oscillator |
| OSA | Optical spectrum analyzer |
| PCF | Photonic crystal fiber |
| PECVD | Plasma-Enhanced chemical vapor deposition |
| PER | Polarization extinction ratio |
| PM | Polarization maintaining |

| | |
|---|---|
| QCL | Quantum cascade laser |
| QWP | Quarter wave plate |
| SA | Saturable absorber |
| SBC | Spectral beam combining |
| SBS | Stimulate Brillouin Scattering |
| SMF | Single mode fiber |
| SPM | Self-phase modulation |
| SRS | Stimulated Raman scattering |
| SSFS | Soliton Self frequency shift |
| SWCNT | Single walled carbon nanotubes |
| TEC | Thermal expansion of the core |
| TFB | Taper fiber bundle |
| TOD | Third order dispersion |
| UHNA | Ultra-high numerical aperture |
| USP | Ultra short pulse |
| VBG | Volume Bragg grating |
| ZDW | Zero dispersion wavelength |

# CHAPTER 1: INTRODUCTION

## 1.1 Description and Advantages of Fiber Lasers

Advancements in fiber lasers have led to high-power laser systems that are capable of high average powers, generation of pulses ranging from fs to μs, and amplification of these pulses to GW peak powers. The most noted advantages of fiber lasers are the ability to produce robust, compact, systems with diffraction-limited beam quality while operating with high wall plug efficiencies.

The fiber laser geometry offers many important attributes making it a useful laser medium for many demanding applications. One main feature the fiber geometry offers is the ability to extract high powers in diffraction-limited beams with minimal thermal management relative to solid-state lasers. Moreover, beam quality of the fiber based system is generally insensitive to thermal lensing. Robust fiber systems can be built in small form factors and can be isolated from the environment through all fiber integration of components.

Fiber lasers ease thermal management because the large surface area to volume ratio. While the glass hosts of fibers are poor thermal conductors, the heat is distributed along the length, facilitating heat removal and reducing thermal gradients, making fibers lasers superior thermally to conventional solid-state systems. Three level, and quasi-three level dopants generally operate more efficiently when cooled and the fiber geometry allows for compact and simple cooling through air convection, by wrapping the fiber around cooled mandrels, or by submersion in water baths if needed.

### *1.1.1 Confinement in the Core*

A fiber laser contains a doped core region with a higher index of refraction than the surrounding cladding region, so that light is confined in the fiber through total internal reflection. By designing the fiber correctly, primarily the core size and refractive index step, single transverse mode laser operation is possible and robust. With the mode defined by the fiber waveguide, it is possible to use relatively long doped sections to obtain large single-pass gain and high laser efficiency. Because the fiber properties can be designed to force $LP_{01}$ operation of the laser, many applications requiring single mode operation benefit through the use of fiber geometry. The use of single mode beams is integral to both remote sensing and directed energy applications where laser power needs to be transmitted over long distances. Laser material processing applications also benefit from single mode operation, particularly when small and clean features are needed.

Many applications demand high average powers in the continuous-wave (CW) regime and higher energies/peak powers in pulsed regimes; however fiber core size is a limiting factor. The core size and numerical aperture determine the mode area of light within the fiber, which in term determines the threshold for damage and nonlinear effects. In order to overcome these issues much research is being explored to increase the core size to large mode areas while maintaining the single mode beam quality of the output light.

#### 1.1.1.1 Optical Fiber Theory

An optical fiber is a step index waveguide commonly with circular symmetry and is defined as such mathematically. Other core geometries are possible but for this dissertation

circularly symmetric fibers will be used. Both slab and circular waveguides are governed by total internal reflection. While this definition does not give information about the modes of light that are able to propagate in the fiber it does give an important physical picture that leads to concepts of the numerical aperture and V number, which are integral to discussing fibers. The numerical aperture (NA) of a waveguide is defined as:

$$NA = Sin(\theta_0) = \sqrt{n_2^2 - n_1^2} \qquad (1)$$

where $n_2$ is the index of the core and $n_1$ is the index of the cladding. The term, $\theta_0$, describes the maximum angle outside the fiber that can excite a guided mode within the fiber. From the electromagnetic treatment and the definition of the NA, a normalized frequency or V number can be derived. The V number is defined as

$$V = \frac{2\pi a}{\lambda} NA \qquad (2)$$

where $a$ is the radius of the fiber. The V-number is used to determine the approximate number of modes that are in a fiber. Step index fibers with a V parameter < 2.405 are considered single mode operation.

The full electromagnetic derivation of how light propagates and forms guided modes in a fiber can be found in many texts [1], thus a full reiteration is not necessary here. However, the results of this derivation are important to understanding the way in which light propagates in a fiber especially for scaling to large mode areas for high power laser generation.

*1.1.1.1.1 Large Mode Area Fibers*

The increase in fiber powers is directly related to the expansion of fiber core and optimizing pump geometries. The first demonstrations of fiber lasers used flash lamps for pumping, however this was a non-optimal solution due to lack of stored energy compared to other solid state systems [2,3]. The next advancement in fiber laser technology was direct diode pumping of single mode fiber. These improvements were pushed by the telecommunications industry, but relied upon matching single mode diodes to the single mode fiber, thus limiting power due to limited diode technology [4]. The major advance in power scaling of fiber lasers appeared with the advent of the double clad fiber (DCF) in 1988. In this geometry the cladding region is surrounded by a low refractive index region allowing for guidance of multi-mode pump light while signal light in the core is single-mode [5]. The DCF architecture was fundamental to enabling increases in core size and the advent of large mode area (LMA) fibers.

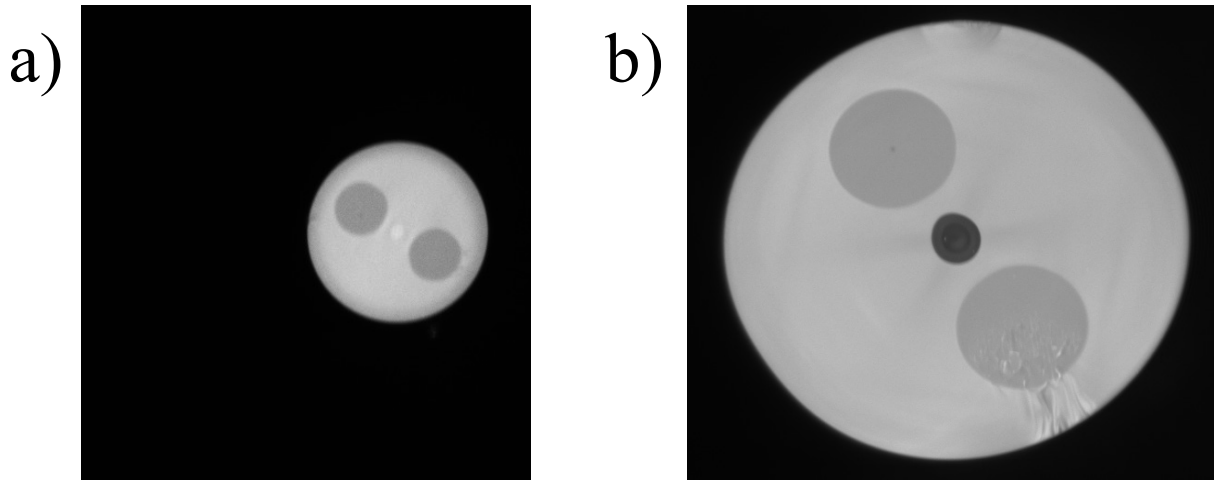


*Figure 1: a) Image of a PM 10/130 single mode fiber. b) Images of a LMA PM 25/400 fiber*

Figure 1 a) and b) show images of both single-mode and LMA fibers that will be used in this thesis. In the case of this specific single-mode fiber it is a double-clad fiber allowing for cladding pumping. Single-mode fiber is designed such that the core diameter and NA only allow the $LP_{01}$ mode to propagate by ensuring that $V < 2.405$ where V is defined in Equation (2). The use of single-mode fiber offers advantages when developing components in fiber because only the fundamental mode is excited. However, many high power laser applications are limited by confinement in the relatively small mode area of the fiber, thus scaling to larger mode field diameters is necessary. Equation (2) highlights the parameters that can be adjusted to scale the core diameter and maintain fundamental mode operation in conventional step index fiber. The two parameters are the NA and the wavelength. The wavelength will typically be fixed by the laser source, but the V-parameter shows that longer wavelengths will allow fundamental mode propagation for larger core sizes due to the inverse relationship. Therefore, the primary method used is to minimize the NA. In LMA fibers typically a few modes are allowed to propagate but due to bending loss higher order modes can have larger values of loss than the fundamental mode. In the fibers presented in Figure 1 the parameters are as follows: a) has a 10 μm core with a 0.15 NA therefore V=2.355 at 2000 nm and b) has a 25 μm core diameter with a 0.09 NA and V = 3.53.

Many methods of scaling fiber core size are being explored to avoid fiber damage and nonlinear effects such as stimulated Brillouin scattering and stimulated Raman scattering, while still maintain single mode operation. Initially, using conventional fiber geometries small NAs in the core region, tailored dopants, and index profiles were used to excite the gain in the lowest order mode. Other methods of fiber coiling in conjunction with small NAs helps strip weakly

guided higher order modes in the fiber ensuring single mode operation. These techniques can be used for core diameters up to ~ 30 μm for operation at ~1 μm wavelength; however more advanced fiber geometries are needed.

One of the most prominent methods for scaling the core size in recent years is the use of photonic crystal fiber (PCF) [6,7]. In these fibers, the index of refraction in the cladding region is modified using microstructures, such as air holes or glass with different index than the rest of the cladding, reducing the NA of the core. Lower core NA enables proportionately larger core diameter capable of guiding the lowest order mode, but shedding any higher order modes. Presently, PCFs with single mode operation at 1 μm have core diameters greater than 70 μm with a maximum up to 140 μm [8–10]. While PCFs can offer endlessly single mode operation there are drawbacks for these systems compared to conventional fibers.

Conventional fiber allows compact, robust operation because multiple components in a system can be spliced together to create all-fiber systems. PCFs on the other hand are not as easily manipulated and particular care needs to be taken during splicing and cleaving. Another drawback that needs to be taken into account is the bend loss of the PCF, many systems need to operate in a straight fiber or rod, thus the compactness and robustness of fibers is no longer an advantage [11,12] .

Other approaches to scaling the fiber core diameter are being explored. These include chirally coupled core [13], gain guided index anti-guided fibers [14], and leakage-channel fibers [15]. Due to the lack of technological maturity these fiber designs are still being developed.

### *1.1.2 Passive Components*

One of the primary advantages of using optical fiber to build and design lasers is in the ability to build robust systems that do not have the need for optical alignment. The key to systems of this nature is to produce optical components built into packages that take advantage of the fiber geometry. As fiber based components improve, the quality and stability of fiber laser systems have and will continue to improve. Advancements in the ability to make high quality components could parallel developments that improved lasers in general with the improvement of semiconductor laser diodes. In this section a few fiber components that will be used later in this thesis will be discussed; namely, pump combiners, mode field adaptors, and fiber isolators.

#### 1.1.2.1 Pump Combiners

Traditional methods of pumping high power fiber lasers include the use of free space telescopes to couple light into a fiber. One example would be the use of a high brightness pump diode with a 100 μm multimode delivery fiber and coupling light using a 4 f telescope with matching focal length lenses into a 125 μm DCF. One major drawback to this method of free space coupling is there are alignment tolerances using free space coupling. Thus, the use of fiber fused components to deliver pump light to an active fiber is an important step in the development of high power fiber lasers. To counter two of the drawback of the free space coupling, multiple pump diodes can be fused into a single fiber that delivers the pump light, which can then be splice to a double-clad fiber without free space alignment issues.

Two types of fused fiber components exist for the delivery of high-power multi-mode pump light. These components will be denoted as N × 1 for a fused fiber bundle that only

delivers only pump light and has no signal feed through and a (N+1) × 1 where the fused fiber bundle delivers pump light and has a feed-through for the signal.

One method for fabrication of the N × 1 is to prepare multimode fiber by removing the polymer coating from the fiber then inserting the fibers into a hollow capillary and fusing the structure. Once fused, this structure will be tapered to match the outside diameter of a DCF then cleaved and spliced. Brightness must be conserved in order for the pump light to be guided with the DCF [16]. Mathematically this can be described as follows,

$$\phi_b NA_b \leq \phi_0 NA_0 \qquad (3)$$

where $\phi_b$ is the diameter of the fiber bundle, $NA_b$ is the largest NA of the input fiber, $\phi_0$ is the diameter of the output fiber core, and $NA_0$ is the NA of the output fiber core [16].

The (N+1) × 1 type of TFB is used extensively in the work later in this thesis. In this design the central multimode fiber is replaced with a passive signal fiber, therefore, signal light can be transmitted through the device either to or from active fiber. Due to the complexity of making (N+1) × 1 pump combiners, we have commercially purchased such devices rather than fabricating our own [17].

Two primary types of TFB used in this dissertation are (2+1) × 1 with 100 μm multimode pumps and a 10/130 PM signal feed through; and (6+1) × 1, with 200 μm multimode pumps with a 25/400 μm PM signal feed through fiber. The (2+1) × 1 pump combiners are able to combine up to 100 W with <0.5 dB insertion loss. The 6+1:1 pump combiners are can couple 300 W with

a manufactured specified pump coupling transmission of 85%, but a measured value closer to 75%.

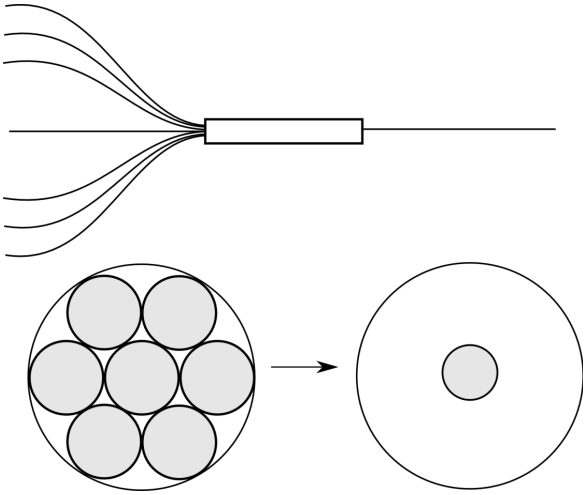

*Figure 2: Schematic showing the cross-section of a typical taper fiber bundle [16].*

1.1.2.2 Mode Field Adaptors

As discussed previously one of the major advancements in the development of both high average and high peak power fiber lasers was the advent of the LMA fiber. Conventional core-clad structures can increase the core diameter and reduce the core NA to maintain guidance, although doing this may increase the number of transverse modes that are allowed to propagate in the fiber. In order to compensate for the transverse mode excitation fibers can be bent to strip higher order modes. However fundamental mode operation can be achieved by launching strictly the fundamental mode into the LMA fiber [18]. In systems where there are dissimilar fibers, both SMF and LMA, it becomes necessary to launch light from the fundamental mode of the SMF to the fundamental mode of the LMA. With free-space optics one must match the mode-field diameter using the correct lens pairs or telescope systems, sometimes the optimal solutions

are not available. Fiber components on the other hand, can be fabricated to achieve low loss and properly match the MFD and maintain fundamental mode operation.

These components are known as mode field adaptors (MFA), and depending on the parameters of the dissimilar fibers there are numerous ways to fabricate these MFA. One widely used technique when splicing dissimilar SMFs is to use thermal expansion of the core (TEC) or thermal diffusion of the core [19]. A typical use of this method would be splicing of ultra-high numerical aperture (UHNA) to a more typical SMF. These fibers differ because the fiber geometry of the UHNA can have NA > .3 and core radius diameters < 5 μm whereas a SMF fiber can have an NA = 0.14 and a core diameter of 8.2 μm (SMF-28E). Therefore the geometries do not match and directly splicing the two can cause high splice losses.

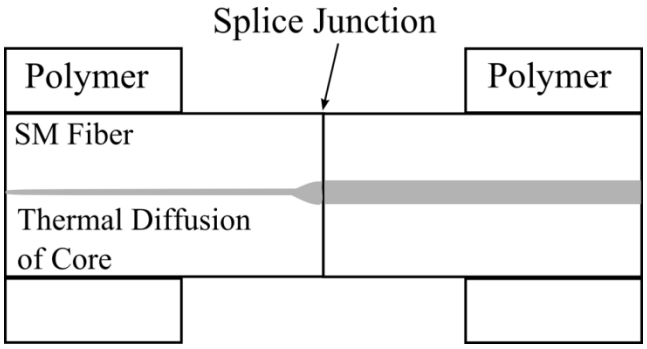


*Figure 3: Drawing of a mode field adaptor fabricated with thermal expansion of the core for fibers with similar cladding diameters [20].*

This method of TEC does not work with MM fibers because the thermal diffusion process that leads to mode size reduction then mode field expansion [20]. One possibility to create a low loss junction between both SMF and LMA fiber is to taper the LMA fiber and splice to the SMF [21]. However, using this method the MFD of the two fibers may not match. As is shown in [21], the insertion loss is still greater than 1 dB for a splice between a Corning SMF

HI1060 and a LMA with a 25 μm diameter and a 0.06 NA. One method to overcome this is to combine the methods of tapering a fiber and using TEC of the core on another fiber. Using a combination of methods Faucher et, al. [20] have spliced a section of Corning 1060 and a 20 μm NA, 0.065 NA fiber with a low loss around 0.2 dB. Without using a MFA, the splicing of these fibers produced an 8.5 dB insertion loss and multimode-interference.

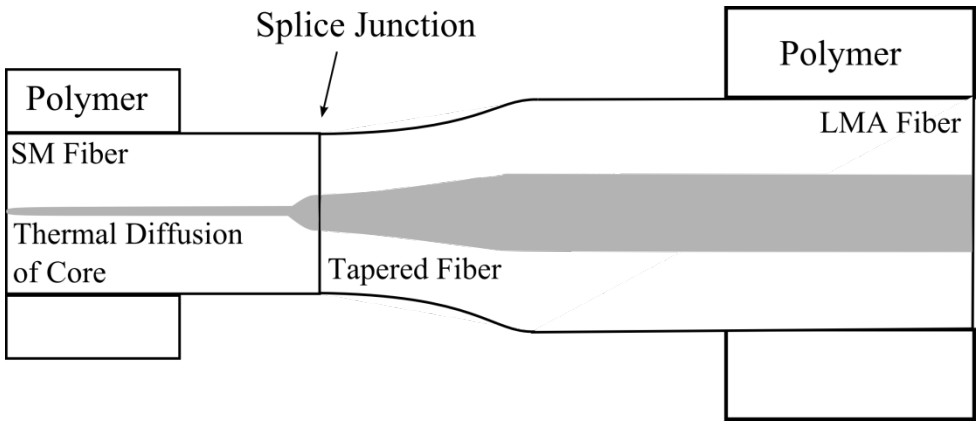


*Figure 4: Mode field adaptor drawing showing a mixture of TEC and the tapering of a larger cladding fiber [20].*

1.1.2.3 Optical Isolators

In high power amplifier systems as well as other laser system, it is desirable to maintain the parameters of the initial oscillator through the laser system. Due to feedback in fiber amplifier systems the gain possible in each stage is significantly limited without used of optical isolators because of degradation of the input signal. In order to prevent backward feedback Faraday materials are used to fabricate optical isolators. While optical isolators have been realized for > 30 years, fiber coupled isolators [22] for use at 2000 nm have been developed in the last < 5 years, therefore, the technology is relatively immature.

A diagram for a polarization sensitive fiber isolator is shown in Figure 5. This polarization sensitive isolator works by using optically anisotropic materials to walk each polarization into different planes. This polarized beam passes through the crystal and spatially walk-off the center line of the following fiber and is not back-coupled into the fiber.

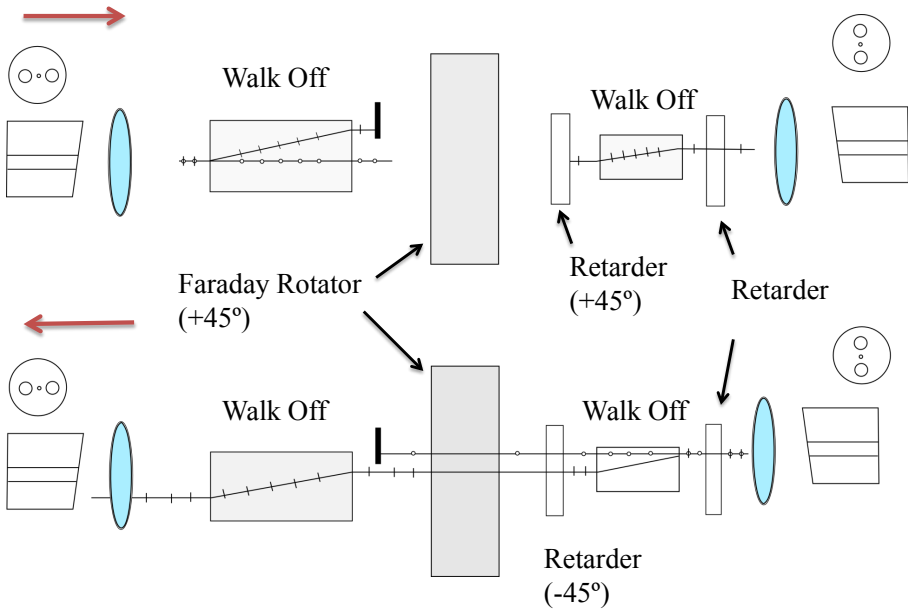


*Figure 5: Schematic of a polarization sensitive fiber isolator.*

### 1.2 Spectroscopic Properties of Thulium

The use of thulium doped silica fiber has increased over the past decade due to the advantageous properties of $SiO_2$, optimization of Tm into the glass matrix, and the unique properties of thulium as a dopant. Covalently bonded $SiO_2$ provides many well-known advantageous properties that make it an ideal host for high power lasers including: low refractive index, low nonlinearities, low thermal expansion coefficient, and large tensile strength. Another

important characteristic for $SiO_2$ is the multi-phonon absorption edge is > 2000 nm; therefore, the emission wavelengths of Tm fall within the transparency of $SiO_2$. While other glass types accept Tm as a dopant, the thermo-mechanical properties of these glasses do not allow for robust high power laser operation [23,24]. The upcoming sections will discuss the spectroscopic properties that Tm exhibits when doped into $SiO_2$ and the energy transfer processes that effect the efficiency of Tm as laser dopant.

### *1.2.1 Spectroscopic Properties*

The energy level diagram for thulium is shown in Figure 6, with the appropriate energy transfers diagramed. The relevant energy levels for the operation of Tm include the $^3H_6$, $^3F_4$, $^3H_5$, and $^3H_4$ where each level shows Stark splitting due to the insertion of the dopant into an amorphous host. Doping into the amorphous glass host causes inhomogeneous broadening of the doped ions causing a large bandwidth. In order to dope high concentrations of $Tm_2O_3$ into $SiO_2$ the glass must be doped with $Al_2O_3$ to increase the solubility of the rare earth ions [25]. Efficiency levels of codoping $Al^{3+}/Tm^{3+}$ have been measured, and concentration ratio exceeding 10 are important to facilitate high doping concentrations [26]; in turn, this increases the cross-relaxation process which will be discussed in the next section.

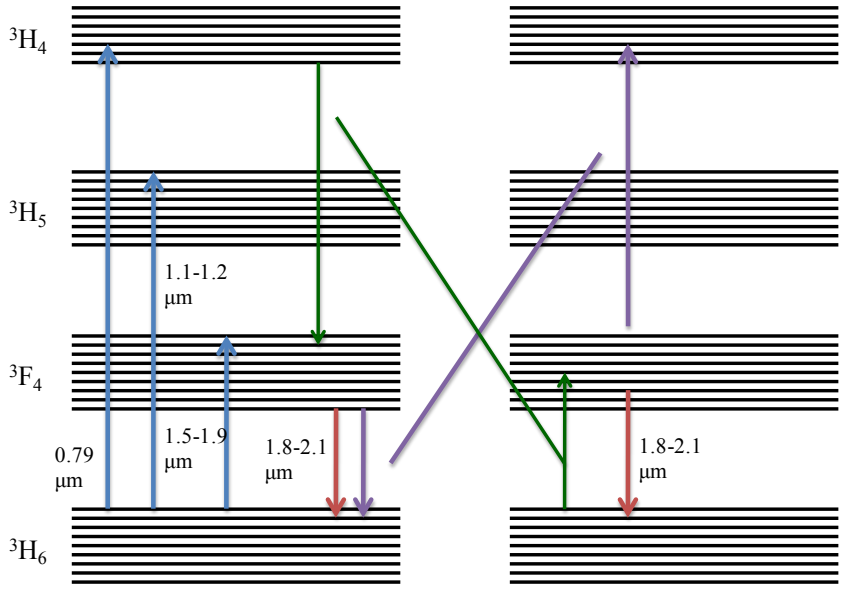


*Figure 6: Energy level diagram for adjacent Tm ions. Blue lines represent absorption, red represent emission; the green shows the cross-relaxation process, and purple diagrams energy transfer upconversion.*

In order to excite the laser transition in Tm, there are two primary transitions that can be excited depending on the pump wavelength. The primary emission occurs between the $^3F_4$ and $^3H_6$ Stark levels and produces emission ranging from 1.6 to 2.2 µm. This laser transition is a quasi-three level laser transition due to thermal population distributions within the ground state ($^3H_6$). However, emission from thulium at wavelengths greater than ~2020 nm acts as a quisi-four level transition because the sublevels of the ground state are not highly thermally populated near the top of the band. Due to the three-level nature of thulium and the thermal population distribution, there is a strong level of re-absorption of shorter wavelengths limiting the short wavelength operation in thulium.

Thulium has three potential options for pump bands centered near 790 nm, 1200 nm, and 1600 nm. However, the transition centered at 1200 nm needs mature pump technology and does not produce an efficient laser transition. Transitions excited between 1.5-1.9 µm occur as "in-

band" pumping and have the possibility to produce efficient lasers due the small quantum defect pumping. In this pumping scheme ground state electrons from the $^3H_6$ level are excited to the top of the $^3F_4$ manifold where they thermally decay to the lower energy portion of the $^3F_4$ manifold where the laser transition occurs. While pumping in the region has an advantage with regards to lower quantum defect and less thermal stress than with 790 nm pumping the number of high brightness pump sources is limited. The most effective laser to use in the region is an Er:Yb fiber laser operating at 1550-1570 nm. The use of Er:Yb is important for core pumping short sections of fiber. Using this technique the absorption coefficient is much higher than for double-clad pumping, promoting the use of short lengths of fiber for short wavelength applications or in short pulse generation where the length of fiber is important.

The primary method of pumping Tm to lase at 2000 nm is using already mature diode lasers operating at 790 nm based upon AlGaAs diode technology developed for 808 nm diodes. This pump process can provide extremely efficient pumping with a cross-relaxation process that will be highlighted later. High brightness diodes operating at 790 nm are able to be fabricated with high wall plug efficiencies and MM delivery fibers as small as 100 μm thus providing an optimal source for cladding pumping. Presently using multiple 790 nm diodes Tm based systems have been amplified to powers up to 1 kW [27]. While it is possible to generate high efficiencies with 790 nm pumping, typical values maximize around 60% efficiency thus Tm fiber systems generate high heat and must be thermally managed. Resonant pumping is certainly an attractive alternative, as heat generation could be in high average power systems. This is one force driving the development of holmium-doped fiber lasers emitting at ~2.1 μm and pumped by Tm:fiber lasers at 1.9 μm.

Figure 7 shows the cross-section of emission and absorption for Tm. The graph highlights the pump wavelengths. Given the broad emission bandwidth and output wavelength firmly in the eye-safe regime and tunable from 1900-2100 nm Tm:fiber is highly attractive for the generation and amplification of fs pulses.

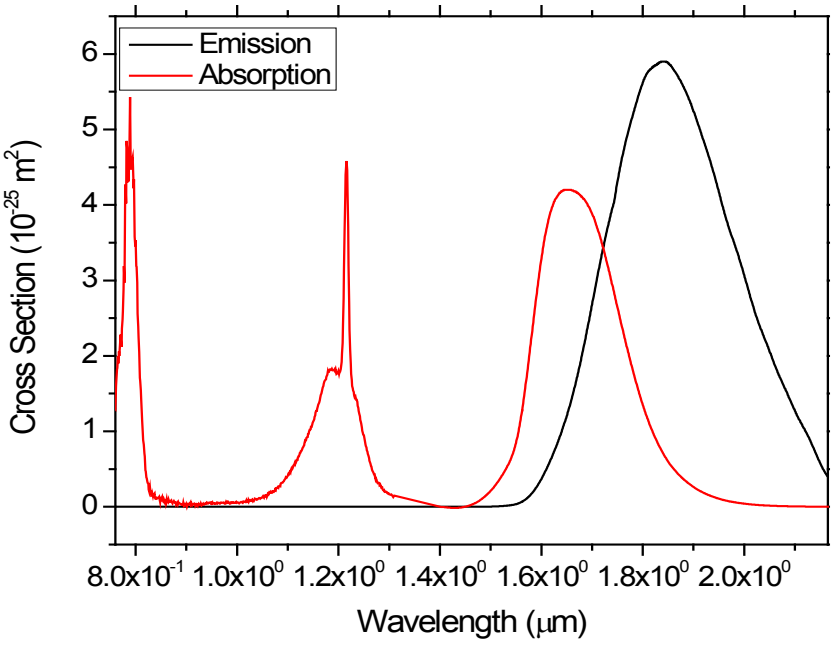


*Figure 7: Absorption and Emission cross section of Tm:fiber [28].*

### *1.2.2 Cross Relaxation*

Cross-Relaxation (CR) is an energy transfer processes in thulium that is the basis for generating highly efficient Tm:fiber lasers while pumping with at 790 nm. Without the CR process pumping at 790 nm, the quantum defect would be ~40 %. The CR process effectively increases the quantum efficiency 200%, thus theoretically enabling slope efficiencies up to 80% [29]. Effectively two signal photons can be emitted for a single pump photon, via interaction of two thulium ions that share energy. In CR this sharing of energy excites a ground state electron to an excited state as shown in Figure 6.

### *1.2.3 Energy Transfer Upconversion*

Energy transfer upconversion (ETU) is a similar process to CR; however instead of exciting a ground state electron to an excited, state the energy transfer occurs between an already excited electron to an even higher energy state. In Tm, two ETU process are possible and can be labeled using the transitions $^3F_4$, $^3F_4 \rightarrow {}^3H_6$, $^3H_4$ (ETU1) and $^3F_4$, $^3F_4 \rightarrow {}^3H_6$, $^3H_5$ (ETU2). Due the exothermic nature of ETU2 it is more probable than ETU2 [25,29].

## 1.3 Applications of Thulium Fiber Lasers

### *1.3.1 Atmospheric Propagation*

Light covering the wavelength range from 1.8 - 2.1 μm is attractive for many applications associated with long-range atmospheric transmission and/or atmospheric sensing, due to spectral windows providing high atmospheric transmission as well as strong molecular vibrational from atmospheric water vapor and/or $CO_2$. Light generated at these wavelengths is in the 'eye-safe' region ($\lambda > 1.4\mu m$) and safer for many applications where human bystanders may be exposed to specular reflection or scattering. Applications directly related to transmission in the atmosphere include free space communications, directed energy, laser induced breakdown spectroscopy (LIBS), differential absorption LIDAR (DIAL), and chemical sensing applications [5-8]. Figure 8 is a simulation of the atmospheric transmission around 2 μm using MODerate resolution atmospheric TRANmission (MODTRAN).

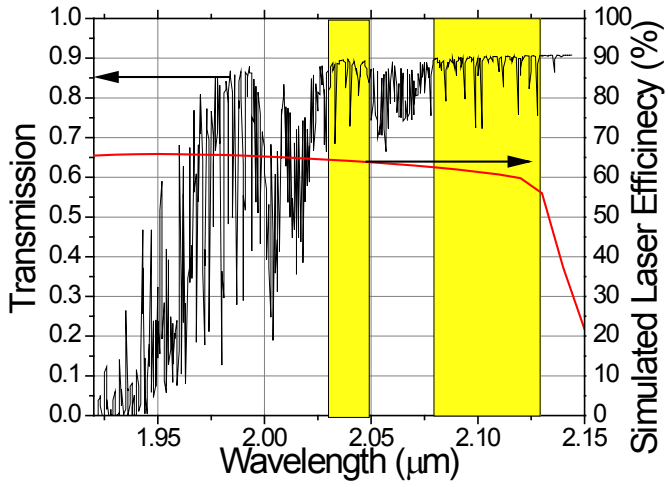


*Figure 8: MODTRAN simulation of atmospheric transmission near 2μ m. The red curve shows computer simulated efficiencies of Tm. The yellow bands mark areas of highest transmission .*

### *1.3.2 Mid-IR Supercontinuum Generation*

The use of broadband Mid-IR light (3-10 μm) light opens up many new application areas in medical, sensing, and defense related applications. Presently both quantum cascade lasers (QCL) [30,31] and optical parametric oscillators (OPO) are viable sources for generating light in the Mid-IR spectral region, but there are some drawbacks. Typically OPOs have been pumped by large, bulky, expensive lasers; however the advancements in fiber laser technology and power has reduced the need for these large and expensive systems. Another method to generate light in the Mid-IR spectral region is to use optical fiber to generate supercontinuum.

Due the ability to engineer fibers both through micro-structuring the geometry and through material choices, fibers offer an attractive choice to producing broadband sources in the Mid-IR. Micro-structured optical fibers (MOF) offer the ability to fabricate parameters that are advantageous for broadband light generation, including increasing nonlinearities, controlling

light confinement, and tailoring the zero-dispersion wavelength (ZDW) for optimal broadband light generation [32–35]. Presently supercontinuum sources have been commercialized in the visible and near-IR wavelengths (400-2400 nm) for many applications particularly biological imaging, but these commercialized sources are limited to this wavelength range due to the use of silica based glasses [36].

While the mechanical properties of silica based glasses are advantageous for many applications the primary limitation for Mid-IR generation is the multiphonon absorption edge does not allow optical transparency > 4 μm and impurity losses due to OH impurities have a significant effect on the infrared transmission. Therefore, glasses with heavier atoms are need to shift the multiphonon absorption edge to longer wavelengths [37]. These glasses can fall into a few types including: heavy-metal-oxide, zirconium barium lanthanide sodium fluoride (ZBLAN), and chalcogenide based glasses. In this work we will discuss the use of tellurite ($TeO_2$), a heavy-metal-oxide glass, and chalcogenide glasses. These heavy-metal-oxide glasses and chalcogenide glasses have linear refractive indices greater than silica based glasses. Tellurite based glasses have refractive indices near 2 and $As_2S_3$ glasses near 2.44. In both these cases the material ZDW wavelength is shifted further into the Mid-IR. These values for the ZDW are 2.24 μm and 4.81 μm for tellurite and chalcogenide glasses, respectively. One final advantage of these non-silica compound glasses over that of silica is the intrinsic nonlinearities are 10 to 100 times greater. One measured value of tellurite has a nonlinear refractive index of $51\times10^{-20}$ $m^2/W$ and $As_2S_3$ based chalcogenide glasses have an order of magnitude great than that with $594\times10^{-20}$ $m^2/W$. In comparison Silica has a nonlinear refractive index of $2.7\times10^{-20}$ $m^2/W$.

Given the ability to create MOF with chalcogenide and tellurite glasses, both are interesting materials for generation of Mid-IR supercontinuum pumped by ultrashort pulse lasers at 2000 nm. As outlined above the intrinsic nonlinearities are relatively high and the zero dispersion of both these glasses is greater than 2 μm; therefore engineering of the fiber through tapering or MOF structures with extremely small core will provide for control of the ZDW and dispersion shape of the fiber for wavelengths from ~2 – 6 μm. Through these methods glasses with high optical transmission and high nonlinearities can be used to engineer extremely broadband light in the Mid-infrared.

*Table 1 Comparison of glass properties useful for Mid-IR light propagation*

| **Glass Type** | **Code** | **Main Components** | **$n_0$** | **$n_2 \times 10^{-20}$ $m^2/W$** | **ZDW** |
|---|---|---|---|---|---|
| **silica** | Si | $SiO_2$ | 1.45 | 2.7 [38] | 1.26 [39] |
| **Tellurite** | ZeTe | $ZnO\text{-}TeO_2$ | 2.03 | 51 [38] | 2.24 [39] |
| **Fluoride** | ZBLAN | $ZrF_4\text{-}BaF_2$ | 1.50 | 3.3 [38] | 1.62 [39] |
| **chalcogenide** | AsS | $As_2S_3$ | 2.44 | 594 [40] | 4.81 |
| | AsSe | $As_{40}Se_{60}$ | 2.83 [41] | 1100 [41] | 7.225 [42] |

## 1.4 Overview of Dissertation Contents

In the following chapters of this dissertation the discussion will build upon the basics mentioned in this chapter. In Chapter 2 the basics for high average power scaling in thulium doped fibers will be discussed. This includes an overview of work done to date developing kW

level systems using all-fiber geometries and a survey of methods for high power scaling once the limits of a single fiber aperture has been reached. Chapter 3 focuses on our results of developing integrated CW fiber systems for use in spectral beam combining. This chapter will describe work done using a relatively new meta-optic filter known as a guided-mode resonance filter to stabilize wavelengths. Chapter 4 will shift to a background for developing femtosecond systems and the methods and limitation of amplifications for these systems. Chapter 5 discusses the system design and construction for chirped pulse amplification in Tm fiber. Chapter 6 discusses the application of such ultrashort pulses for supercontinuum generation in the Mid-IR and the novel fibers used to generate these broadband spectra. Chapter 7 concludes the dissertations with an outlook to develop higher peak power systems using Tm fiber.

# CHAPTER 2: THEORETICAL DEVELOPMENT FOR HIGH AVERAGE POWER

## 2.1 High Power CW Fiber Lasers

The primary steps in producing high average power CW fiber laser systems have been the advent of DCF and advancements in high brightness semiconductor laser diodes. The primary growth in high average power systems has focused on fibers doped with Yb, due to its low quantum defect and readily available high power pump diodes. The power from single aperture Yb fiber lasers has grown exponentially and has recently achieved the 10 kW-level with single transverse mode quality [43]. While the growth in Yb systems is well documented and has shown great progress in producing high power quasi-single mode oscillators, Tm doped fibers are beginning to see a similar growth rate. Figure 9 shows the growth rate from watt level systems in 1997 to more recent results in Tm systems >1 kW [27]. The thermal stresses induced with 790 nm diodes and the performance of fiber components, such as TFB, ultimately limit the overall scalability of these systems. Two notable results in Tm:fiber are: one, the highest average power out of a single Tm fiber; and two, the highest power with a single-frequency output. The highest average power from a Tm:fiber laser to date was achieved in an all-fiber setup with two stages of amplification producing 1 kW average power [27]. However the more interesting result comes from a single-frequency where power reached 608 W without any deleterious nonlinear effects which described in Section 2.1.1.2.2 [44].

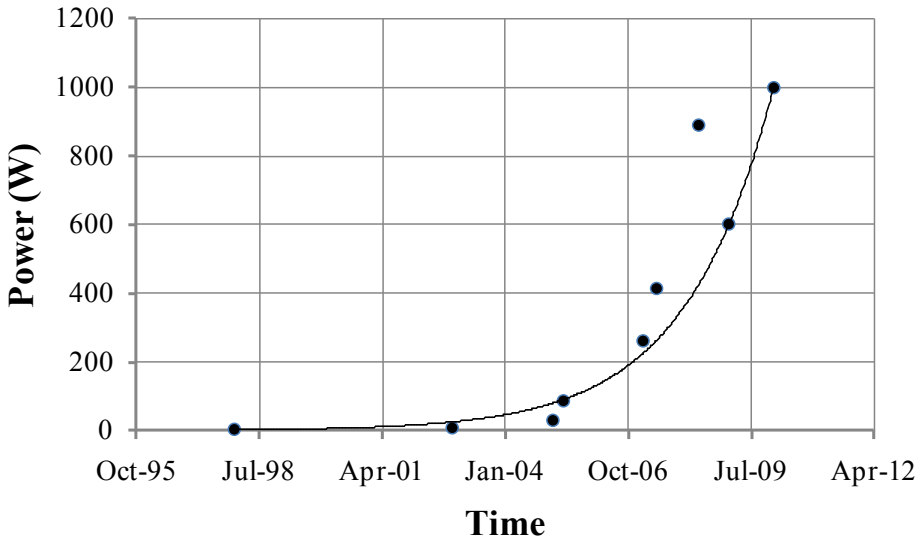


*Figure 9: Power milestones reached by Tm fiber lasers [27,44–50]*

### *2.1.1 Physical and Damage Limitations of Fiber Lasers*

2.1.1.1 Thermal and Damage

There are a number of physical limitations to increasing the output power from a single fiber aperture related to both thermal instabilities and damage of the fiber itself. Using equations and analysis from Brown and Hoffman [51] and Dawson *et al.*, [52] we can develop the physical limitations to high power CW lasers in general and for Tm fibers specifically. When dealing with the thermal limitations of fiber amplifiers Brown and Hoffmann, present three effects: rupture, core melting and thermal lensing. Using the optical-to-optical efficiency $\eta_{laser}$ and the fraction of absorbed pump power that is converted to heat $\eta_{heat}$ we can calculate the heat power deposited per unit length multiplied by a factor $(1-\eta_{heat})/\eta_{heat}$. For Tm fiber lasers we will assume some factors for both the optical-to-optical efficiency and the fraction of pump power converted to heat, typically this can be calculated using $\eta_{laser}+\eta_{heat}=1$, but with non-

radiative effects $\eta_{heat}$ may not equal the quantum defect. We will assume a 60% optical efficiency in a Tm fiber with 25/400 μm core/clad geometry and 30% heat deposition from absorbed pump power. All calculations will use realistic lengths for a fiber amplifier (5 m) and the core clad ratio already mentioned.

*2.1.1.1.1 Thermal Fracture*

Thermal Fracture is analogous to stress fracture in bulk solid state lasers. To calculate the power extractable before thermal fracture we use

$$P_{out}^{fracture} = \frac{\eta_{laser}}{\eta_{heat}} \frac{4\pi R_m}{1 - \frac{(r_{core})^2}{2(r_{clad})^2}} L \qquad (4)$$

where $R_m$ is the rupture modulus of the glass (2460 W/m) [53], $L$ is the length of fiber, $r_{core}$ and $r_{clad}$ are the radius of the core and clad, respectively. Using these values, the power before fracture of the optical fiber is > 300 kW.

*2.1.1.1.2 Core Melting Limits*

The following equation gives the heat power deposited per unit length that will lead to melting of the fiber core

$$P_{out}^{melting} = \frac{\eta_{laser}}{\eta_{heat}} \frac{4\pi k(T_m - T_c)}{1 + \frac{2k}{r_{clad} h} + 2ln(\frac{r_{clad}}{r_{core}})} L \qquad (5)$$

where $k$ is the thermal conductivity (1.38 W/m K) [54], $T_c$ is the coolant temperature, $T_m$ is the melting temperature of silica (1983 K) [54], and $h$ is a convective film coefficient that depends on the cooling mechanism. Values for $h$ can vary from 1000 ($W/m^2K$) for forced airflow and

with liquid flow cooling can increase to 10000 ($W/m^2K$) [55]. In our case with the fibers wrapped around a cooled mandrel we estimate a value of 5000($W/m^2K$). By inserting numbers into Equation (5) we expect core melting to occur at 31 kW.

However, Equation (5) does not take into account the heat flow out of the fiber accurately because fiber are typically coated with a fluoroacrylate coating for protection and not heat flow. In order to account for the coating in present systems Goodno et al., [56] have defined the thermal limits differently and accounted for the coatings of the fiber by setting the $T_m$ value to 105ºC. Goodno *et, al*., using a similar equation calculated a conservative maximum output power of 750 W from a 25/400 μm active fiber. Taking this into account with our slightly more efficient values for optical-to-optical and heat loss we expect a maximum power of 767 W.

Another method to model the temperature distribution in the fiber is to solve the steady-state heat equation for a cylindrically symmetric rod. This equation is as follows [57]

$$T(z,r) = T_0 + \frac{Q(z)}{4\pi}\begin{cases} -2\ln(\frac{r_{clad}}{r_{coat}}) \Big/ K_{coat} - -2\ln(\frac{r_{core}}{r_{clad}}) \Big/ K_g + + [1-(\frac{r}{rcore})^2] \Big/ K_g & r \le r_{core} \\ -2\ln(\frac{r_{clad}}{r_{coat}}) \Big/ K_{coat} - -2\ln(\frac{r}{r_{coat}}) \Big/ K_g & r_{core} < r \le r_{clad} \\ -2\ln(\frac{r}{r_{coat}}) \Big/ K_{coat} & r_{clad} < r \le r_{coat} \end{cases} \quad (6)$$

This equation includes the radii of the core (12.5 μm), clad (200 μm), and coating (275 μm) as well as terms for the thermal conductivities of the glass ($K_g$ = 0313 W/m-K) and coating ($K_{coat}$= 1.4 W/m-K). The value for $T_0$ is fixed at 14 ºC, the temperature that the outside jacket is cooled

to through conduction with a fiber mandrel. In this equation we set the maximum temperature to be the value at which the coating reaches its melting point. This value comes from the term *Q(z)*

$$Q(0) = 2\pi K_{coat} \frac{(T_{max} - T_0)}{\ln(\frac{r_{coat}}{r_{clad}})} \qquad (7)$$

Figure 10 shows the heat distribution for a fiber where the fluoracrylate coating reaches the melting temperature. The figure shows the temperature of the core and linking it with Equation (5) shows that at 760 W of output power the temperature of the Tm:fiber is ~ 200 ° C.

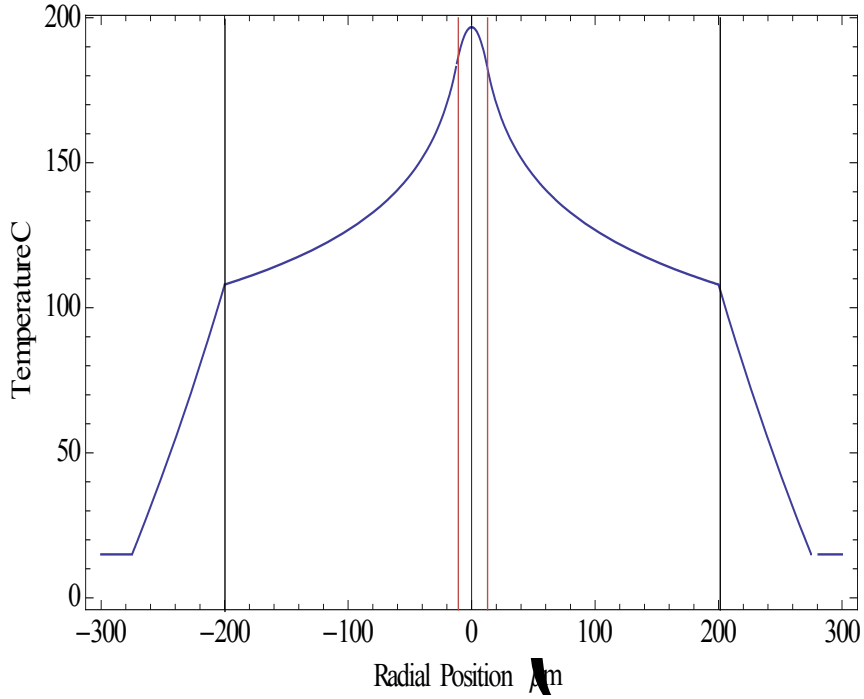


*Figure 10: Solution to the steady-state heat equation where the polymer coating will melt. The temperature of the core is approximately 200 C. Vertical red lines represent the core clad interface and black vertical lines indicate the glass cladding*

Another limitation that is not taken into account but should be mentioned is that if there is any scattering (from a splice) in a Tm system of the pump light into the cladding, the polymer layer strongly absorbs the 2 μm light reducing the power handling capability of the fiber laser.

*2.1.1.1.3 Thermal Lens*

Due to the $\frac{dn}{dT}$ of the silica glass high power can limit the extractable power by causing a refractive index gradient that leads to thermal lensing in the core. To calculate the power level we use this equation shown by Dawson et al. [52]

$$P_{out}^{lens} = \frac{\eta_{laser}}{\eta_{heat}} \frac{\pi k \lambda^2}{2 \frac{dn}{dT} r_{core}^2} L \qquad (8)$$

where $\frac{dn}{dT}$ of silica is 11.8 $\times 10^{-6}$ $K^{-1}$, $\lambda$ is the wavelength. We expect a thermal lens restriction to occur at ~ 47 kW at 2000 nm. Due to the quadratic relationship with the wavelength the thermal lens is expect to outperform a similar laser at 1 μm by a factor of 4.

2.1.1.2 Nonlinearities

CW fiber lasers have two primary nonlinear processes that limit the output power. The two nonlinearities are stimulated Raman scattering (SRS) and stimulated Brillouin scattering (SBS), and depend on the bandwidth of the laser itself. For broad bandwidth CW lasers the nonlinear limitation that is of greatest concern is stimulated Raman scattering, whereas for extremely narrow linewidth lasers the limitation is stimulated Brillouin scattering. One other nonlinear limitation to note is the self-focusing threshold; however, at a wavelength of 1 μm self-focusing occurs at ~ 4 MW of peak power so should not inhibit CW laser systems.

*2.1.1.2.1 Stimulated Raman Scattering*

Spontaneous Raman scattering is a process that occurs in a molecular medium where an photon interacts with a virtual state, and upon, relaxation populates a vibrational state causing a shift of energy to a vibrational state. Typically, the vibrational state that is excited has a lower frequency and the frequency shift is known as Stokes shift. An anti-Stokes process can also occur where a photon can take energy from an already excited molecular vibration shifting energy to a higher frequency. In the case of spontaneous emission, this is a very small energy transfer on the order of $10^{-6}$. In the case of intense pump fields SRS cause a significant increase in energy because the pump energy is transferred to the Stokes wave [58]. This nonlinear process becomes a limiting process in lasers because the laser signal is shifted into a Stokes wave as opposed to staying in the signal. This nonlinear process is a threshold based process and the threshold is governed by a set of coupled equation [58], but the threshold can be approximated using

$$P_{SRS} \approx \frac{16 A_{eff}}{g_R L_{eff}} \qquad (9)$$

where $g_R$ is the Raman gain coefficient ($1\times10^{-13}$ m/W at 1 μm), $A_{eff}$ is the area using the mode field diameter, and $L_{eff} = \frac{1}{g}(e^{gL} - 1)$ (g gain $m^{-1}$). A few approximations can be made for the $L_{eff}$ by writing $g = \frac{\ln(G)}{L}$ where G is an amplifier gain factor and for high gains we can approximate $e^{gL} - 1$ as $e^{gL}$ [52]

$$P_{SRS} \approx \frac{16\pi r_{MFD}^2}{g_R G \cdot L} ln(G) \qquad (10)$$

For the realistic values of the LMA fiber we can calculate the value of $P_{SRS}$ to be 1.35 kW without taking into account pump depletion.

*2.1.1.2.2 Stimulated Brillouin Scattering*

Another nonlinear process that affects the output power of fiber lasers is SBS. In this case, as the laser signal travels through the fiber, the laser signal field will generate an acoustic wave in the fiber through electrostriction. As the acoustic wave propagates, it creates a refractive index modulation in the fiber and scatters light at a downshifted frequency through Bragg diffraction. Light is down shifted because the refractive index modulation traveling in the fiber causes a Doppler shift [58]. The downshift is relatively small compared to SRS and is typically in the 10's GHz; for Tm lasers this value is closer to 8.3 GHz. The Bragg diffraction reflects light in the backward propagating direction. SBS also has a threshold similar to SRS and can be approximated using,

$$P_{SBS} \approx \frac{17\ \mathrm{A}_{eff}}{g_B(\Delta\nu)L_{eff}} \qquad (11)$$

where $A_{eff}$ and $L_{eff}$ are the same as the SRS, but $g_B$ is the Brillouin gain coefficient. The Brillouin gain coefficient $g_B$ is defined as

$$g_B(\nu_B) = \frac{8\pi^2\gamma_e^2}{n_p\lambda_p^2\rho_0 c\nu_A\Gamma_B} \qquad (12)$$

Where $\gamma_e \approx .902$ (electrostrictive constant of silica) and the density $\rho_0 \approx 2210$ kg/m$^3$, $n_p$ and $\lambda_p$ are the refractive index and laser wavelength, respectively, and $\nu_A$ is the Brillouin shift. The linewidth of the Lorentzian spectrum of the Brillouin gain is given by $\Gamma_B$. Using similar approximations as were made for the SRS case we can simplify the threshold equation for SBS as follows

$$P_{SBS} \approx \frac{17\pi r_{core}^2}{g_B(\Delta\nu)L}\Gamma^2 \frac{\ln(G)}{G} \qquad (13)$$

Before determining the thresholds for light at 2 μm a few other considerations need to be mentioned. The Stokes shift is inversely proportional to wavelength, the Brillouin linewidth narrows at longer wavelengths due to a $\frac{1}{\lambda^2}$ relationship, and the peak gain is not affected by wavelength [58]. Due to wavelength scaling we can expect that SBS suppression via inhomogeneous broadening at 2 μm will be two times that of a system operating at 1 μm and four times that due to linewidth broadening.

Due to the heating in the core of Tm:fiber there are additional considerations to take into account such as thermal broadened SBS. Goodno et al., presented a prediction that incorporates the SBS and thermal model. With the 25/400 μm, passive fiber they show in passive fiber that the power limit for a single frequency 2 μm laser is $P_{SBS}L$ = 425 W-m, and with a 1.7 m fiber the power before SBS was 250 W. In the case of the Tm:fiber the value is larger with an SBS gain linewidth of 13 MHz because the thermal properties of the gain fiber broaden the SBS linewidth. Doping the active fiber with 10 wt % Al to reduce clustering of Tm ions leads to an increased

acoustic velocity; thus increases the SBS gain peak by a few hundred MHz. This increase causes a different gain peak from the passive fiber and it is expected that the doped fiber can handle more output power before SBS is a limitation; however, the undoped fiber limits the system [56].

2.1.1.3 Damage Limitations

There are a number of optical damage effects that can occur in the fiber, both fiber fuses and optical end-face damage that can limit the laser power. End face damage can be reduced by using glass end-caps on the fiber to expand the mode-field diameter before reaching the glass air interface. To quantify the power level at which damage occurs with a fundamental Gaussian mode we use

$$P_{out}^{\ damage} = I_{damage}\pi r_{MFD}^2$$

where $I_{damage}$ is the surface damage limit of silica (~10W/μm$^2$). Using this equation we expect the surface damage threshold of a CW fiber laser with 25/400 μm core/clad ratio to be ~ 4.5 kW.

### *2.1.2 Methods of Power Scaling*

As discussed in the section 2.1.1, there is a point where the maximum achievable average power from a single fiber aperture will be reached. In the case of a realistic Tm fiber amplifier, values were calculated for thermal restraints and nonlinear restraints. From calculations in Section 2.1.1.1.2, the biggest limitation to using commercially available Tm fiber is the thermal limitation where the coating temperature increases beyond its melting point. According to

conservative calculations this was ~760 W and for a system to be used for an extended period of time this heat generation will limit the output power.

In order to overcome the limits for single aperture output, it is possible to combine multiple beams into a single diffraction-limited beam. Through this method the output power can be scaled with the number of lasers present. The two primary methods for beam combining are coherent beam combining (CBC) and spectral beam combining (SBC).

#### 2.1.2.1 Coherent Beam Combining

CBC offers a possibility to scale output power of single fiber apertures by using multiple gain elements. Rather than sacrificing spectral brightness, as is the case for SBC, CBC requires multiple laser systems to be phase locked with each other. In order to ensure the phases of the individual channels are locked, several methods have been developed, using a common oscillator, evanescent-wave or leaky-mode coupling, self-organizing, active feedback, and nonlinear optical (phase conjugation) [59]. To date, CBC has produced 100 kW combined power using multiple with Nd:YAG slab amplifiers with a beam quality 2.9 times the diffraction limit [60].

#### 2.1.2.2 Spectral Beam Combining

Spectral beam combining (SBC) is a power scaling method where spectral brightness is traded for spatial brightness by combining multiple beams at slightly different wavelengths into a single diffraction-limited beam. Generally a SBC system contains multiple wavelength-stabilized lasers which are incident on either one or more diffractive or wavelength selective elements that combine the separate beams into a single beam. Figure 11 shows a schematic of a

SBC system with multiple laser channels incident at different angles and combined in a single beam. While the concept and techniques of SBC were introduced in the telecommunications field with WDM semiconductor laser transmitters, the first high power proof of concept idea was presented in 1999 where two fibers were placed in a linear array and focused through a transform lens onto a diffraction grating [61]. After the grating, the different wavelength beams from the two fiber facets were overlapped and reflected back into the cavity using an output coupler [62].

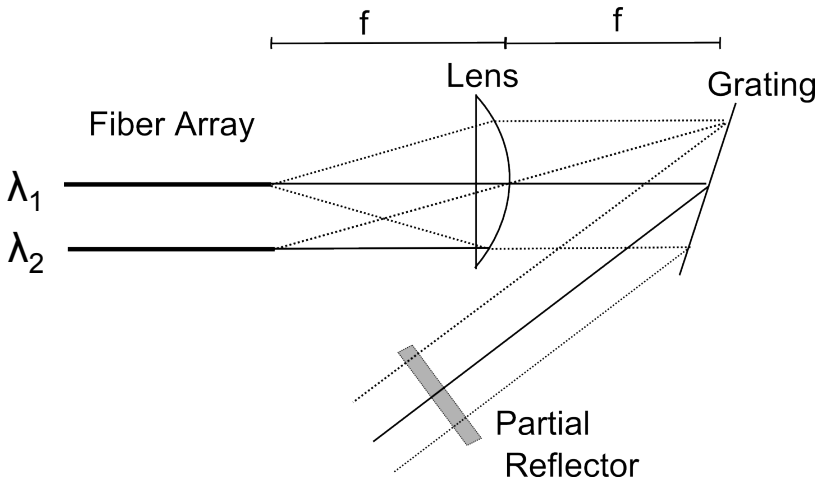


*Figure 11: Experimental setup of transform lens SBC.*

Since this initial experiment with fiber lasers numerous advancements in combining elements have occurred, facilitating average powers up to 8.2 kW in Yb fiber lasers [63]. The transform lens design in Figure 11 has been used in the Yb system as described as well as with Tm fiber lasers systems [64]. Aside from this transform lens technique, diffraction gratings can be used to combine multiple narrow linewidth collimated beams incident on the grating from different incident angles to produce a nearly diffraction-limited beam. This method requires high quality diffraction gratings for high power scaling, and is limited by thermal or damage effects. A high quality dielectric diffraction grating was fabricated for the 2 kW test with near

polarization independence, allowing for non-PM fiber sources [64]. Using this technique Wirth et al. was able to achieve 61% efficiency with respect to total launched pump power with $M_x^2$= 2.0 and $M_y^2$ = 1.8 [64].

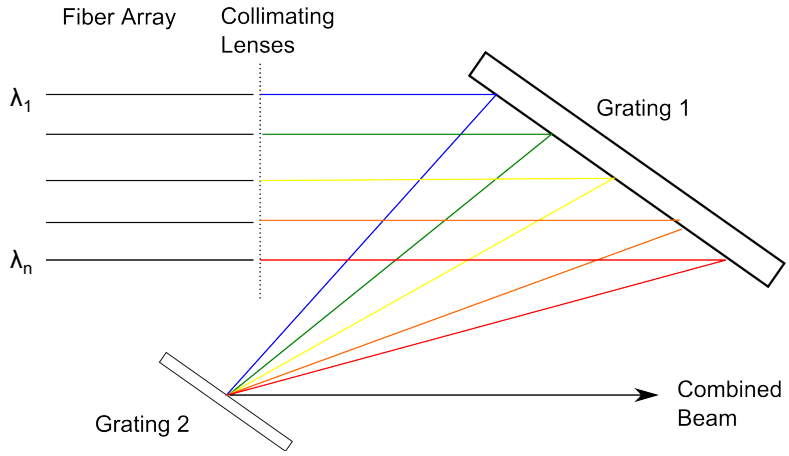


*Figure 12: Schematic of the dual-grating setup*

Improved performance is offered by a dual-grating combination system has been proposed and is shown in Figure 12 [65]. The dual-grating system offers advantages over the single grating system because it relaxes the condition of the narrow linewidth $\Delta\lambda$. In the single grating system, linewidths must remain narrow due to spatial dispersion caused by the grating. This in turn, places severe constraints on the sources for the individual wavelength channels associated with SBS. In the two-grating system, light is collimated from the fiber aperture and propagates parallel to the other fiber channels before reaching the first grating. The individual channels are diffracted such that they combine at the same spot on the second grating, which compensates for the spatial dispersion added at the first grating and outputs a single diffraction-limited beam [65].

Using this dual-grating setup two fiber lasers capable of producing 115 W with linewidths of ~0.15 nm were combined to an output power of 190 W with an $M^2$=1.18. With the same technique lower power systems were compared to show how the beam quality is affected by a single grating setup vs. a double grating setup. At 10.9 W combined power, the $M^2$ in the dispersed axis after a single grating was 1.96 and after the second grating was reduced to 1.2 [65].

One more recent and promising method for SBC uses VBGs to combine multiple wavelengths by reflecting a desired wavelength and passing it through a minimum of the reflection spectrum of another VBG. Using this method a total of 5 independent lasers spaced 0.5 nm apart have been combined to produce 770 W of output power with an $M^2$=1.16. This system had an absolute combining efficiency of 91.7% [66]. VBGs also offer a number of different monolithic configurations that can be used to combine multiple beams in a single element and Andrusyak et al. have combined four beams in a single VBG with a wavelength spacing of 0.7 nm.

Another techniques was demonstrated in 2008 using inexpensive long pass interference filters designed with a sharp wavelength transition from reflecting to transmitting. Regelskis et al. used long wavelength pass filters with 1 nm wide reflective-to-transmission edges to combine laser channels separated by about 2 nm. In this demonstration, the output from a single pulsed nanosecond oscillator was split by the interference filters and the independent channels were amplified in separate amplifiers and recombined with similar filters. The setup is show in Figure 13. This experiment achieved total combined average powers of 52 W at 100 kHz repetition rate,

amounting to >90% combining efficiency. Using lower repetition rates and longer pulse duration a combined pulse energy of ~1.9 mJ was achieved, yet $M^2$ was not reported [67].

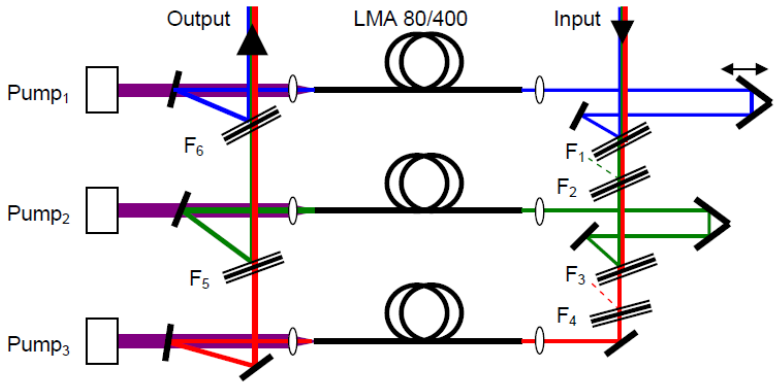


*Figure 13: Experimental setup for interference filter based SBC. [67]*

More recently, a similar experiment was completed with low cost interference filter that were designed as band pass filters as opposed to long pass filters. Four separate laser oscillators producing 25 ns q-switched pulses were electronically synchronized and amplified in separate rod type PCFs. Using the design for combination shown in

Figure 14, four lasers operating at 50 kHz were combined to 208 W average power and 4.2 mJ pulse energy. By reducing the repetition rate, the combined pulse energy could be increased to 6.3 mJ. The limiting factor in this experiment was the low cost interference filters and that caused thermal lens induced wavefront distortions. $M^2$ was 2.3 for the 208 W maximum average power [68].

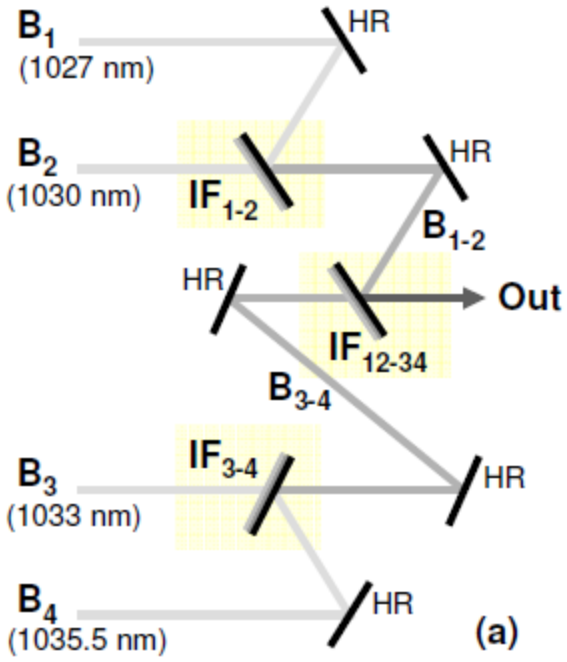


*Figure 14: Setup for SBC using low cost bandpass filters. [68]*

SBC at 2 μm is immature compared to 1 μm, primarily due to the lack of components that can provide high combining efficiency. SBC using Tm fibers was first shown in 2001 using the transform lens method with four fiber apertures [69]. Four cladding pumped fiber lasers were transmitted through a transform lens onto a diffraction grating (600 ln/mm), which combined the beams onto the output coupler. These experiments produced a combined beam with 23.6 W for a total launched power of 85 W with wavelength separations >20 nm.

# CHAPTER 3: SPECTRALLY STABLE HIGH POWER CW

## 3.1 Spectrally Stable CW Fiber Lasers

In this work we will show that spectrally stable lasers are an integral component to the scaling of laser powers by SBC. Fiber Bragg gratings and volume Bragg gratings will be introduced as elements that can achieve spectral stabilization. A new meta-optic element will be introduced in section 3.2, known as a guided mode resonance filter (GMRF), that also provides spectral stabilization and can be fabricated in large quantities.

### *3.1.1 Fiber Bragg Gratings*

Fiber Bragg gratings (FBG) provide spectrally selective feedback that can be used in an all fiber configuration for high powers. Aside from providing a method for all-fiber spectral selection, FBGs have other beneficial properties including low insertion loss, high return loss or extinction, wavelength tunable, and low costs, depending on the fabrication method. Highly reflective FBGs are made with a periodic modulation of the refractive index forming a Bragg stack. In the simplest case, light matching the Bragg condition is reflected back without otherwise disturbing propagation in the fiber. Aside from the reflective FBG, multiple additional designs are possible including long period gratings for transmission [70], chirped refractive index structures for dispersion compensation in ultrashort laser cavities, and Gaussian-apodized [71].

Multiple techniques are used to produce FBGs including using phase masks to expose a photosensitive fiber to UV light, point-by-point exposure with UV light, and femtosecond laser writing [72,73]. FBGs are a primary choice for all single mode fiber systems but can be difficult to implement in LMA fibers. As the core size increases higher order modes are present in the

fiber and have different effective indices within the FBG, which excites the higher order modes and broadens the spectral linewidth [74]. Aside from difficulties with different effective indices between modes, it is difficult to uniformly modify the refractive index of LMA fiber across the core because of its large diameter [75].

Tm:fiber works well with FBGs and the pairing has been shown to work well in many publications [76–79]. Tang et, al., showed an all-fiber Tm system capable of 137 W with an optical-to-optical- efficiency of 62% with 3 nm bandwidth. In the works presented in Section 3.2-3.4 FBGs are a viable solution to the fabrication of single-mode oscillators that have spectrally stable narrow-linewidth outputs. Including inline polarizers into a system with the FBGs will provide all-fiber polarized systems for the generation of laser light spaced a few nm apart. While FBGs can be tunable by modifying temperature of the fiber or physically manipulating the fiber in order to work with different wavelength new phase masks need to be fabricated, for traditional FBG fabrication techniques. The development of new phase masks can be expensive and many may be need to span many wavelengths. However, we will introduce and use GMRFs because of the ability to cheaply develop many narrow-linewidth systems.

### *3.1.2 Volume Bragg Gratings*

Volume Bragg gratings (VBG) are Bragg gratings formed in bulk photothermorefractive (PTR) glass by exposing the glass with UV light and thermally developing the structure to produce index modulation [80]. As in FBGs, the index modulation in this volume creates a grating and when the Bragg condition is satisfied light can be reflected or transmitted with high efficiency with narrow bandwidths. Angle tuning of the spectral feedback from a VBG is also

possible in the correct cavity configuration. Due to the relatively large aperture of VBGs, high power wavelength stabilized systems have been shown in Er:Yb, Yb, and Tm fiber laser systems [81–83].

## 3.2 Theoretical and Experimental discussion of GMRFs

### *3.2.1 GMRF Theory*

Guided Mode Resonance Filters (GMRF) offer another free space spectrally selective element compatible with LMA fibers. GMRF technology is derived from one of Wood's anomalies, was described by Hessel in 1965, and implemented by Magnusson in 1992 [84,85]. Practically GMRFs contain two thin film layers deposited on a substrate. The top layer deposited is etched to form a sub-wavelength diffraction grating. The second layer acts as a waveguide (confinement) layer for the light. Physically, light incident the grating structure is diffracted into evanescent orders, which are coupled into the waveguide layer. These evanescent modes are often leaky and couple back out of the device. This leakage can be engineered to provide specific spectrally-selective feedback to the light source. Figure 15 shows a drawing of the physical layout and process of a GMRF

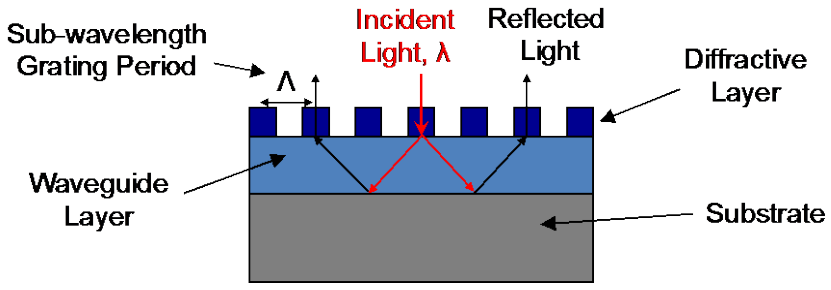


*Figure 15: Profile view of a GMRF highlighting the physical processes associated with the filter.*

The performance of these components depends on several structural parameters: the grating period and duty cycle; the grating layer thickness and material index; the waveguide layer thickness and material index; and the substrate material index. By modifying these values GMRFs can be fabricated to have specific peak reflection, resonances, and linewidths in reflection or transmission. GMRFs can also be designed to operate in polarization sensitive or insensitive modalities.

Recent examples of GMRF stabilized lasers have been demonstrated in Er:Yb and Tm fiber laser systems by Prof. Eric Johnson's group at Clemson University. The first demonstration occurred in an Er:Yb system with output powers up to 1 W and peak reflectivity > 90% and linewidth of 0.18 nm [86].

### *3.2.2 Broadband Characterization of GMRF*

3.2.2.1 Polarization Insensitive Passive Characterization

The first demonstration of GMRF technology at 2 μm wavelengths utilized a polarization insensitive design. Multiple wafers were fabricated with >64 GMRFs per wafer, also known as die. The large number of die being produced allowed for the varying of several fabrication parameters on a single wafer to facilitate optimization of the filter design/fabrication parameters. In the case for these hexagonally structured elements, the duty cycle of the etched grating was varied.

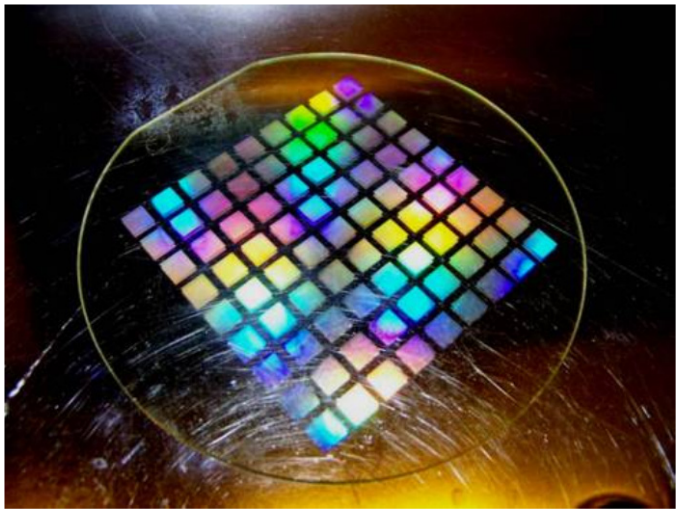

*Figure 16: Wafer with 81 GMRF filters that were designed to operate at different wavelengths. This wafer highlights the quantity of GMRF that can be fabricated with different parameters [87].*

GMRFs were fabricated using Plasma Enhanced Chemical Vapor Deposition (PECVD), with the fused silica substrates coated with 395 nm thick silicon nitride ($Si_xN_y$) and 380 nm thick silicon oxide ($SiO_x$). The layer of $Si_xN_y$ was deposited directly onto the fused silica wafer and acted as the confinement layer; whereas, the $SiO_x$ layer became the grating layer. The sub-wavelength grating was etched into the topmost layer (~ 130 nm) using standard microlithography. A hexagonal sub-wavelength grating structure was used because it provides for a polarization insensitive device. In the process of fabrication, errors due to process control and deviation caused resonance wavelengths to shift to shorter wavelengths than computational models predicted; however, this did not affect the resonance linewidth.

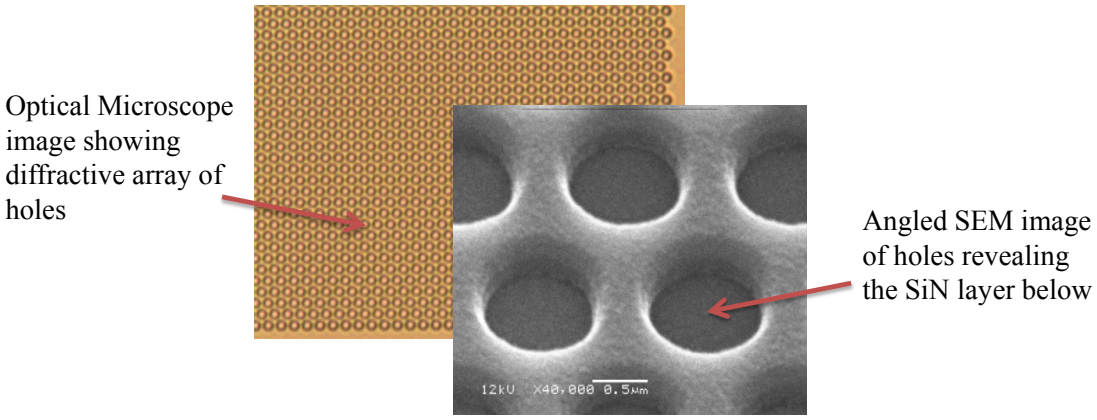


*Figure 17: Optical microscope and scanning electron microscope image of a hexagonal GMRF structure [88].*

In order to characterize the performance of the fabricated GMRF, a broadband ASE source was built to passively measure the resonance wavelength, peak reflectivity, and linewidth of the filter by measuring the broadband source transmission through the filter. The ASE source contained a 4 m long section of non-PM 25/400 LMA fiber, with a core NA of 0.09. The active fiber was wrapped around an 11 cm diameter mandrel with a V-groove cut into the side. This fiber was water cooled to ~ 14° C in order maintain high efficiency. Both ends of the active fiber were spliced to sections of matching undoped fiber and each was kept in an aluminum V-groove holder with silicone thermal paste to mitigate thermal stress during optical pumping. Both free ends of the undoped fiber were held in water-cooled cooper V-grooves.

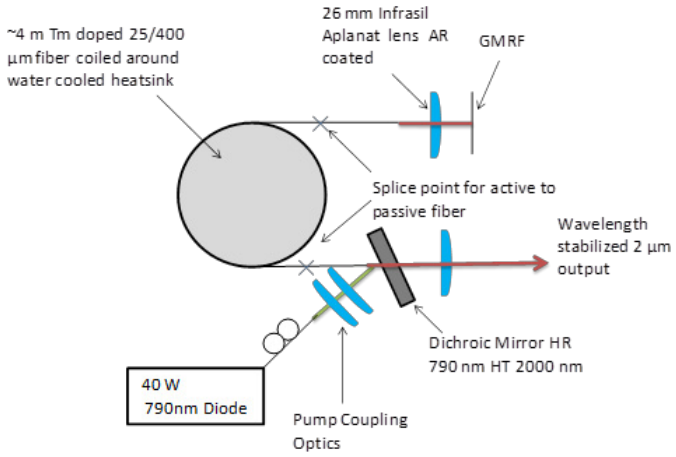


*Figure 18: Schematic for testing passive and active properties of GMRFs. In the case of passive testing the laser power was reduced below threshold so ASE propagates through the GMRF [89].*

The Tm ASE source was pumped using a 400 µm 0.22 NA multimode 790 nm pump diode. The output from the pump delivery fiber was coupled through a pair of 50 mm focal length achromatic lenses and reflected from an angled dichroic mirror, which provided high reflection at 800 nm and high transmission at 2000 nm. The pump light entered a flat cleaved fiber facet of the undoped fiber. The flat cleaved provided 4% feedback from Fresnel reflections, so this section of fiber will act as a fiber oscillator in later tests. The opposite section of undoped fiber was angle cleaved to ~ 8° in order to suppress any parasitic lasing. This end of the fiber was collimated using a 26 mm AR coated Infrasil aplanatic triplet, and aligned to the reflective GMRF.

In order to operate as a broadband ASE source the pump power was set where the output of the Tm:fiber laser was below laser threshold allowing broadband light to propagate out of the angle cleaved facet. Using an optical spectrum analyzer (OSA) this spectrum was recorded prior to inserting the GMRF into the beam path. The pump power was increased such that the

feedback from the GMRF would cause lasing at the maximum laser efficiency and spectral stability to optimize the orientation of the GMRF, then pump power was reduced to allow the ASE to transmit through the GMRF. Using this method, notches in the broadband ASE appear because the GMRF causes reflection of these specific wavelengths.

When the GMRF was optimized as a feedback element in the laser cavity, the orthogonal polarizations propagating out of the fiber experienced two different wavelength resonances. In this case, Figure 19, the resonance is centered at 2013.12 nm and has a spectral width of 1.89 nm; however, the maximum reflection of the two peaks is ~2.25 dB or ~40% assuming all loss is due to the reflective mechanism of the filter. While using the ASE in transmission through the GMRF, the filter orientation was optimized to collapse the two peaks into a single peak with a linewidth of ~ 500 pm (FWHM). The notch in the ASE transmission also increased to ~7.3 dB from the baseline corresponding to a reflectivity of ~81 %, Figure 20. In this configuration, as will be discussed in the section describing laser oscillations, this alignment does not allow for feedback into the laser. The double peak corresponds to polarization splitting. Polarization splitting was seen because incident light was at non-normal incidence or is nonplanar causing asymmetric coupling of the mode into the confinement layer. The orthogonal polarization states were coupled differently, thus splitting the resonances.

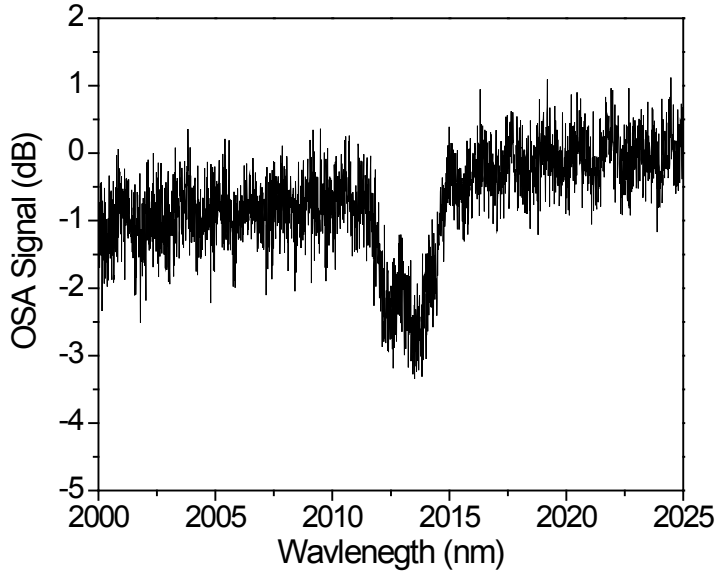


*Figure 19: Passive characterization of a polarization insensitive GMRF. In this figure the GMRF was aligned for lasing but appears misaligned due to the generation of a broad transmission band and two peaks representing orthogonal polarizations [89].*

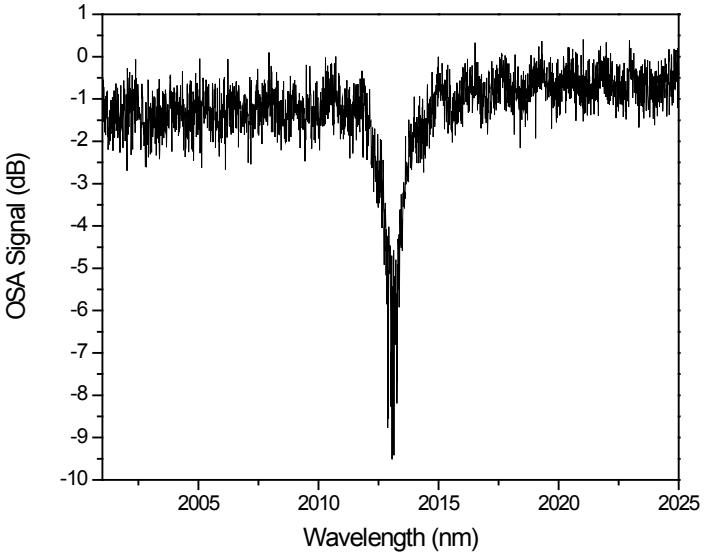


*Figure 20: Passive characterization of a polarization insensitive GMRF. In this case the GMRF position was manipulated by adjusting the tip/tilt of an optical mount to allow the peaks to converge and create a higher reflective device [89].*

3.2.2.2 Polarization Sensitive Passive Characterization

In the polarization sensitive GMRF design, the sub-wavelength grating structure of the GMRF was designed as a one-dimensional grating, shown in Figure 21. Fabrication techniques and layer materials were similar to the polarization insensitive case. The $Si_xN_y$ layer was deposited onto the fused silica substrate and a layer of $SiO_x$ was deposited on top of the $Si_xN_y$ layer. As opposed to the hexagonal array of holes producing the sub-wavelength grating, this polarization sensitive design required a linear grating etched 180 nm into the $SiO_x$.

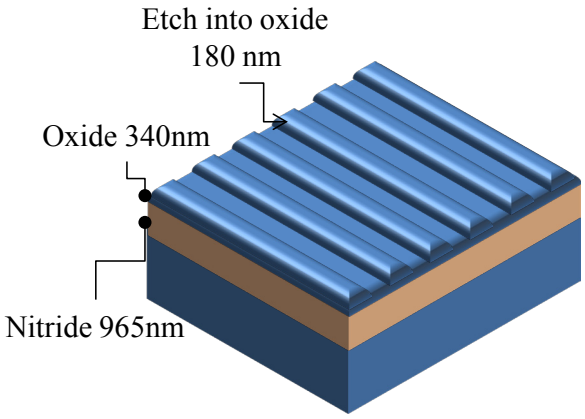


*Figure 21: Polarization sensitive GMRF design with a linear grating etched into the surface.*

The polarization sensitive GMRF was designed specifically for stabilizing wavelengths and polarization in a spectral band between 2030 and 2050 nm. This design places one polarization in this wavelength band and the orthogonal near 2015 nm. In order to characterize this GMRF a similar setup as already described above was used, but the output was passed through a Glan laser polarizer to probe the individual polarizations. Using this method, for one die we measured a ~14 dB decrease in transmission at 2046 nm with a linewidth of 100 pm, Figure 22.

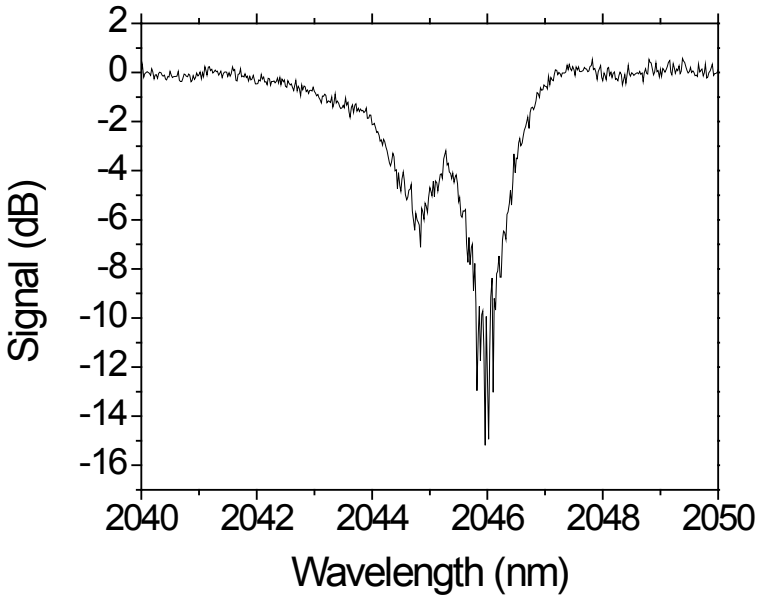


*Figure 22: Passive characterization of the polarization sensitive GMRF*

### *3.2.3 Laser Operation with GMRF*

3.2.3.1 Polarization Insensitive Laser Results

The GMRF provided feedback for a LMA fiber oscillator and provided wavelength stabilization and spectral narrowing for output powers up to 10 W. The same fiber setup described in Section 3.2.2.1 and Figure 18 was used for laser experiments with the polarization sensitive GMRF as described. Above output powers of 10 W parasitic lasing appeared at wavelengths outside of the spectral envelope imposed by the GMRF. Feedback from the relatively low reflectivity GMRF produced a laser with ~ 34% slope efficiency with respect to launched pump power out of a single fiber output, shown in Figure 23. Taking into account power from both ends of the fiber (flat cleave and transmission through the GMRF) the slope efficiency of the system increased to ~40%

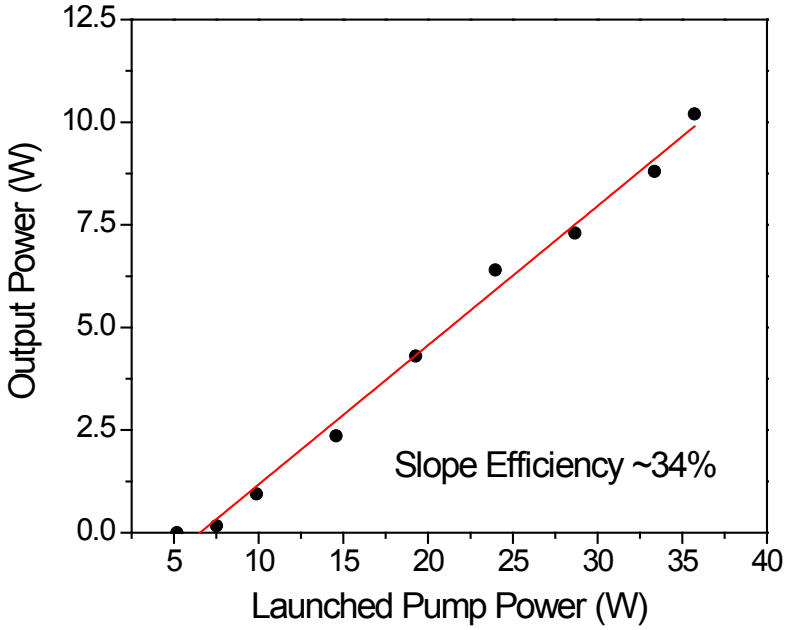


*Figure 23: Slope efficiency of the polarization insensitive GMRF shows 34% efficiency [89].*

The spectral output of this system was measured using an OSA and was dependent on the output power of the laser and is displayed in Figure 24. Just above laser threshold, the wavelength was centered at 2013.70 nm with a FWHM of 0.18 nm. As the laser power increased the wavelength shifted to longer wavelengths with a center wavelength of 2014.02 nm with a FWHM of 0.40 nm at 6 W output. At 10 W output power, two laser peaks were observed with a net linewidth of 0.70 nm due to the presence of the polarization splitting in the GMRF at non-normal incidence. This wavelength shift and spectral broadening is due to the inhomogenously broadened nature of Tm and gain competition within the spectral reflection. If parasitic lasing were better suppressed by higher reflectivies, we expect that the spectrum would continue broadening with increasing power until the reflective envelope is filled.

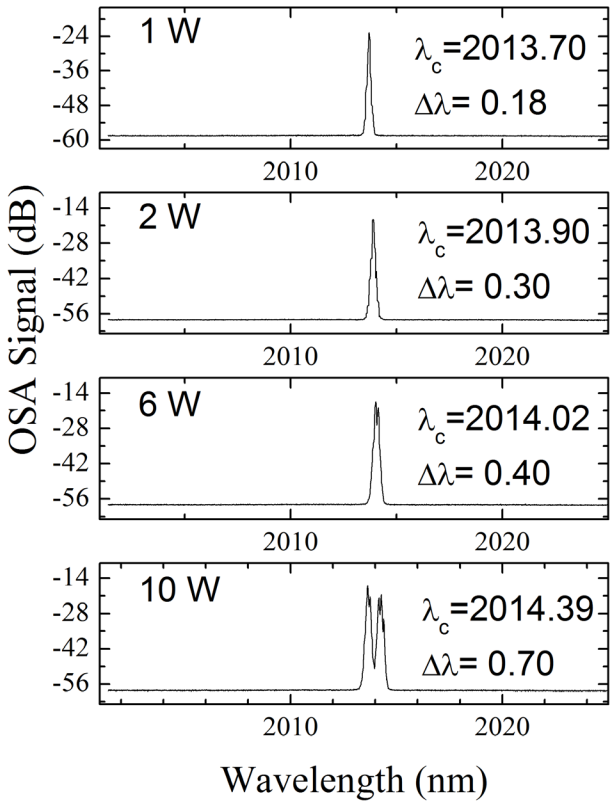


*Figure 24: Spectral evolution of laser signal stabilized by the GMRF [89].*

3.2.3.2 Polarization Sensitive Laser Results

The polarization sensitive GMRFs were designed to be used as wavelength stabilization elements for multiple single-mode oscillators. These oscillators were used as the master oscillator for multiple quasi all-fiber MOPA systems for spectral beam combining, these results will be described in section 3.4.1. Due to the requirements of this project, the laser oscillator utilized a different architecture than the one described in previous section.

The oscillator consisted of a 4.5 m long PM doped fiber single-mode fiber with a 10/130 core clad geometry and core NA of 0.15. Pump light from a DILAS Diodenlaser GmbH diode providing 35 W at 793 nm was delivered to the active fiber using a 2+1 x 1 TFB. The TFB (ITF

labs) contained two 105/125 multi-mode pump arms, where only one was used, and an undoped single-mode signal pass-through fiber matching the active PM 10/130 fiber. The fiber facet directed towards the GMRF was angle cleaved to reduce parasitic oscillations from Fresnel reflections, and the fiber was coupled to the GMRF using an 11 mm aspheric lens to collimate the light. A HWP was placed in the path between the GMRF and fiber facet in order to optimize the polarization from the reflection from the GMRF relative to the stress rods of the fiber. The opposite end of the active fiber was spliced to a chirped fiber Bragg grating (CFBG) from TeraXion written into a passive section of PM 10/130 fiber, which provided 20% reflectivity from 2030 – 2050 nm.

We chose to use a CFBG to facilitate greater wavelength flexibility, as this architecture allows us to produce an output within a 2030 – 2050 nm window simply by changing the GMRF in the cavity. As a representative, the linewidth of one of the oscillators was 390 pm at 10 dB below the spectral peak with a center wavelength of 2033.5 nm. The output power is 3.2 W for 12 W of launched pump, and the PER is 18 dB [90].

## 3.3 Applications of GMRFs for Spectral Beam Combining

### *3.3.1 Diffraction Grating Based SBC*

#### 3.3.1.1 System Design

Three MOPA systems were built where two channels were stabilized by GMRFs and the third was stabilized using a gold-coated copper substrate diffraction grating. The diffraction grating was used for simplicity because the laser was designed as a tunable MOPA for atmospheric propagation testing [91] although a GMRF could have been used as a substitute for

the diffraction grating. In the systems using GMRFs, both the oscillator and amplifier consisted of the same LMA fiber, a Tm doped (4 wt%) 25/400 μm with 0.09 core NA fiber. Both oscillator cavities were built using different wavelength GMRFs as the highly reflective element and the 4% Fresnel reflection from a flat cleaved fiber as the output coupler. Fiber facets directed toward the GMRF were angle cleaved (8°) to mitigate parasitic lasing. These two oscillators had wavelength of 1984.8 and 2012.8 nm and the third laser was tuned to 2008.8 nm. Each had a linewidth of 100-200 pm [92].

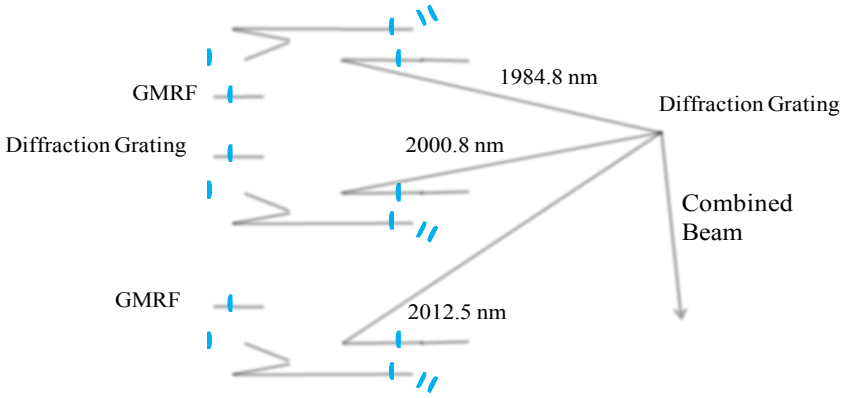


*Figure 25: Schematic of SBC with a reflective diffraction grating [92].*

Each oscillator seeded a power amplifier with ~1.5 W. Each Power amplifier was pumped by a 300 W, 790 nm laser diode (LIMO). The $M^2$ and slope efficiencies for each amplifier were measured. $M^2$s were consistently ~1.2 and slope efficiencies of the power amplifiers were between 50-60%. Individually each power amplifier was capable of producing powers between 40 and 120 W, and in each case an intra-stage isolator was needed to amplify beyond 50 W; however, only one isolator was available at the time of these experiments.

Amplifier outputs were collimated using uncoated fused-silica plano-convex lenses with 100 mm focal length; thus each interface produced a 4% loss due to Fresnel reflections.

Each beam path was match in length before combining on the grating in order to maintain similar divergences to and from the diffraction grating. In order to match the beam propagation path, the longest path was used as the reference and the others were extended to a value of 6m. The beam combiner was a water-cooled (14° C) plane-ruled gold-coated copper reflection grating with 600 lines/mm blazed for 1850 nm in the Littrow condition. Due to the unpolarized incident light this grating had an efficiency of ~ 70%.

3.3.1.2 SBC Results

The beam was characterized at ~2, ~5, and ~8 m from the combining element using a Spiricon Pyrocam III in order to insure that the three individual beams were spatially overlapped, Figure 26. The combined beam was measured at 20 W using an OSA to ensure that only the combined wavelengths were present and is shown in Figure 27. The three wavelengths (1984.8 nm, 2000.8 nm, and 2012.5 nm) from the individual lasers are clearly visible more than 30 dB above the noise floor, Figure 27. The maximum combined power was 49 W, with a total power of 73 W incident on the grating with ~25 W from each channel. The combining efficiency at 2 μm was 67% with respect to the incident light, and 32% with respect to the diode power pumping the amplifiers.

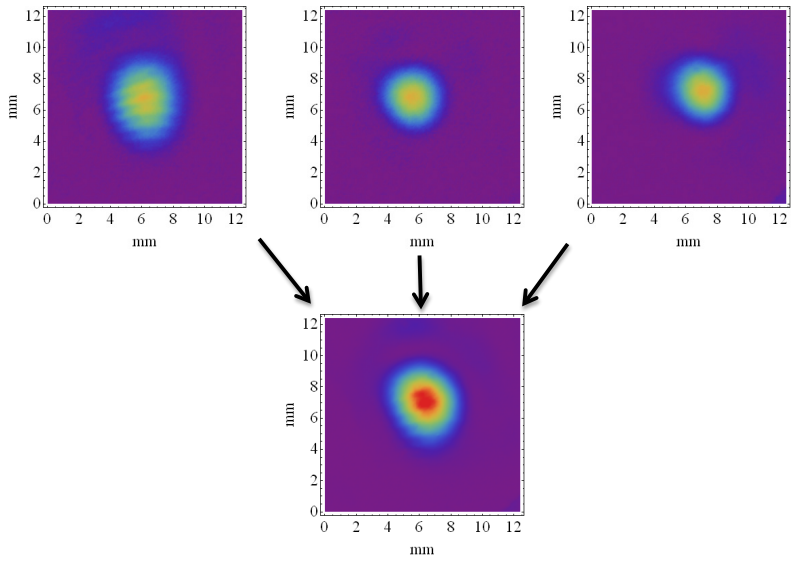


*Figure 26: Individual images of three separate beams for SBC. A combination of all three beams is shown as a mathematical addition of the three individual beams [92].*

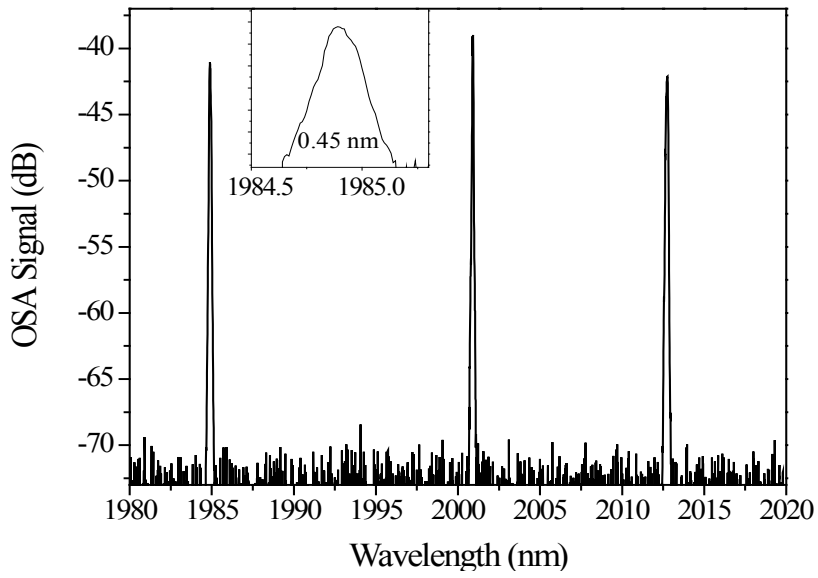


*Figure 27: OSA trace of all three combined beams. This verifies the wavelengths of 1985, 2001, and 2012 nm. The inset shows the linewidth of the beam centered near 1985 nm [92].*

The beam quality of the combined beam was characterized ~5 m from the combining grating. The beam quality of each of the individual beams was measured with 20 W incident on the grating and the combined beam quality was measured at a power level of 35 W. Individual

channels exhibited $M^2$ values of ~1.6 in the plane orthogonal to the grating plane and between 1.5-1.7 in the parallel plane. Increases in the $M^2$ from the individual channel measurements were expected in the plane orthogonal to the grating plane, the vertical plane, due to spatial dispersion. It is expected that the parallel plane increased due to wavefront distortion added from the sub-optimal uncoated plano-convex lenses and the multiple elements that the beam passed through. At the combined power of 35 W, thermal distortions from the combining grating and subsequent beam guiding components resulted in $M^2$ values of ~1.9 and ~2.6 in the planes orthogonal and parallel to the diffractive plane, respectively. This axial shift arises from astigmatism introduced by thermal lensing. It is expected that the $M^2$ degradation at the 35 W combined level would be present if a single channel were operating at similar levels due to the absorption and subsequent heating of the gold-coated diffraction grating causing thermal degradation.

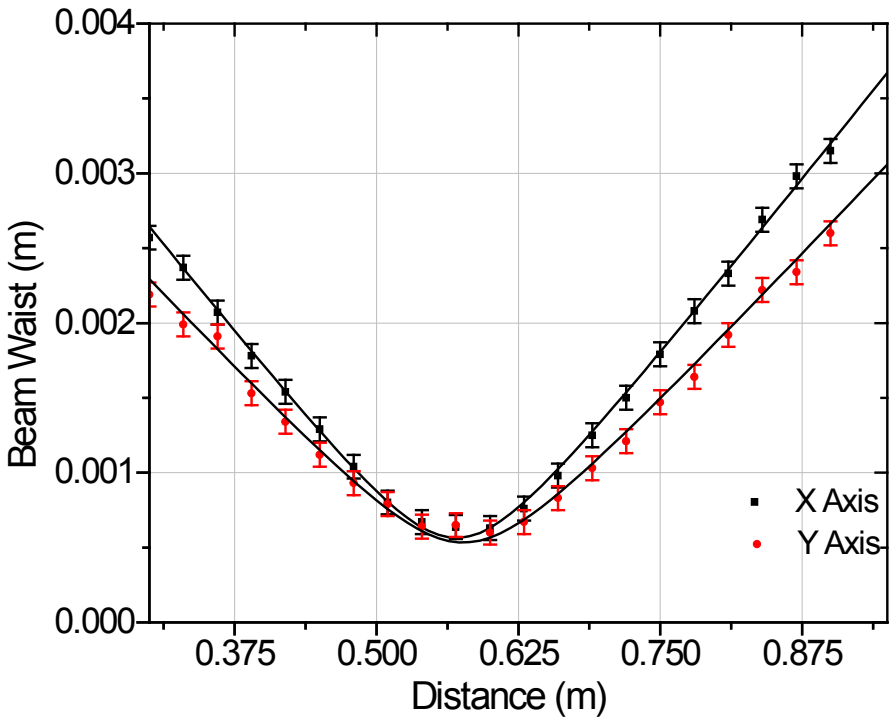


*Figure 28: $M^2$ fitting of the combined beam at 35 W [92].*

Sub-optimal beam quality arises from multiple absorbing elements in the beam path prior to the $M^2$ measurement. For similar high power experiments, we have observed thermal lens effects from the absorption of 2 μm light in the fused silica lenses and optical wedges used to attenuate and guide the beam. In order to minimize these effects, less absorbing lenses and optical wedges made from materials such as Infrasil have been used in subsequent experiments to minimize these thermal issues.

The other factor that contributed to sub-optimal beam quality was the relative pointing stability of the individual laser channels prior to combination. In the experimental setup, two optical tables were used to accommodate the three laser systems. It was therefore necessary for the beams to travel ~5 m before being combined on the appropriate grating. This long path adversely affected the pointing stability, with subtle vibrations of the individual tables causing variations in the measurement of $M^2$ ~5 m from the combining grating (a total of 10 m from the source outputs). The small angular separation of the diffracted orders, along with the physical size of the mirrors and mirror mounts used, dictated a wavelength separation of >10 nm between the source wavelengths and a path length of 2 m between the grating and the final folding mirrors to prevent beam clipping on the opto-mechanical components.

3.3.1.3 Methods to improve SBC

In order to optimize system performance and further scale the combined power, a number of critical improvements needed to be implemented. Incorporation of PM fibers and polarized GMRF stabilized seed lasers, in conjunction with optical isolators, greatly assist power scaling of individual channel powers with narrow linewidths. These improvements were made to the

diffraction grating based feedback system, the middle system in Figure 25, and increased the power beyond 200 W after the SBC tests were completed [93]. Amplifying a GMRF stabilized oscillator operating at 4 W in the power amplifier described in [93] resulted in average powers up to 160 W.

A combining grating with a greater efficiency and damage threshold would be able to withstand higher incident powers before thermal deformation degraded beam quality [63]. However, grating based beam combination does not facilitate closely spaced wavelengths due to the physical constraints associated with beam alignment although advancements have been made to decrease the wavelength spacing using a staircase mirror to pre-compensate the beam spacing prior to the combining grating in a two grating setup [94].

Another approach incorporates long-wavelength bandpass spectral filters to combine beams via a sharp transition edge from high reflectivity to high transmission in a narrow wavelength range. This concept has been demonstrated with >90% combining efficiency [16]. This system, as well as one using a VBG as the combining element [17], has the advantage that wavelength spacing between channels can be minimized to increase spectral density. Using such architectures will facilitate scaling to the kW power level using many moderately powered individual laser systems.

### 3.4 100 W Polarization Maintaining MOPA

This section will describe the system architecture and results for a narrow linewidth integrated PM Tm fiber laser [90]. This laser will serve as the architecture for multiple laser channels, and represents an advancement of SBC concepts at 2 μm. The initial design described

in Section 3.3, provided a quick solution to complete SBC on a single grating and demonstrate the usability of the GMRFs. In order to advance the concept, robust fiber systems with minimal to no alignment were needed, taking advantage of numerous fiber components to integrate the system.

### *3.4.1 System Design*

Following the design of the initial oscillator we use a GMRF to provide wavelength stabilization, as well as the ability to produce many closely spaced wavelengths. Due to the requirements for polarized output, we use the polarization sensitive GMRF in the oscillator. In order to free space couple light to the GMRF an 11 mm aspheric lens with broadband AR coating from 1050 to 1600 nm is used. This light was transmitted through a HWP to ensure the linear polarization reflected from the GMRF matches the slow polarization axis of the fiber. The intracavity fiber face is angle-cleaved to prevent parasitic feedback from the glass/air interface at the fiber tip.

The oscillator contained a ~5 m long section of PM single-mode Tm-doped silica fiber with 10/130 μm core/clad geometry with a core NA of 0.15 (Nufern, Inc.). This active fiber was wrapped around a cylindrical fiber mandrel with an 11 cm diameter and its temperature was maintained at 13 °C by water cooling. The oscillator is pumped with a 35 W, 793 nm laser diode (DILAS Diodenlaser GmbH ) with 105/125 μm diameter multimode fiber. The pump light was delivered through one input fiber from a 2+1 x 1 pump combiner (ITF Labs). The taper fiber bundle contained two pump ports with 105/125 μm multimode fibers geometries and a signal port matched to the PM 10/130 active fiber. One end of the active fiber was spliced to the signal

port of the TFB and the other end was spliced to a section of undoped PM 10/130. The counter-propagating signal port of the TFB was spliced to a chirped fiber Bragg grating (CFBG), written in undoped PM 10/130 μm and fabricated by TeraXion. The CFBG has a reflective bandwidth that is 20 nm broad, spanning 2030-2050 nm, and an average reflectivity of 20%. This element became the output coupler of the fiber laser. The CFBG is used in multiple MOPAs that will be used for SBC; therefore, the bandwidth is large enough to facilitate lasing at any wavelength between 2030 and 2050, with each laser wavelength will be controlled by the reflective properties of the GMRFs. The diagram of this oscillator is shown in the left hand side of Figure 29.

The output of the oscillator is spliced to a dual stage polarization sensitive fiber coupled optical isolator with PM 10/130 fiber pigtails (Shinkosha Co.). This isolator is rated for a maximum incident power of 3 W with >55 dB return loss, 0.5 dB insertion loss, >35 dB PER. The output of the isolator is spliced to the input of a fiber MFA from ITF Labs, which couples the PM 10/130 fiber of the oscillator to the PM 25/400 large mode area (LMA) fiber of the amplifier. The MFA connects the oscillator to the amplifier with a minimal insertion loss of 0.5 dB and no apparent degradation of polarization. The single mode output of the oscillator is effectively coupled to the fundamental mode of the amplifier fiber.

The amplifier contains Tm-doped PM LMA fiber with 25 μm diameter/0.09 NA core and 400 μm diameter/0.44 NA cladding (Nufern, Inc). The amplifier is pumped with six individual 80 W, 793 nm diodes manufactured with 200/220 μm diameter multimode delivery fibers manufactured by QPC Lasers. The diode delivery fibers are spliced to the input arms of a 6+1 x

1 tapered fiber bundle (TFB) pump combiner (ITF Labs), consisting of six pump input fibers with 200 μm diameter/0.22 NA and a signal pass through fiber matched to the active PM LMA 25/400. The maximum available pump power is limited by the 300 W power rating of the TFB and the experimentally measured 75% pump coupling efficiency; however the fabrication of such TFBs is rapidly improving in terms of power handling and coupling efficiency.

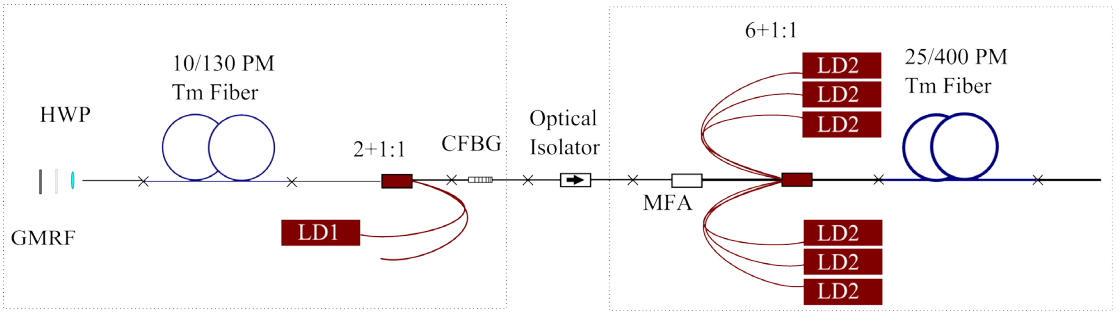


*Figure 29: Quasi- All fiber setup for the 100 W PM system.*

As shown in Figure 28, the output of the MFA is spliced to the input of the 6+1 x 1 pump combiner with little reduction in PER or mode quality. The pump combiner output is spliced to a 5 m length of Tm-doped PM 25/400 and the opposite end of the active fiber is spliced to a 1.5 m length of passive fiber. The active fiber is wrapped around an 11 cm diameter mandrel, and the mandrel and fiber splices are water-cooled for thermal management. The output facet is angle-cleaved to prevent parasitic feedback.

### *3.4.2 Results*

In this MOPA the single-mode oscillator was designed to provide polarized output, with narrow linewidth and a few watts of average power. Using the GMRF, the oscillator operates at 3.2 W for 12 W of launched 790 nm pump light. One MOPA operates with a linewidth of 390 pm at 10 dB from the spectral peak and at a wavelength of 2033.5 nm. In multiple systems the

GMRFs are exchanged to fill the CFBG reflection band between 2030 and 2050 nm; however the linewidth of each laser does not change substantially from the 390 pm described here. The oscillator operates with a PER of 18 dB, in conjunction with the polarization sensitive isolator the PER of the light seeding the amplifier is > 20 dB.

The slope efficiency of the amplifier is 47% with respect to launched pump power, shown in Figure 32 for three lasers; however, the output linewidth broadens during amplification. In the amplification process the linewidth broadens from the input 390 nm to 690 pm at the full power lever of 109 W, both of these linewidths are measured at 10 dB from the spectral peak, Figure 33. The output PER is consistent and >15 dB up to the maximum power. This degradation of the PER from > 20 dB to > 15 dB is present because the splicing of the LMA fiber launches ~ 6% of the total power into the cladding which is not polarization maintaining. The output beam quality, including cladding light, has an $M^2$ of 1.19 and 1.25 along X and Y axes respectively (Figure 33). During amplification, the $M^2$ increases slightly from a value of 1.15 at 10 W output power.

### 3.5 High Power Polarized Spectral Beam Combining

This section focuses on the application of the polarized wavelength stabilized laser channels described in the previous section. The basic principles of SBC, specifically at wavelengths near 2000 nm were described in Section 3.3.1. The work presented there develops and explores some of the challenges to be addressed for SBC in this eye safe wavelength. The most prominent limitations associated with single-diffraction grating beam combining are the optical load and the geometry requirements to combine multiple beams with small wavelength

separation. In order to conveniently combine three channels on a single 6 foot by 3 foot optical table, the wavelength spacing between each laser channel needs to be ~ 10 nm. While thulium offers a large excitable a bandwidth, only a relatively small portion of that bandwidth is within an atmospheric transmission window.

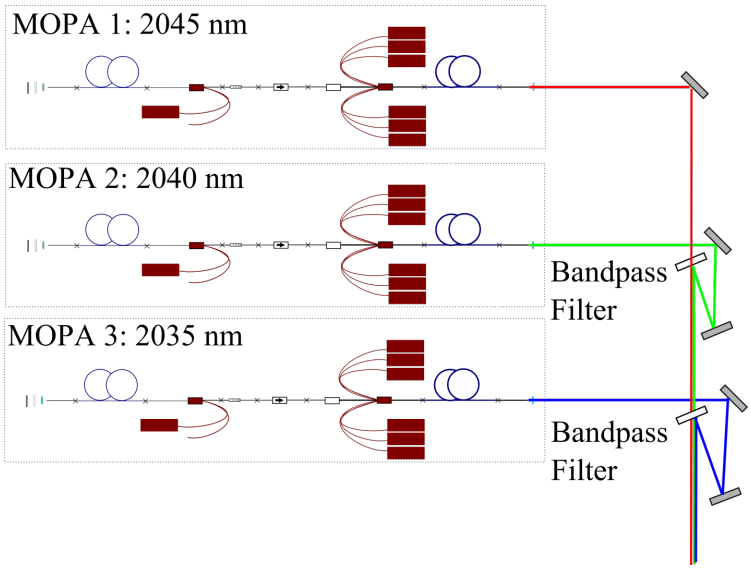


*Figure 30: Schematic of the SBC system using bandpass filters.*

Our work focuses on the ability to develop spectral beam combined systems that can be used in windows in the atmosphere where there high transmission of 2 μm light, namely 2030-2050 nm. In order to do this there is a need for large number of wavelength stacking; therefore, the method of combining needs to be free of geometrical limitations imposed by the combining element.

### *3.5.1 Beam Combining Element*

3.5.1.1. Component Parameters

In order to produce a SBC system that can have small wavelength spacing between laser channels and few geometrical restrictions in alignment, dielectric filters are used to combine wavelengths. Numerous filter designs are possible, including edge, long pass, short pass, and band pass filters. For cases where we want essentially dense wavelength division multiplexing, the filters needed to have extremely sharp edges and operate by angle tuning of the filter. By angle tuning the filters the same design can be used for all channels and by slight angle differences the different wavelengths can be multiplexed. The drawback to combining with angle tuned filters is that the two orthogonal polarizations will see different effective indices from the thin film structure, thus will have a wavelength separation between the two edges. This criterion was the primary reason that the individual channels of each system must be polarized. However, with different polarizations present it should be possible to use both polarization and spectral beam combining with the system.

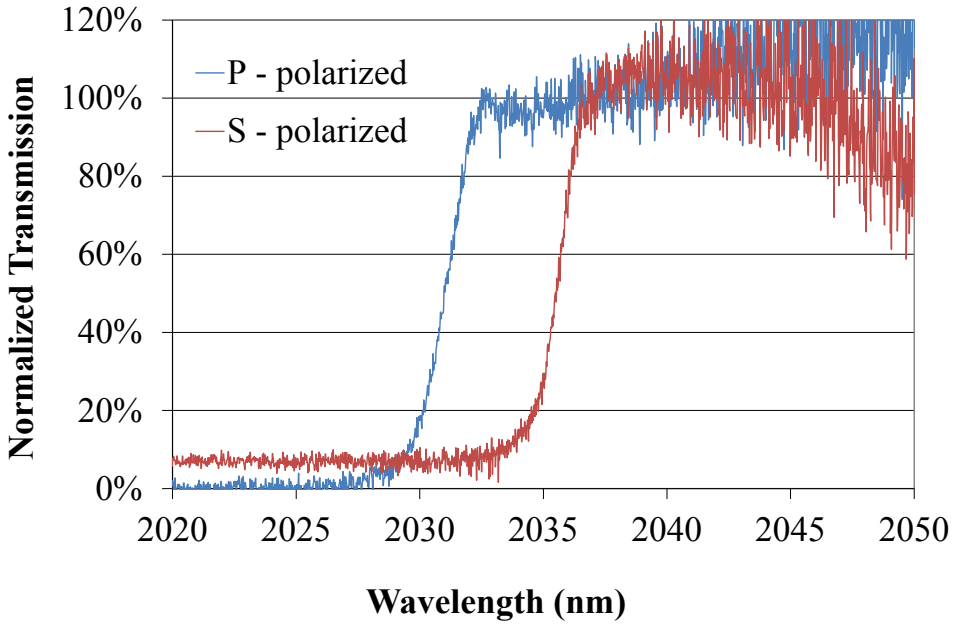


*Figure 31: Filter Edge measured with ASE source*

3.5.1.2 Combining Results

Low power and high power combining tests were completed. Low power tests were completed using only the oscillator outputs. These tests were used to verify the fabrication of the combining element and to measure combining efficiency prior to thermally loading the element. Under low power condition, the three oscillators operated at 2045, 2040, and 2035 nm. Combining of all three channels was achieved with an efficiency of 90.7%. When the wavelength separation was increased to 10 nm (channels 1 and 3) the combination efficiency was 94.9%. The difference between the two cases comes with the insertion of the bandpass filter used to reflect the 2040 nm beam and is associated with the angle tuning and the transmission of the 2045 nm beam.

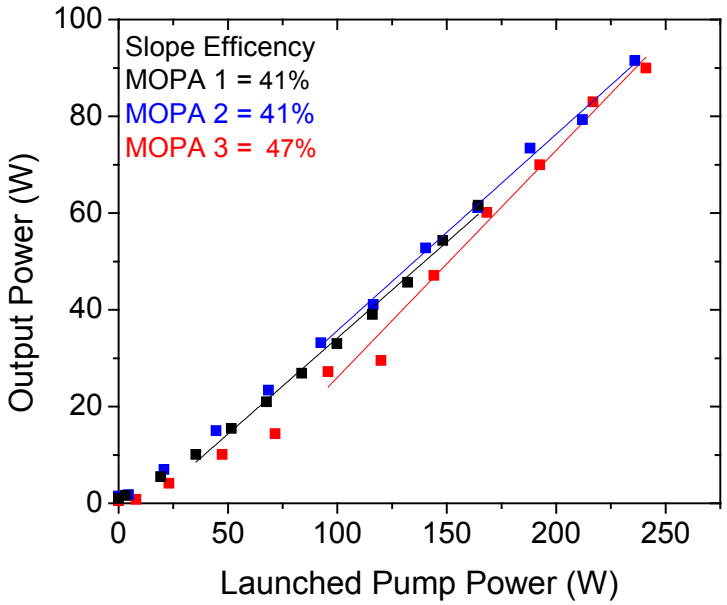


*Figure 32: Slope efficiencies of individual channels used for SBC.*

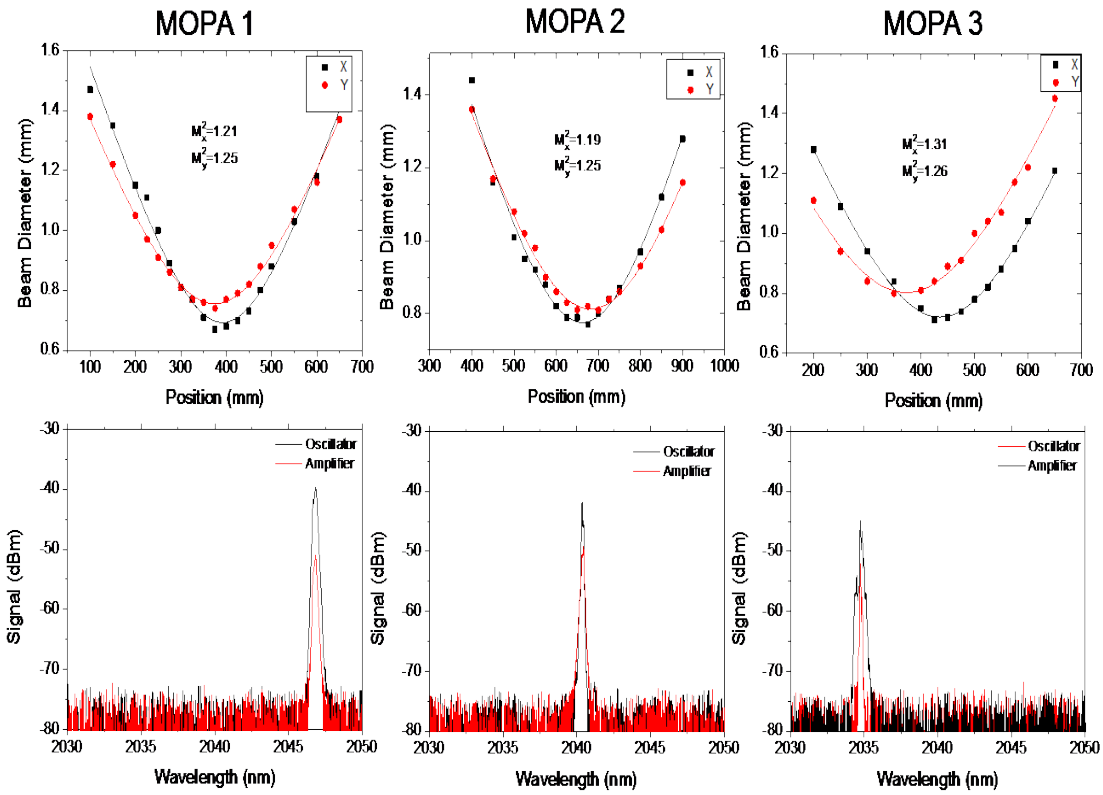


*Figure 33: Curve for $M^2$ measurment and spectral characteristic of each individual MOPA system.*

Prior to high power testing each system was tested to the maximum pump power that the TFB would allow, ~ 300 W. For each system the beam quality was measured using an $M^2$ technique, as well as slope efficiency, PER, and spectral output. Slope efficiencies of the individual channels varied between 41-47% as shown in Figure 32. Figure 33 contains both the spectral and $M^2$ data for the individual MOPA systems. The individual MOPA systems produced $M^2$ ranging from 1.19-1.31.

The output of all three MOPAs was combined with a total efficiency of 89%. The incident powers of each individual MOPA were 87, 99, and 98 W. The MOPA with the lowest power was ~ 10 W lower than the other channels at full power because the mode quality transmitted through the TFB was sub-optimal, causing excitation of higher order modes in the fiber. Polarization of these higher order modes drifted with time, therefore the reflected power from the bandpass filter varied due to the polarization state. After the combining experiments were completed, the TFB in MOPA 3 was exchanged and the mode quality and polarization was no longer an issue. The total combined power was 253 W, corresponding to a total combining efficiency of 89%. The electrical-to-optical efficiency of this system was ~ 35%. The beam quality of the combined beam was measured using the same $M^2$ methodology as used to characterize the individual beams. The resulting beam quality was found to be 2.0 along X and 1.7 along Y. The corresponding data is shown below, along with far field beam images of the output of each MOPA and the combined beam. Data for the combining efficiency and output power is shown in Figure 34.

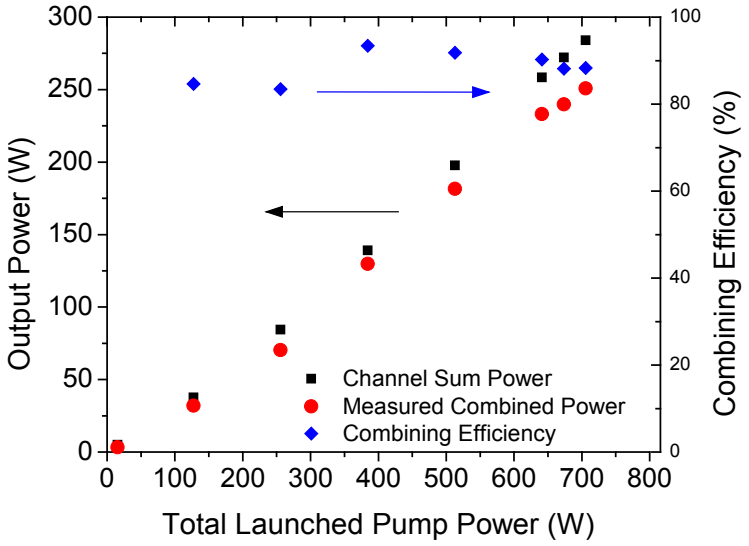


*Figure 34:Spectrally beam combined power showing the measured power, an addition of the individual channels, and an overall combining efficiency.*

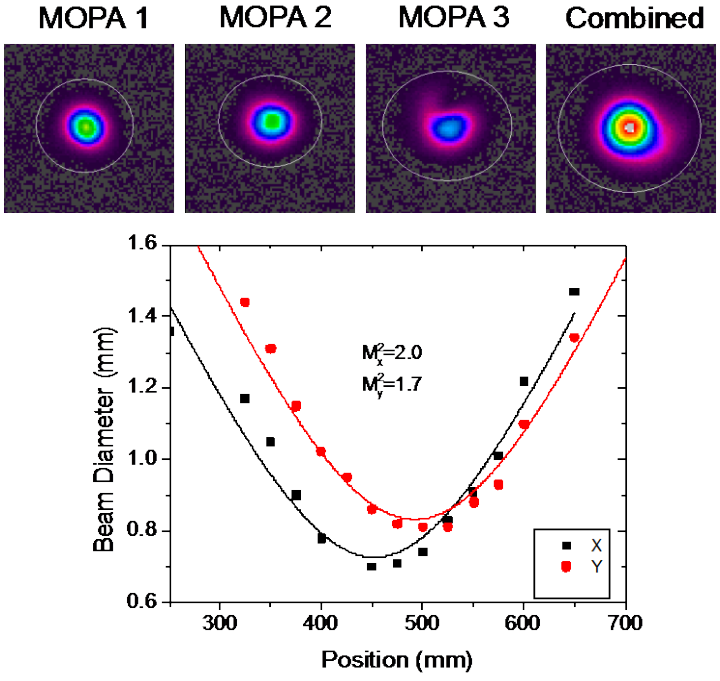


*Figure 35: Beam images of each individual MOPA channel and combined beam as well as $M^2$ of the combined beam.*

# CHAPTER 4: THEORETICAL DEVELOPMENT OF FEMTOSECOND PULSE GENERATION AND AMPLIFICATION

## 4.1 Introduction

### *4.1.1 Pulse Propagation*

4.1.1.1 Nonlinear Schrödinger Equation

In order to describe the propagation of pulses in an optical fiber, one must begin with Maxwell's equations and derive the wave equation. From the wave equation, another lengthy derivation is needed [58] to reach the nonlinear Schrödinger equation

$$\frac{\partial A}{\partial z}+\frac{\alpha}{2}A+\frac{i\beta_2}{2}\frac{\partial^2 A}{\partial T^2}-\frac{\beta_3}{6}\frac{\partial^3 A}{\partial T^3}=i\gamma\left(|A|^2 A+\frac{i}{\omega_0}\frac{\partial}{\partial T}\left(|A|^2 A\right)-T_R A\frac{\partial|A|^2}{\partial T}\right) \qquad (14)$$

This final equation is a simplification describing a few physical processes that can occur as a pulse propagates with a slowly varying envelope in a fiber. Essentially the nonlinear Schrödinger equation describes how a slowly varying amplitude $A=A(z,t)$ propagates in a medium with dispersive, loss/gain, and $\chi^3$ nonlinear processes. In this equation $\alpha$ represents loss, the terms $\beta_2$ and $\beta_3$ come from a Taylor series expansion of the propagation constant $\beta(\omega)$, which correspond to the group velocity dispersion (GVD) and third order dispersion (TOD), respectively. The terms on the right hand side will be discussed in the upcoming section but represent some of the nonlinear terms possible in the propagation of a pulse. In Equation (14) the nonlinear processes described are self-phase modulation, self-steepening, and Raman scattering.

4.1.1.2 Split-Step Fourier Transform

One method to model how pulses propagate in a length of fiber is to use split-step Fourier Transform. In this method the terms related to dispersion and loss are separated from nonlinear phenomena [58], as follows

$$D = -\frac{-i\beta_2}{2}\frac{\partial^2}{\partial T^2} + \frac{\beta_3}{6}\frac{\partial^3}{\partial T^3} - \frac{\alpha}{2} \tag{15}$$

$$N = i\gamma(|A|^2 + \frac{i}{\omega_0}\frac{1}{A}\frac{\partial}{\partial T}(|A|^2 A) - T_R\frac{\partial|A|^2}{\partial T}) \tag{16}$$

In reality these terms are not independent of each other, but these quantities can be approximately split where the dispersive terms affect the pulse duration while the terms for nonlinearities affect the spectral properties. For modeling, the fiber is divided into small segments and a two-step numerical calculation is made to determine the electric field in a segment of fiber. In one step the dispersion and losses modify the electric field as phase terms then a Fourier transform is performed. With this transformed field, the terms for nonlinearities are applied as phase terms then an inverse Fourier transform is performed. The results of the previous step become the initial conditions for the subsequent step, and the process continues along the length of the fiber. In this thesis, commercial split-step Fourier transform software, FiberDesk, is used to compare model and experimental results [95].

### *4.1.2 Dispersion*

A key component to pulse propagation in ultra-short pulse (USP) systems is the effect of frequency chirp caused by GVD. Chromatic dispersion in materials results from the fact that the

refractive index of a material is frequency dependent. Figure 36 shows refractive index for fused silica glass from 0.5-2.5 μm as calculated from Sellmeier equation.

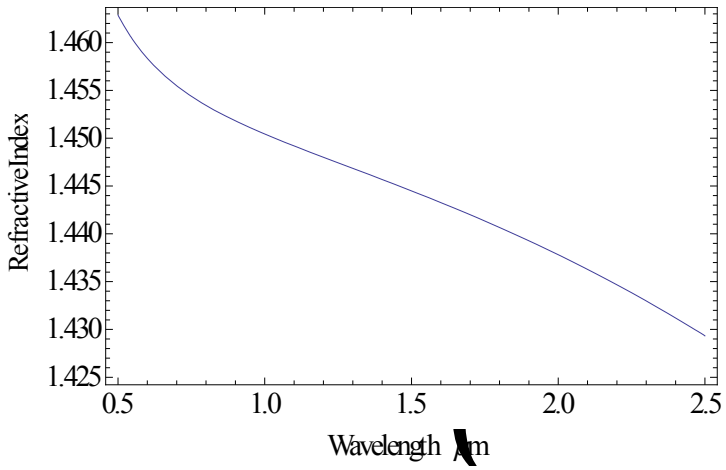


*Figure 36: Refractive index of fused silica glass from Sellmeier formula.*

Chromatic dispersion determines the propagation speed of different frequency components and manifests itself as pulse broadening in ultrashort pulses. To describe this we most look at the Taylor series expansion of the propagation constant $\beta = \frac{n(\omega)\omega}{c}$.

$$\beta(\omega) = \beta_0 + \beta_1(\omega - \omega_0) + \frac{1}{2}\beta_2(\omega - \omega_0)^2 + \frac{1}{6}\beta_3(\omega - \omega_3)^3 + \cdots \qquad (17)$$

where

$$\beta_m = \left(\frac{d^m \beta}{d\omega^m}\right)_{\omega=\omega_0} \quad (\text{m}=0, 1, 2\ldots) \qquad (18)$$

The first derivative of the propagation constant is referred to as the group velocity and the second derivative as the GVD. Both the sign and value of the GVD will become important to the discussion of pulse solutions and pulse regimes of mode-locked fiber lasers and is shown in Figure 37.

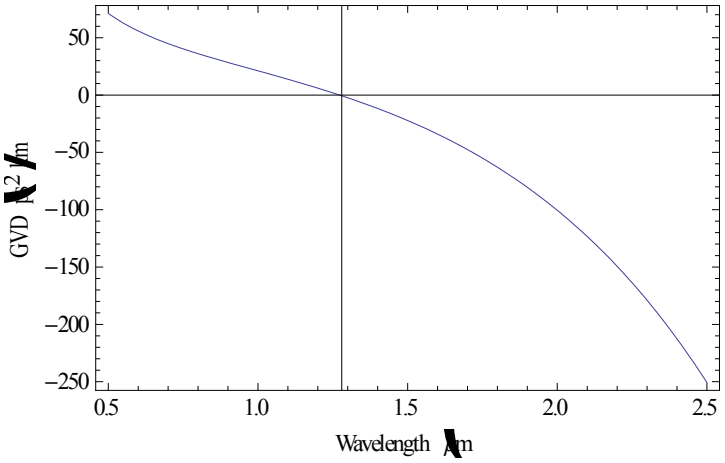


*Figure 37: Group velocity dispersion of fused silica plotted against wavelength highlighting the zero dispersion wavelength*

In Figure 37, the group velocity dispersion of fused silica is plotted against wavelength from 0.5 – 2.5 μm and the zero dispersion wavelength is highlighted. The primary mechanism that governs the $\beta_2$ value of the fiber is the material dispersion of the host and any dopants. However, because the fiber is a waveguide, the material index and the effective mode index are slightly different, with the effective mode index, being lower. Because the waveguide causes this lower effective mode index the overall dispersion is a combination of the material dispersion and this waveguide term. In most cases, this waveguide term does not affect the overall $\beta_2$ value. However, by changing the core diameter and NA of the fiber, this waveguide term can become more dominant and shift the zero dispersion wavelength (ZDW) [58].

One of the major considerations for pulse propagation is the GVD sign because the sign of chirp causes different effects in the presence of nonlinearities. Positive values of GVD ($\beta_2>0$) produce normal dispersion while negative values ($\beta_2<0$) produce anomalous. Whether the dispersion is anomalous or normal, the pulse broadens temporally when an unchirped pulse

propagates in the absence of nonlinearity. However, the effects of intensity dependent nonlinearities in fibers need to be considered to describe their pulse propagation.

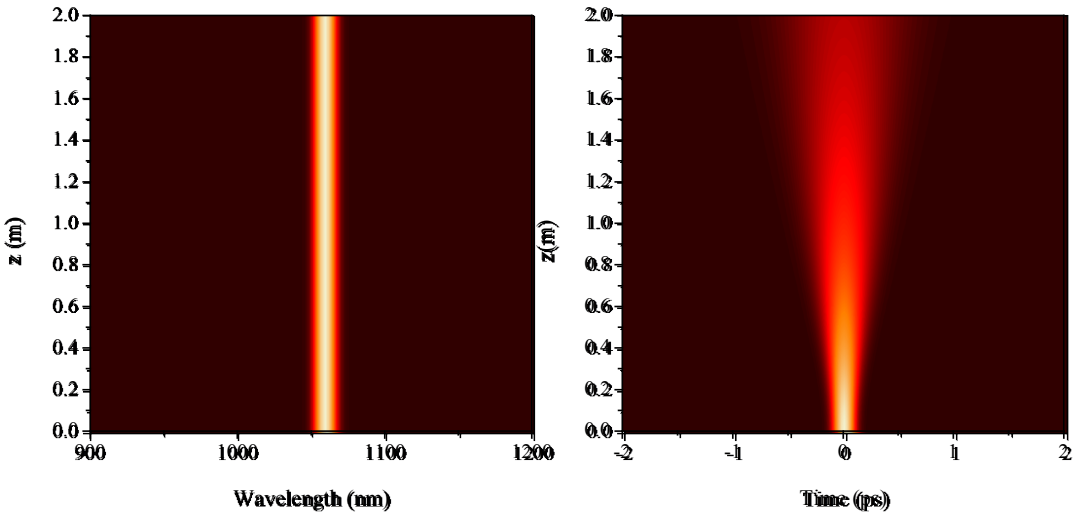


*Figure 38: Simulation of broadening due to GVD.*

GVD is the primary contribution of linear pulse broadening mechanisms, however, when dealing with ultrashort pulses higher-order dispersive terms have an increased contribution. When $\Delta\omega << \omega_0$ the higher order dispersive terms ($\beta_3$, $\beta_4$…) can be considered negligible [58]. After GVD the next higher order term is third order dispersion (TOD), which makes the pulse's intensity profile asymmetric

### *4.1.3 Nonlinearities*

4.1.3.1 Self Phase Modulation

Self-phase modulation (SPM) is an intensity dependent nonlinear effect, which manifests itself in a change of the temporal phase of a pulse, thereby modifying the pulse's spectrum. The

first observations of SPM in silica optical fibers were reported in 1978 in a paper by R. H. Stolen et al. [61]. Although SPM modifies the spectrum of the pulse, the effects are not independent of the linear frequency chirp caused by GVD. In the theoretical case of a pulse with linear chirp propagating at the zero dispersion wavelength the broadening or narrowing of the pulse depends on the sign of the chirp. Positive chirp leads to spectral broadening while the opposite is true for negative chirp in the presence of SPM. Moreover, when including a nonzero GVD and the effects of SPM; the two effects interplay depending on the magnitude of these effects in comparison to one another.

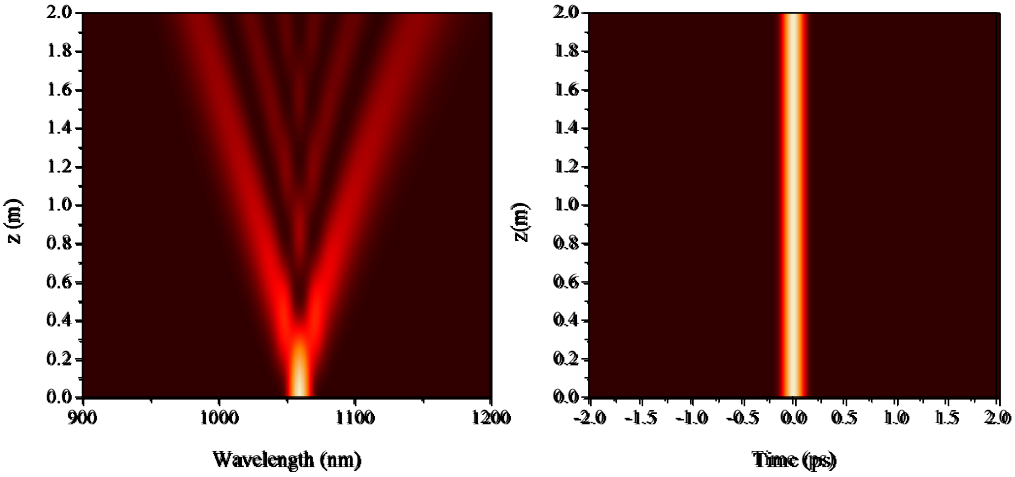


*Figure 39: Example of the effect of SPM as a pulse of light propagates in a fiber without GVD*

Figure 39 is a plot showing the evolution of SPM during propagation along a length of fiber with no GVD ($\beta_2$=0). As light propagates, the pulse spectrum broadens or narrows, depending on the input chirp, in Figure 39 there was no initial chirp on the pulse. The figure shows an oscillatory behavior due to constructive and destructive interference. As SPM generates new frequencies there is a chirp added to the pulse. Thus, different parts of the spectrum can have the same instantaneous frequency chirp causing interference.

### *4.1.4 Interplay between Nonlinearities and Dispersion*

The NLSE Equation 14 highlights that there is interplay between the nonlinear terms and the dispersive terms; therefore in realistic systems both need to be taken into account. A number of specific effects occur because of the interplay between these terms. In Section 4.2.3.1 there will be a more in depth discussion of solitons, specifically soliton based mode-locking, but the principle of solitons corresponds to a special case of interplay between GVD and SPM. In the case of temporal solitons, a pulse is travelling in a fiber with anomalous dispersion, thus the $\beta_2$ value is negative and the phase added through this propagation is negative. Conversely, the phase generated by self-phase modulation is positive. Thus, as a pulse propagates with the correct peak power the dispersive and nonlinear terms cancel and the pulse will propagate the length of fiber invariant in time. In the case of a fundamental soliton, the electric field has a hyperbolic secant shape in time. If the peak power is too large higher order solitons can propagate and create a periodic evolution of the pulse both in the spectral and time domains, without other higher order effects present. An example of higher order soliton propagation is seen in Figure 40. Solitons are defined by the parameter $N$ that takes into account the dispersive length, $L_{D,}$ and nonlinear length, $L_{NL,}$ which are defined as

$$L_D = \frac{T_0^2}{|\beta_2|} \tag{19}$$

$$L_{NL} = \frac{1}{\gamma P_0} \tag{20}$$

Where $T_0$ is the pulse duration, and $P_0$ is the peak power [58]. To determine the soliton order the following equation is used

$$N^2 = \frac{L_D}{L_{NL}} = \frac{\gamma P_0 T_0^2}{|\beta_2|} \qquad (21)$$

A value of $N$=1 corresponds to a fundamental soliton [58].

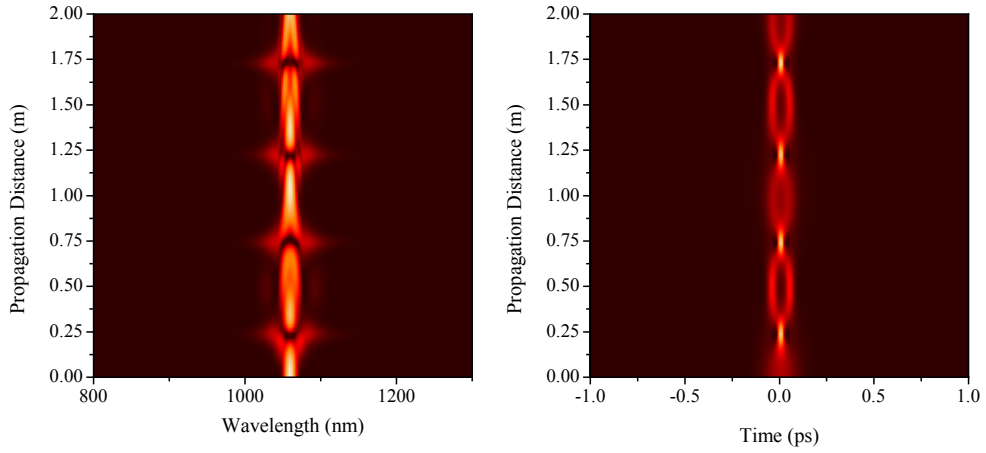


*Figure 40: Example of a higher-order soliton (N=3) neglecting higher-order dispersive effects or Raman scattering.*

One other interplay worth noting is in the presences of gain, positive $\beta_2$ and SPM, in which a pulse can broaden in spectral and time domains while maintaining a linear chirp across a pulse as it amplifies. This occurs because the pulse evolves asymptotically and the pulse shape becomes nearly parabolic. This evolution is important for amplifiers, as pulses can broaden to fill the gain bandwidth and maintain a linear chirp that can be easily compensated. Therefore, amplified compressed pulses can have a shorter duration than the input pulse [96,97].

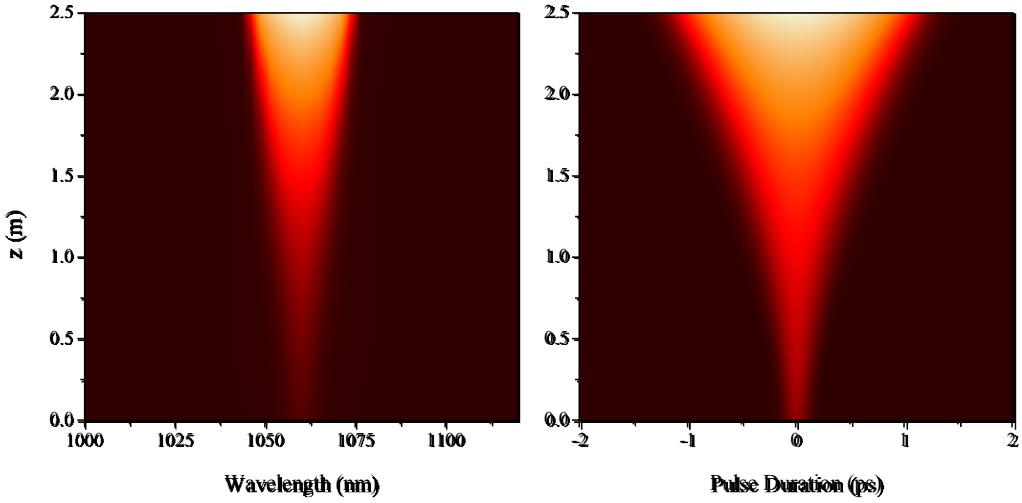


*Figure 41: Model from FiberDesk showing the evolution of a self-similar pulse in an amplifier*

## 4.2 Pulse Generation

### *4.2.1 Description of Mode-Locking*

Mode-locking of lasers is used to generate ultrashort pulses by locking the phase of many longitudinal modes of a cavity within the gain bandwidth of the dopant. By enforcing the phase relationship between the axial modes, constructive interference causes the coherent radiation to organize in pulses in the time domain, at a frequency corresponding to the roundtrip time or an integral multiple of the cavity. As pulses circulate through the cavity, the pulse can shorten until the spectrum becomes so large that pulse lengthening mechanisms, or spectral narrowing processes, occur. In order to produce the phase relationship within the cavity, mechanisms need to be employed by active or passive means [55].

### *4.2.2 Passive Mode-Locking*

Mode-locking of lasers can be induced either through passive, active, hybrid methods. In this thesis, passive mode-locking techniques will be used to create femtosecond pulses in a fiber

laser using saturable absorbers as the mode-locking component. Elements used as saturable absorbers are optically absorbing media whose absorption decreases with the optical intensity of a pulse. Mode-locking due to saturable absorption is explained using an absorber whose relaxation time is on the time scale of the pulse length. Noise fluctuations from the stimulated emission of the laser begin to saturate the absorber. As a pulse begins to form, the intense peak of the pulse passes through the bleached absorbing media whereas the lower intensity wings are absorbed. Through interplay of the gain medium and the saturable absorber, pulse shaping occurs and continues until the gain bandwidth and pulse width reach a stable solution. A passively mode-locked laser of this type usually consists of both a time-dependent loss and gain. Saturable absorber mechanisms in lasers depend on the relaxation time ($\tau_A$) of the absorbing media and how it compares to the pulse width ($\tau_P$) of the pulses generated. These two types of media are divided into two forms: slow saturable absorbers, where $\tau_p << \tau_A$ and fast absorbers where $\tau_A < \tau_p$. The dynamics of slow saturable absorbers are well documented in multiple publications [98,99] and are not a primary means for mode-locking fiber lasers.

4.2.2.1 Carbon Nanotubes

A SA garnering attention recently is single-walled carbon nanotubes (SWCNT). Carbon nanotubes were first discovered in 1991 at NEC by Iijima [100]. SWCNTs were first demonstrated as SAs for fiber lasers in 2004 [101]. SWCNTs act as saturable absorbers through excitonic absorption processes in semiconductor nanotubes with ultrafast relaxation times possible. SWCNT relaxation times have been measured using a pump probe experiments to be 370 fs when spray coated on a quartz substrate [102].

SWCNT are formed from cylindrically shaped carbon atoms in a hexagon honey comb-like geometry. Diameters of the cylindrical structure are typically on the order of nm's while the lengths are 10's of μm long. Due to the crystallographic structure of the 2-D nanotube, the SWCNT possess semiconducting, metallic or semimetallic properties. The chirality of the SWCNT nanotube governs the properties of the device and ones that exhibit semiconductor behavior are useful for saturable absorption. Set *et al*, argues that the saturable properties of a SWCNT come from excitonic absorption because of its ultafasat recovery time [101]. Another benefit of SWCNT is the optical absorption properties are inversely dependent on the size of diameter because the bandgap varies inversely with the diameter [102].

The use of SWCNT as fast SA's has been realized in crystalline solid-state lasers and fiber lasers, where a number of techniques to deposit the nanotubes. In the first fiber laser demonstration a SWCNT mixture was spray coated on a substrate and sandwiched between two AR coated substrates. In this design at 1.5 μm, the laser operated in a ring cavity and light was focused through the SA in free space configuration producing an autocorrelation of 1.7 ps with 3.7 nm spectral bandwidth. Using a linear cavity with a reflective SA, the authors were able to achieve 13.6 nm bandwidth resulting in Gaussian pulses of 318 fs [67]. Another deposition technique involves optically driving the deposition of the SWCNT on the fiber facet. In this technique, SWCNT are dispersed in ethanol and agitated using an ultrasonic bath, and a fiber facet is place in the nanotube mixture with light transmitted through the fiber. The SWCNT overcome the scattering forces and are deposited on the fiber facet providing an effective SWCNT SA [103]. The coated fiber tips are then incorporated into the fiber laser cavity. Mode-locked lasers have been demonstrated at multiple wavelengths using this method [69]. Another

variation on this technique has been proven at 1, 1.5 and 2 μm by coating an adiabatic fiber taper with a SWCNT polymer composite. The fiber is tapered to small diameters (3-7 μm) so the evanescent portion of the guided light interacts with the SWCNT composite [104,105].

4.2.2.2 Nonlinear Polarization Evolution

Nonlinear polarization evolution (NPE) is the result of intensity dependent nonlinear effects within an optical fiber that produce nonlinear phase changes. Physically, elliptically polarized pulses interacts with the $\chi^3$ of the fiber to induce a nonlinear birefringence due to the intensity-dependent Kerr effects of SPM and Cross Phase Modulation [106]. In a system where the peak power of the pulse does not induce nonlinear rotation, the pulse will have a constant polarization versus time/position along the fiber. When a pulse has sufficient peak power to induce nonlinearities, the peak of the pulse will induce a polarization change; however, for the lower intensity wings the polarization will not change. The use of NPE has drawbacks because the polarization state of the fiber can be dependent on bends in the fiber as well as environmental conditions. By inserting a QWP, a HWP, and a polarization discriminating element such as a polarizing beam cube after the fiber, it is possible to achieve intensity dependent transmission [107,108].

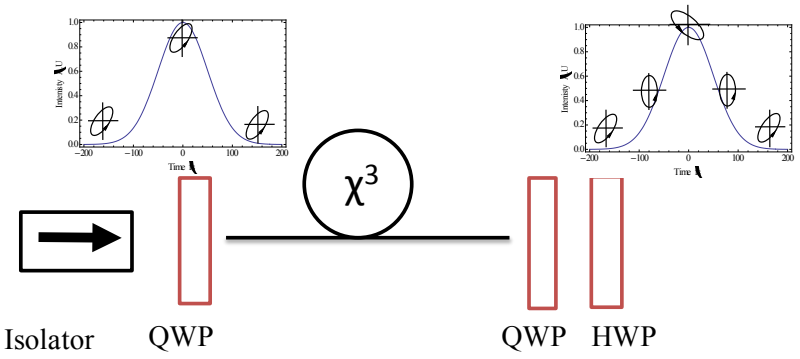


*Figure 42: Basics of NPE based mode locking in fiber lasers. The pulses are propagating from the left to right and the images show a representation of how the polarization changes in the nonlinear media.*

The use of NPE has become a primary method to test the limits of ultrashort oscillator performance, both in terms of pulse widths and pulse energies. The shortest pulses from Yb oscillators have been produced using well optimized systems using NPE, these values include 28 fs for a system correcting TOD [109] and 36 fs for a system with no TOD correction [75]. NPE has also been the mode-locking mechanism in the initial development of stretched pulse oscillators in Er fibers, first optimized in 1992 by Tamura [79] with 77 fs pulses. Some of the most recent work in Tm fibers has used NPE as the mode-locking mechanism to produce pulse with energies >4 nJ and pulse widths <300 fs [80, 81]. In addition this method was used to produce the first Tm mode-locked laser [82].

One of the fundamental drawbacks of NPE based oscillators is the environmentally instability. Temperature fluctuations or other environmental effects that influence polarization can disrupt mode-locking, requiring the user to optimize the setup. One solution to the environmental stability was published in 1993 by M. Fermann et al. by employing a polarization maintaining fiber in the system producing a 200 fs 70 pJ system in Er [73].

### *4.2.3 Fiber Regimes and Limitations*

4.2.3.1 Soliton

Undoped fibers operating in the anomalous dispersion regime can lead to interesting pulse dynamics when coupled with non-linear effects enabling pulses to propagate along the fiber without changing pulse duration. This type of pulse was named soliton after the effect of solitary waves. Solitons are characterized by a pulse with a hyperbolic secant pulse shape and are formed when the phase introduced by SPM is opposite that of the GVD. Since the nonlinear phase and dispersive phase delay need be similar to facilitate pulse propagation, the power of the fundamental soliton is limited and can be described by [59]

$$P_s = \frac{|\beta_2|}{\gamma \tau^2} = \frac{3.11|\beta_2|}{\gamma \Delta \tau^2} \qquad (22)$$

In practice fiber lasers operating in the soliton regime are built using a ring cavity, where mode-locking typically starts from noise for simplicity. Ring cavities are best optimized with linear polarization control in the cavity and optical isolators to prevent competition between clockwise and counter-clockwise propagating pulses. Soliton based fiber lasers are limited to energies ~0.1 nJ with pulse duration at 100's of femtoseconds because of the phase delay restrictions in the fiber [76]. The phase is typically limited to phase delays on the order of π. In soliton based lasers, if one ignores the gain bandwidth limitations, energy and pulse duration ($\tau$) can be approximated by [83]

$$E_s = \frac{3.53\sqrt{|D_2|}}{\gamma L} \qquad (23)$$

One characteristic feature of soliton mode-locked fiber lasers is Kelly side band formation that produces sidebands in the spectrum of the source. The sidebands form due to periodic disturbances as the pulse propagates in the laser [84]. As the soliton pulse propagates in a cavity the soliton lose energy at splices, output couplers, and other components in the cavity. Therefore, the soliton energy and peak power vary periodically as the pulse propagates and experiences gain and loss. In order to maintain the soliton some of the energy is shed into a dispersive wave. Because of the periodic perturbation, the dispersive wave is resonantly enhanced in a laser [107].

4.2.3.2 Dispersion-managed Solitons

Dispersion managed solitons are solutions to the NLSE that occur when pulses propagate through regions of both positive and negative GVD with a total net dispersion close to zero. Laser cavities with alternating GVD, known as stretched pulse lasers, produce pulses with higher energies than those of fundamental solitons. Theoretical developments for dispersion managed soliton propagation in communication systems is found in articles by Smith [85] and Mu [86]. In the first experimental work by Tamura et al., positive dispersion occurred in the Er doped fiber and anomalous was provided by SMF-28. This first example of a stretched pulse oscillator produced self-starting pulses with energies of 90 pJ and pulse widths of 77 fs [79]. The segments of opposite dispersion cause the pulse width to stretch and compress as it circulates in the cavity. The variation in pulse width effectively reduces the average peak power in the cavity allowing the net nonlinear phase shift per pass to be lower than that of a soliton system. Aside from the higher energy potential, the stretched pulse cavity also produces spectrally cleaner pulses.

Subsequent studies by Tamura et al. characterized the properties of stretched pulse oscillators, in terms of system layout and net dispersion values [87, 88].

Experimentally, cavities with intracavity dispersion management have been used in Er, Yb, Nd, and Tm dopants. In the former paragraph, the initial realization of stretched pulse oscillators was discussed in Er-dopants. However, the majority of work for high power short pulse oscillators has been utilized in Yb-dopants to produce lasers operating in the wave-breaking free regime as well as producing the shortest pulsed fiber lasers [74, 89]. Optical wave-breaking is a phenomenon that occurs when SPM effects dominate over GVD, and temporal oscillations occur near the pulse edges and generate spectral side lobes. One of the most recent advances in mode-locked Tm fiber lasers was reported in 2008 with the incorporation of dispersion management, through a 4f telescope and grating pair, to produce pulses both in the stretched pulse and slightly anomalous pulse regimes [81, 90]. By incorporating the dispersion compensation, < 300 fs pulses with pulse energies >4 nJ were realized.

## 4.3 Amplification

### *4.3.1 Limitations to Direct Amplification*

Many applications need higher energies or peak powers than what a single mode-locked oscillator can generate. Therefore, amplification of pulses is needed to increase this energy or peak power. During direct amplification of the pulses, the two limitations are the dispersion in the system and the nonlinear degradation of the pulse. If a short pulse enters the fiber amplifier, it will experience a temporal broadening due to the dispersion in the fiber; thus reducing achievable peak power. The primary limitation to direct amplification is the accumulation of

nonlinear phase as the pulse propagates in the fiber, primarily from SPM, until the pulse becomes distorted to the point of wave breaking. However, depending on the dispersion of the fiber and amount of amplification, these dispersive and nonlinear effects can be used to amplify pulses to modest energies.

### *4.3.2 Raman-Soliton Self-Frequency Shift*

The nonlinear Schrödinger equation includes higher order nonlinearity due to Raman scattering. In the case of short pulses < 1ps, where there is significant bandwidth, Raman gain is important because the higher frequency spectral components can transfer energy and be amplified by the Raman gain. This process, known as intrapulse Raman scattering, leads to a phenomena where energy from the higher frequency components shifts to lower frequency components, referred to as a Raman-induced frequency shift (RIFS) [58]. Agrawal [58] describes this process using moment equations to gain physical insight on the process of a RIFS. Both Agrawal and Gordon [110], describe this Raman effect with different method but the results of both analysis agree that the scaling of the frequency shift $\Omega_p$ scales with the pulse duration ($T_0$) as $T_0^{-4}$. Agrawal [58] shows this as

$$\Omega_p = -\frac{8T_R\gamma P_0}{15T_0^2}z \equiv -\frac{8T_R|\beta_2|}{15T_0^{-4}}z \qquad (24)$$

As mentioned in the last section when a pulse with high enough energy travels in an anomalous dispersion fiber, higher order solitons form. In the presence of Raman scattering and self-steepening higher order solitons do not propagate, but rather break up temporally and spectrally into their constituent soliton components in a process known as soliton fission [111].

Through the soliton fission process, a Raman soliton forms containing the properties of a fundamental soliton, however it temporally separates from the input pulse as it propagates in the fiber due to differences in the group velocity dispersion Figure 43 shows a simulation of the generation of a Raman soliton self-frequency shift in passive fiber with 150 fs pulse input into an anomalous dispersion fiber. In the spectral domain, the pulse travels ~0.03 m before the soliton fission process forms the Raman soliton and transfers energy from the high frequency components to the low frequency components as it propagates in the medium. In the temporal domain, the fundamental soliton shifts in time due to the difference in the GVD of the input pulse and the Raman soliton.

This SSFS process can be initiated in a doped and pumped fiber, where there soliton shift is controlled by the pump power. This has been used to shift pulses from Er/Yb fiber to longer wavelengths [112,113]. This process of active generation of the SSFS has been used to generate fundamental soliton pulses at wavelengths near 2000 nm [114,115]. This amplifier does generate shorter pulses and amplifies the energy from the initial input pulse, but is limited by the number of higher order solitons generated.

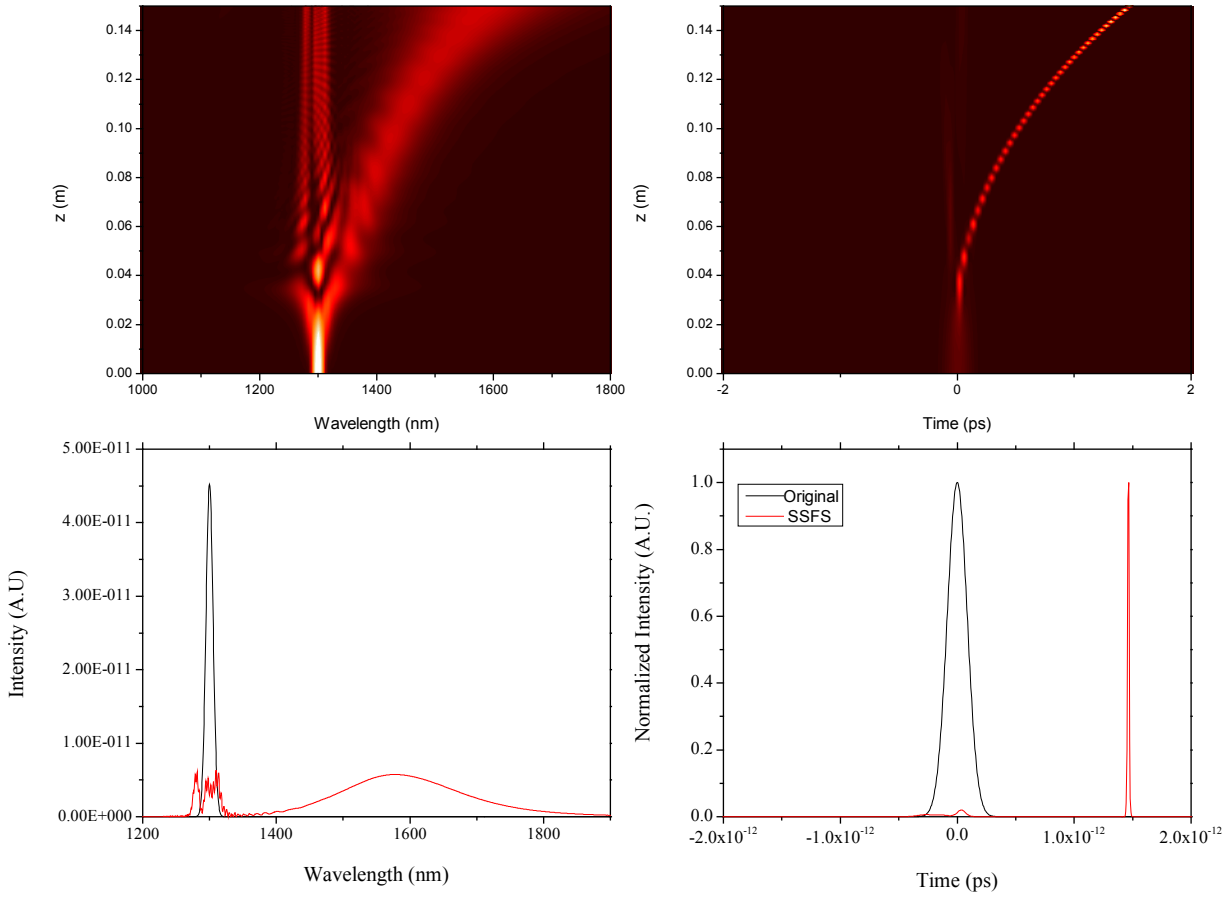


*Figure 43: Computer model of a pulse travelling in an anomalous dispersion fiber that can generate a Raman soliton frequency shift.*

### *4.3.3 Chirped Pulse Amplification*

The primary method for overcoming the limitations of direct amplification or using a Raman-soliton self-frequency shift amplifier is to use the well-known process of chirped pulse amplification (CPA) [116]. Pulses are temporally stretched in order to reduce peak power during the amplification process. After amplification the pulses are recompressed to reach a higher peak power. However, using this process the nonlinearities have to be managed so the pulses can be recompressed to the original duration.

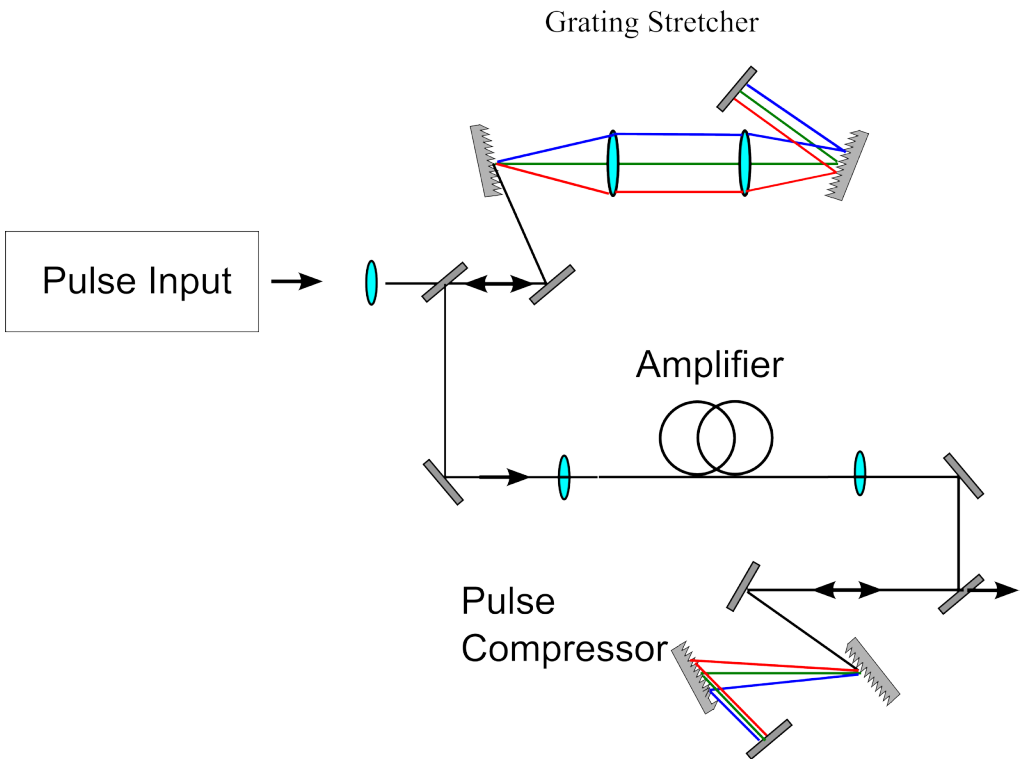


*Figure 44: A schematic showing a simple Fiber CPA system with a grating stretcher and compressor*

Intensity dependent nonlinearities ultimately limit amplification in CPA systems, particularly SPM. SPM adds additional nonlinear phase to a pulse that can lead to nonlinear chirp that cannot be compensated through linear compression techniques. The additional phase from SPM is described in the NLSE by [58]

$$d\phi_{SPM}(z,T) = \gamma \left| A(z,T) \right|^2 dz \qquad (25)$$

Where $A(z,T)$ is the slowly varying field amplitude, $z$ is the propagation distance and $\gamma$ is the nonlinear parameter

$$\gamma = \frac{n_2 \omega_0}{c A_{eff}} = \frac{2\pi n_2}{\lambda A_{eff}} \qquad (26)$$

Where $A_{eff}$ is the mode field area and $n_2$ is the nonlinear refractive index. The B-integral is used in order to quantify the amount of nonlinear phase accumulated due to SPM and other nonlinearities and is defined as

$$B = \frac{2\pi}{\lambda}\int_0^z n_2 I(z)dz \qquad (27)$$

where *I(z)* is the intensity of the pulse as a function of distance propagated in the fiber. Typically, B-Integral values less than π radians are considered in the linear regime and pulses can be recompressed [117]. In the instance that there is excessive nonlinear phase accumulation, the pulse experiences pulse broadening and a change in the wing structure of the pulse. Thus, upon recompression the peak power is reduced.

Examining the nonlinear parameter γ shows $\gamma \propto (\lambda A_{eff})^{-1}$. This proportionality shows that using fibers with larger core sizes and/or longer wavelengths will decrease the amount of nonlinear phase accumulation.

4.3.3.1 Pulse Stretching and Compressing Techniques

The simplest, yet most limited method for temporally dispersing a pulse in a fiber CPA system is to use fiber for the stretching and compressing. The limitations in this method are evident as SPM will be the limiting factor, especially in the compression stage. Another drawback is in conventional fiber where the TOD is always positive, therefore generation of extremely short pulses will be hindered by this extra term. However, in Tm doped CPA systems, pulse stretching through fiber has been the only method shown thus far [113,118,119].

The conventional method, following from amplification of solid-state lasers, is to use dual diffraction grating based stretchers and compressors. A broadband pulse incident on a diffraction grating will spread into its constituent frequencies. By constructing an appropriate optical system, this dispersion is utilized to create a wavelength dependent variation in optical path length to temporally disperse the pulse. There are two basic designs to design a stretcher/compressor depending on the direction of chirp needed [120,121]. In order to generate anomalous dispersion, a Treacy design is used as seen in Figure 45. Two gratings are aligned parallel to each other and the separation distance, diffracted angle, and grating period determine the amount of anomalous dispersion, where the amount of GVD is given by [99]

$$\beta_2 = \frac{m^2 \lambda^3 b}{2\pi c^2 d^2 \cos^2(\theta_D)} \qquad (28)$$

In this equation $m$ is the diffraction order, $b$ is the distance the diffracted ray travels or $b = B\sec(\theta_D)$ where B is the center to center separation between gratings, $c$ is the speed of light, $d$ is the period of the diffraction grating, and $\theta_D$ is the diffracted angle. A similar dual diffraction grating system can be designed as a 4f telescope system with lenses to induce normal group velocity dispersion, also known as a Martinez stretcher [120].

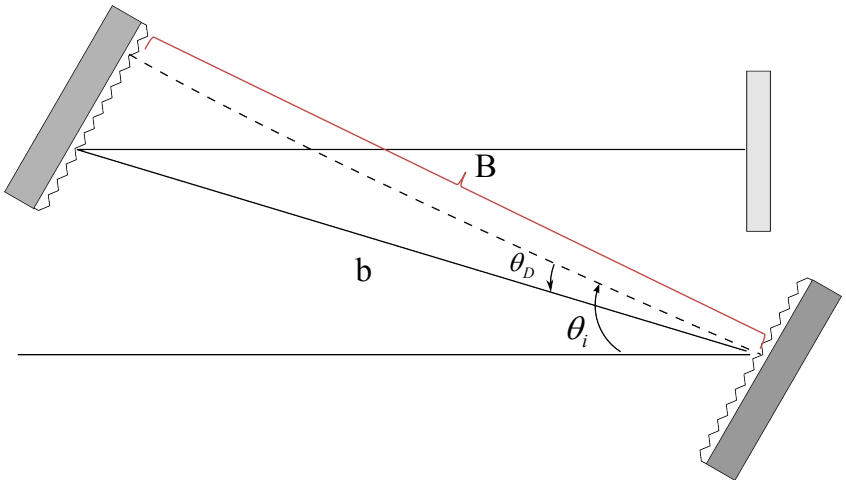


*Figure 45: Example of a Treacy style grating stretcher.*

While diffraction grating based stretchers and compressors can be used for large stretching ratios there are many limitations if a compact system is needed. These limitations originate because the grating period, angle, and distance between gratings are the parameters that determine the dispersion. Without optimizing these values grating based stretcher and compressors can become extremely large.

A more compact method for producing large chirp rates is to use chirped Bragg gratings (CBG). CBGs are possible in both fiber structures and PTR glass [72,122,123]. A chirped Bragg grating has an aperiodic structure so that different frequency components are reflected at different points in the structure. Due to oscillatory behavior by producing a purely aperiodic structure the CBG must be apodized to reduce side lobes and flatten the dispersion behavior [124]. The major limitation of the CBG is that the reflection bandwidth is finite, so the bandwidth of the pulse must be narrower than the CBGs bandwidth. The advantage of using a CBG is that the chirped structure has a temporal reciprocity. This temporal reciprocity means that each side of the grating has opposite but equal chirp rates on all dispersive orders, therefore

they can cancel each other. The use of a CBG in PTR glass allows for stretching and compressing pulses with a single element, and with high peak powers because the beam can be expanded to reduce nonlinearities in compression [123]. To determine the GVD of a CBG Ouellette [122] derives a formula to calculate the term $\beta_2$

$$\beta_2 = \frac{n}{\pi}\frac{\lambda_0^2}{\Delta\lambda}\frac{L_g}{c^2} \qquad (29)$$

where the chirp rate is given by $\frac{L_g}{\Delta\lambda}$ and $\Delta\lambda$ is the bandwidth of the grating.

### *4.3.4 Prospects of 2 μm and Thulium*

One of the central themes of this dissertation is to show that using Tm:fiber offers a path to generate high energy fs laser sources. To date, there have been very few demonstrations of CPA using Tm doped fiber. The first demonstration occurred in 2005 where a Raman soliton was shifted from an Er:Yb fs oscillator to the 2 μm wave band. Pulse were then stretched in a short section of normal dispersion fiber and amplified in a highly dispersive amplifier, where the pulses were compressed during amplification. Results from the system yielded a source with 230 kW peak power, 31 nJ and ~ 108 fs pulses [113]. However, the spectral properties of this system were not described. More recently, groups have been taking advantage of fiber stretching and compression in bulk gratings. Long stretching-ratio chirped pulse amplification in thulium fiber has been demonstrated by two research groups to date, one reaching 151 nJ corresponding to ~ 600 kW peak power and the other being a low repetition rate system capable of 650 nJ with ~ 800 kW peak power [118,119]. In these cases, long lengths of passive fiber have been utilized to stretch pulse durations to 10's ps using both normal and anomalous dispersion fiber [118,119]

and compressed using grating-based compressors in Treacy or Martinez geometries. The primary limitation of the Treacy compressor is positive third order dispersion (TOD), which adds to the positive TOD added by the active and passive fibers in the system and limits the minimum compressed pulse duration. Fully compressed pulse energies are approaching, but have not yet reached, μJ-level with MW peak power in Tm:fiber.

The progress in CPA of Tm is well behind that of Yb, but the dopant and the wavelength offer some possible advantages over CPA at 1 μm. The bandwidth of thulium, as described in Section 1.2, allows for extremely broad bandwidth amplification capable of supporting CPA sub-100 fs pulses after compression. Another major advantage of Tm over Yb fiber systems lies in the central wavelength. This follows directly from the proportionately of the nonlinear parameter, $\gamma \propto (\lambda A_{eff})^{-1}$. By scaling to 2 μm there is a possibility to generate up to 10 times the energy in a pulse compared to 1 μm before SPM accumulation degrades the pulse quality. The V-parameter also is inversely proportional to wavelength, therefore large mode-field area fibers can be utilized while maintaining fundamental mode operation. With combination of the large mode-field possible and the inverse proportionality to wavelength, there are clear advantages.

# CHAPTER 5: FEMTOSECOND PULSE GENERATION AND AMPLIFICATION

## 5.1 Broadband CPA System

### *5.1.1 SWCNT Mode-Locked Oscillator*

We constructed a Tm:fiber oscillator operating as a bidirectional ring cavity, core pumped by a 1550 nm Er:Yb fiber laser via a WDM spliced to the single mode active fiber. The PM Tm doped fiber in the cavity is ~1.1 m long with 10/130 core/clad diameters (Figure 46). The opposite end of the Tm:fiber is spliced to a section of SMF 28 that contained a section adiabatically tapered to a diameter of ~6 μm and coated with a SWCNT-polymer composite, such that the SWCNTs acted as a saturable absorber on the evanescent light propagating through the fiber taper [104]. Operation of the SWCNT SA was described in Section 4.2.2.1. The ring was completed by splicing another section of fiber containing a 90/10 tap coupler into the ring, where the 10% tap served as the output coupler and the 90% port was spliced to complete the ring cavity.

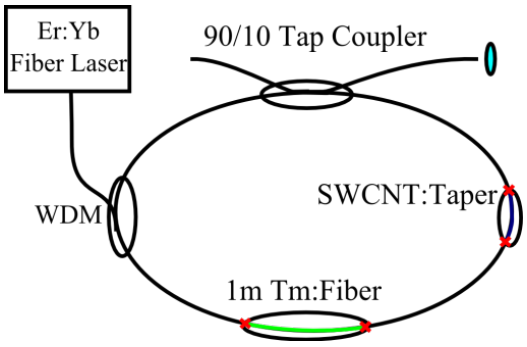


*Figure 46: System schematic of the ultra-fast oscillator [125]*

Stable mode-locking was achieved at a repetition rate of 70 MHz, producing soliton pulses with ~40 pJ energy and ~8 nm spectral bandwidth (Figure 47). Autocorrelation

measurements confirmed bandwidth limited pulses of ~500 fs duration. The average output power was 3 mW. Due to the low energy, the pulses needed to be amplified; however, the spectral modulations due to Kelly side bands needed to be smoothed for optimal amplification. Amplification with Kelly side bands will cause energy to be amplified in the sharp peaks of the side bands and degrade pulse quality.

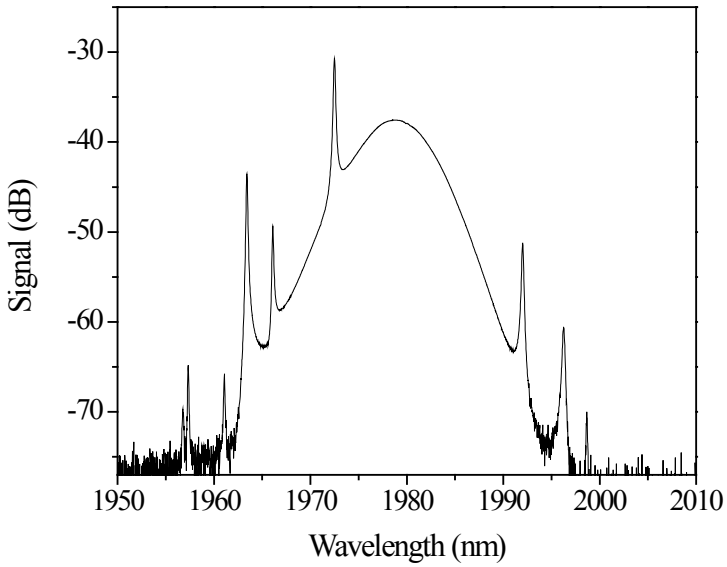


*Figure 47: Spectral output from the USP oscillator. Modulations on the spectrum are due to Kelly sidebands typical of soliton mode-locking [125].*

### *5.1.2 Raman-Soliton Self Frequency Shift Amplifier*

A tunable Raman amplifier was used to spectrally smooth and amplify the oscillator pulses similar to [126]. The unpolarized output of the USP oscillator was transmitted through a series of waveplates and an optical isolator providing linear polarization. The oscillator output was launched into a single mode 10/130 Tm:fiber that was pumped by 793 nm in the co-propagating direction (Figure 48). Pumping the active fiber aided in the formation of a Raman

soliton and the Raman induced frequency shift (Section 4.3.2). By changing the diode pump power, the center wavelength of the Raman pulse could be tuned from ~1970 nm – 2200 nm. The output of this amplifier stage was reflected from a short wave pass filter to spectrally filter the input seed pulse and provide a clean spectrum for subsequent stages (Figure 50).

In addition to spectrally cleaning the pulses, the signal was amplified from 40 pJ to 7-9 nJ after the spectral filter, depending on wavelength. The process of generating the Raman pulse broadened the spectral width of the pulse from ~ 8 nm to 29 nm corresponding to a pulse duration decrease from ~ 500 fs to ~150 fs (Figure 49).

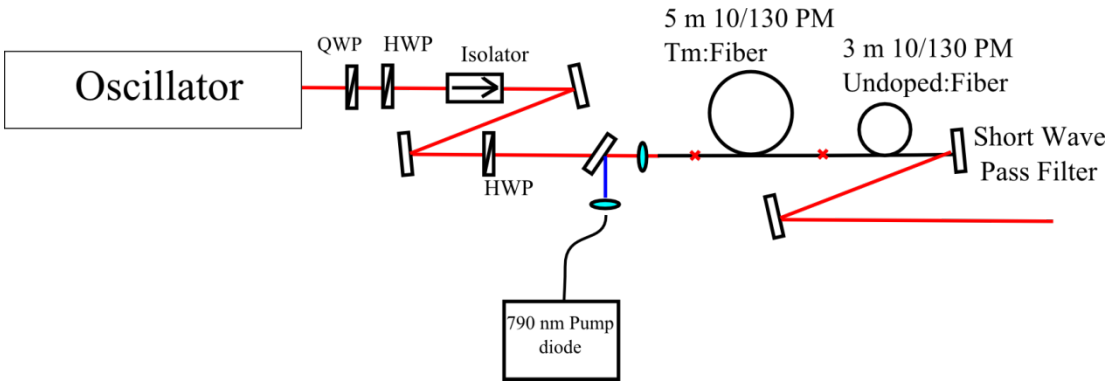


*Figure 48: Schematic of the Raman SSFS amplifier system containing the short wave pass filter [125].*

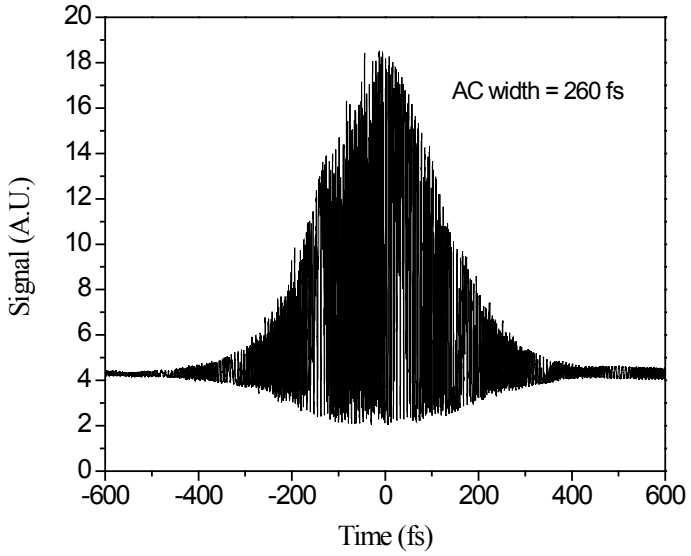


*Figure 49: Interferometric autocorrelation of pulse from Raman SSFS [125].*

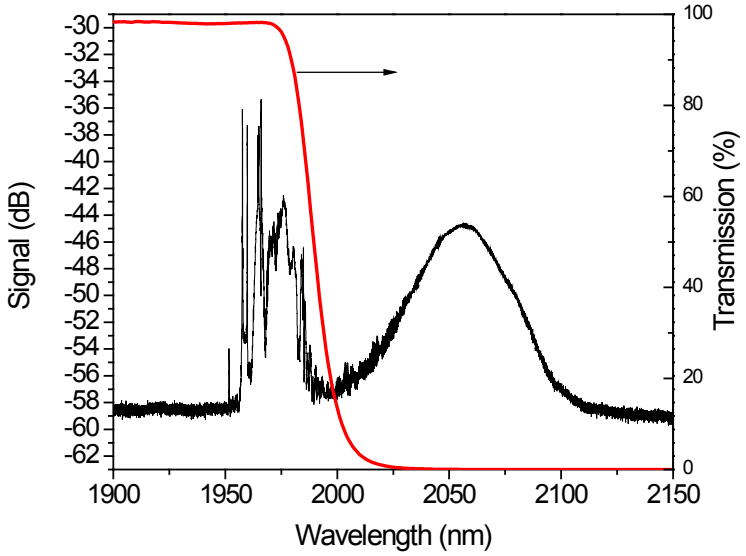


*Figure 50: Spectral output from the Raman SSFS amplifier. The short wave pass filter transmission is overlayed atop the spectrum to show that the slope is sub-optimal for the position of the center of the oscillator spectrum [125].*

### *5.1.3 Pulse Stretching Fiber*

Prior to the final stage of amplification, a 20 m long ultra-high NA (UHNA) silica fiber, with positive GVD was used to temporally stretch the pulses. Despite the anomalous material dispersion of silica in the 2 μm wavelength regime, the fiber parameters are used to modify the waveguide dispersion and shift the overall fiber GVD to positive values. Pulses transmitted through the fiber spectrally broadened from 29 nm to 60 nm due to SPM pulse broadening, as shown in Figure 51. We estimate the pulse duration stretched from ~150 fs to greater than >40 ps at 2020 nm center wavelength.

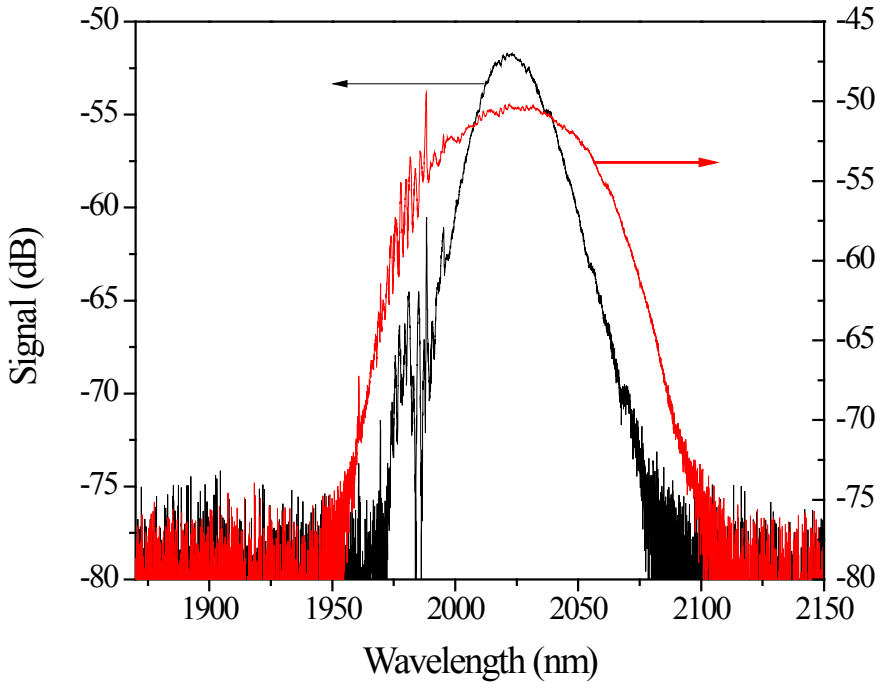


*Figure 51: Spectral output of the filtered Raman pulse and the stretched pulse in the UHNA fiber. The broadened pulse represents the stretched pulse [127].*

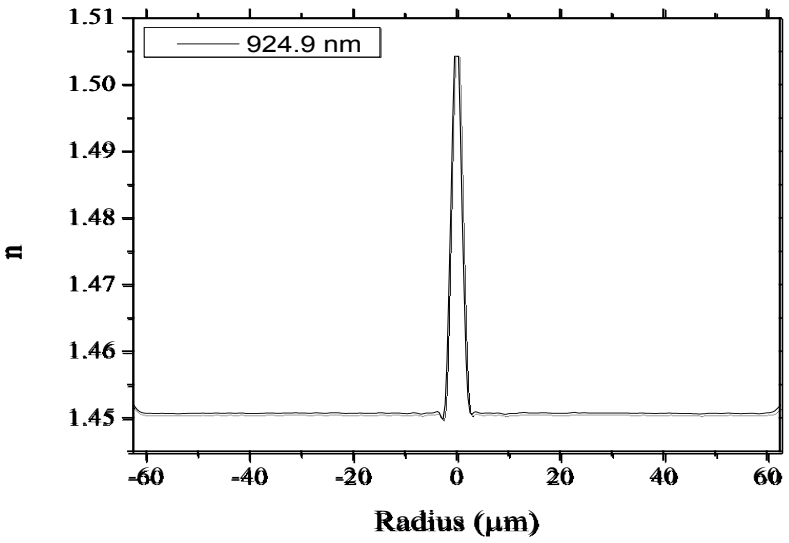


*Figure 52: Measured refractive index profile of the UHNA fiber at 924.9 nm. The measurement was recorded with an IFA-100 multi-wavelength optical fiber analyzer (Interfiber Analysis)*

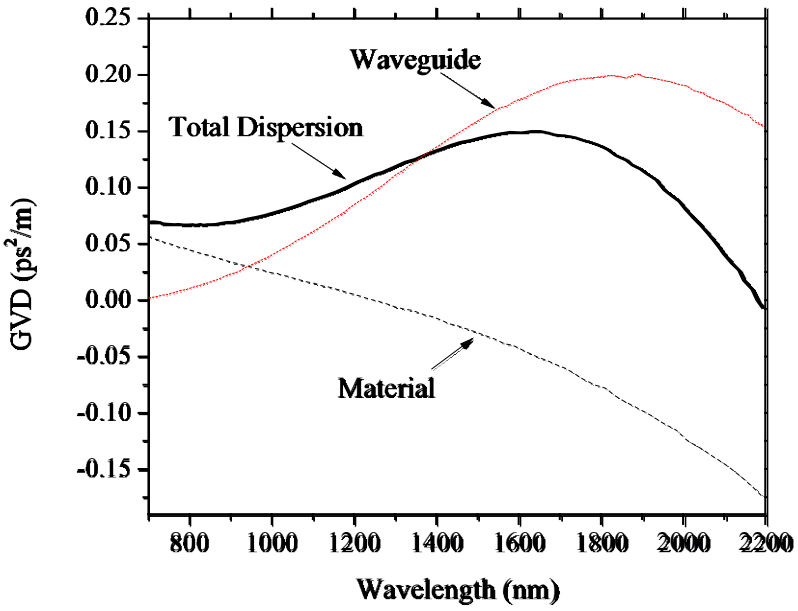


*Figure 53: Model of GVD of the UHNA7 fiber using refractive index values provided by Nufern, Inc. at 590 nm*

The GVD of the UHNA fiber has both been modeled and measured experimentally; however these values do not currently match. A measurement of the spectral interference of the UHNA fiber provided a value of 225±25 ps/km while computer models show more half that value Figure 53. One of the major limitations of the computational model is the lack of knowledge of the exact refractive index and the refractive index variation from the core and clad. We have measured values of the refractive index at 590 nm and are assuming both fibers follow the Sellmeier equation for fused silica.

### *5.1.4 Power Amplifier*

The final amplifier consisted of ~2.7 m of 25/400 non-PM Tm doped fiber with short sections of undoped fiber spliced to the doped fiber to aid in thermal management (Figure 54). The relatively short fiber length resulted in an amplified spontaneous emission (ASE) peak centered near 1970 nm. Amplification was investigated at 2020 and 2050 nm by tuning the center wavelength of the Raman amplifier.

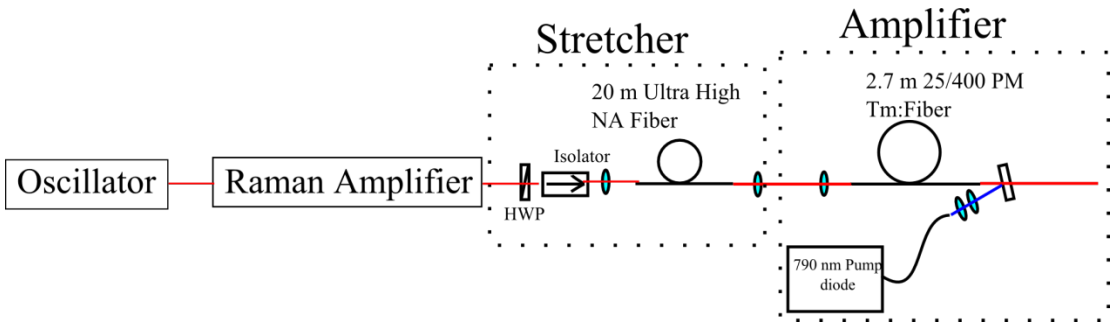


*Figure 54: Schematic of pulse stretcher and amplifier*

For amplification at 2050 nm, the final amplifier was seeded with 80 mW of average power and amplified to 8.4 W of average power or 120 nJ with a slope efficiency of 32 %. Some amplification of the portion of the initial pulse that leaked through the spectral filter was

observed as slight modulations on the short wavelength side. The center wavelength also shifts towards the ASE center of the Tm:fiber and the spectral width narrows. Although the spectrum of the pulses shifted, >40 nm (FWHM) was amplified (Figure 55). The strong spectral modulations are due to a few transverse modes propagating in the LMA fiber and subsequent spectral interference.

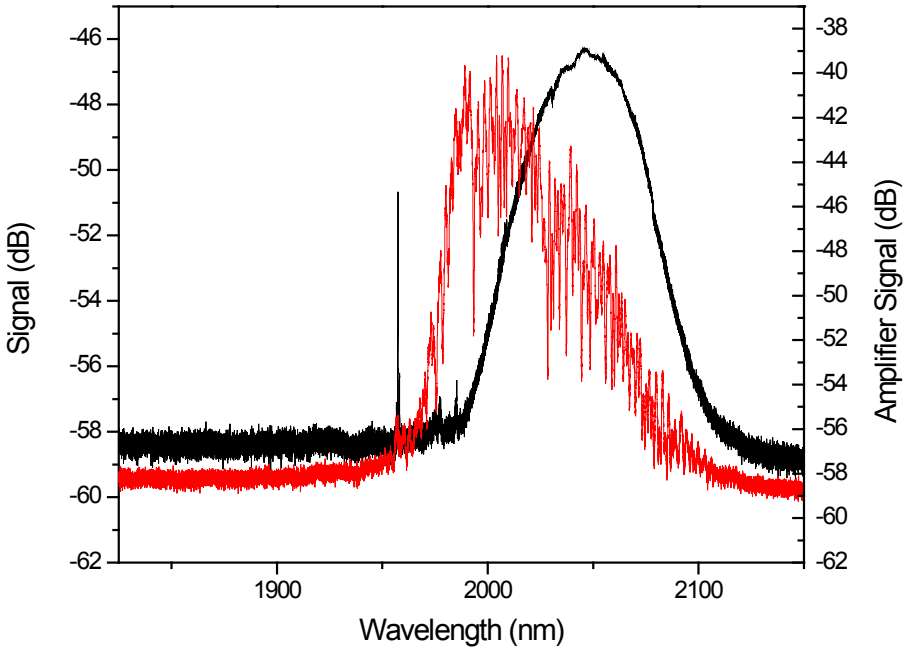


*Figure 55: Spectrum of pulses centered at 2050 nm prior to and after amplification. The modulated spectrum shows the amplified pulses and the spectral shift towards the gain peak of the fiber [128].*

The amplifier performance was improved by seeding closer to the ASE peak of the amplifier. The final amplifier stage was seeded by stretched pulses with an average power of 150 mW centered at 2020 nm, and amplified to powers up to 12.8 W corresponding to 182 nJ of energy. Figure 56 shows the spectral evolution of the amplification process where the ~60 nm of

bandwidth was maintained as the output power increased, although there is a slight shift of center wavelength closer to the ASE peak. Throughout the amplification process ASE increases, but remains >20dB below the peak of the spectrum

### *5.1.5 Higher Order Modes in 25/400*

As mentioned previously, the output of the non-PM 25/400 amplifier fiber shows a large amount of spectral modulation due to higher order modes propagating in the fiber and causing spectral interference due to the differences in the group velocity of different modes. A 2 μm ASE source was coupled into the fiber to excite the $LP_{01,}$ $LP_{11}$, and cladding modes independently.

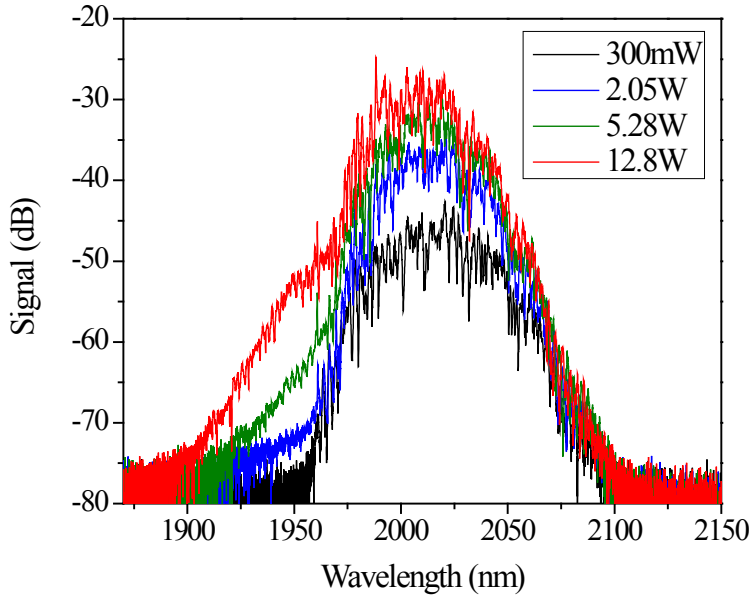


*Figure 56: Spectral evolution of amplified pulses centered at 2020 nm. The spectral center shifts slightly but shows amplification of ~ 60 nm as well as ASE <1950 nm [128].*

In the first test, light from an ASE source was deliberately launched to excite cladding modes, $LP_{11}$, and $LP_{01}$ modes and examine the spectral response after propagation through the fiber. Figure 57 shows the three cases with an image of the fiber facet with the associated spectral response. In the cases where light propagated in the cladding modes and higher-order modes, there were strong high frequency modulation associated with many modes propagating and interfering in the cladding. Launching primarily the $LP_{11}$ shows a reduction in the high frequency modulation and an inference between the fundamental and this mode. Launching purely the fundamental mode results in transmission with no spectral modulation; thus, demonstrating that this fiber is appropriate for amplification at 2μm. To mitigate this effect and reduce free space sections in the laser system mode field adaptors (MFA) have been fabricated to match the mode field diameter of single mode and LMA fibers. By successfully fabricating the MFA, discussed in Section 1.1.2.2, the fundamental mode is launched in the LMA fiber and multi-mode interference is mitigated.

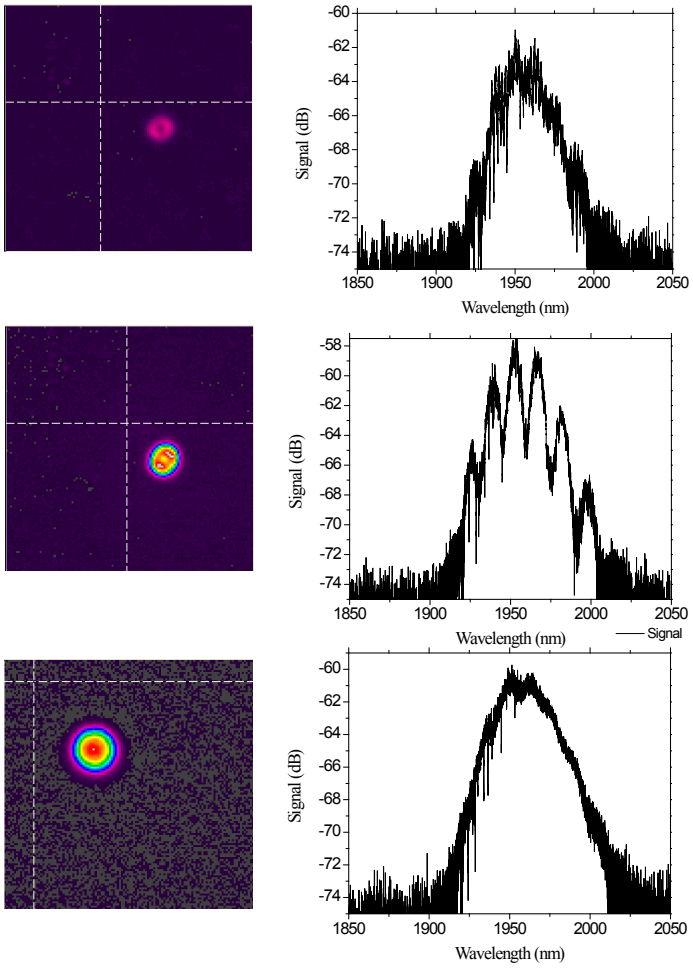


*Figure 57: Spatial beam quality with associated spectrum. From top to bottom the figures shows light launched into the cladding, the LP11 mode propagating, and lowest order mode operation.*

### *5.1.6 Conclusions for the first CPA system*

In this first attempt at CPA pulses were stretched in a fiber with normal dispersion and tight confinement leading to nonlinear broadening of the pulse from 29 nm to 60 nm. These results provide a potential pathway to develop a sub-100 fs CPA system with high peak powers. Using FiberDesk we developed a simplistic model to look at the ability to stretch and broaden pulses in the UHNA fiber then compress to pulse duration shorter than the input. In this model a 150 fs pulse propagates through 2 m of the UHNA fiber with a 4 μm MFD and 0.044 $ps^2$/m of

GVD. This value of GVD will be discussed later in the section on CBG stretching and compressing. Using this simulation, pulses broadened spectrally to 63 nm and were compressible to 98 fs by taking only the GVD into account (Figure 58), since the TOD of the UHNA fiber is not known. Figure 59 shows the evolution of the spectral width (FWHM) and the B-Integral of the pulse. The simulation shows the B-Integral is π when the spectral broadening is 61.5 nm broad, which would correspond to a time-bandwidth limited pulse of 72 fs. Therefore the time bandwidth product of this compressed pulse is 0.455 compared to the theoretical 0.315 for a hyperbolic secant function and 0.85 for a parabolic pulse [129]. The phase induced by SPM hinders the pulse compression in this simulation.

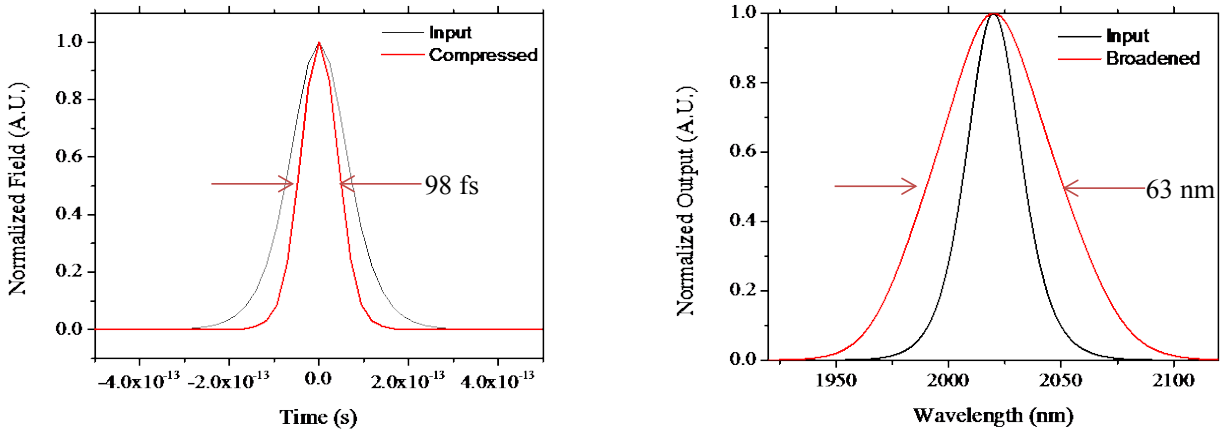


*Figure 58: FiberDesk model of a pulse broadening in a UHNA fiber and recompression of the pulse in a diffraction grating compressor.*

Amplification in the LMA fiber yielded 32 % slope efficiency. Presently in the other published Tm CPA system the slope efficiency has been <41% [118], therefore the often quoted advantages of cross-relaxation have not been realized. The final advancement that needs to be

accomplished when developing the amplifier is to maintain fundamental mode quality. In order to do this mode-field adaptors will be used to couple light into the LMA amplifier fibers.

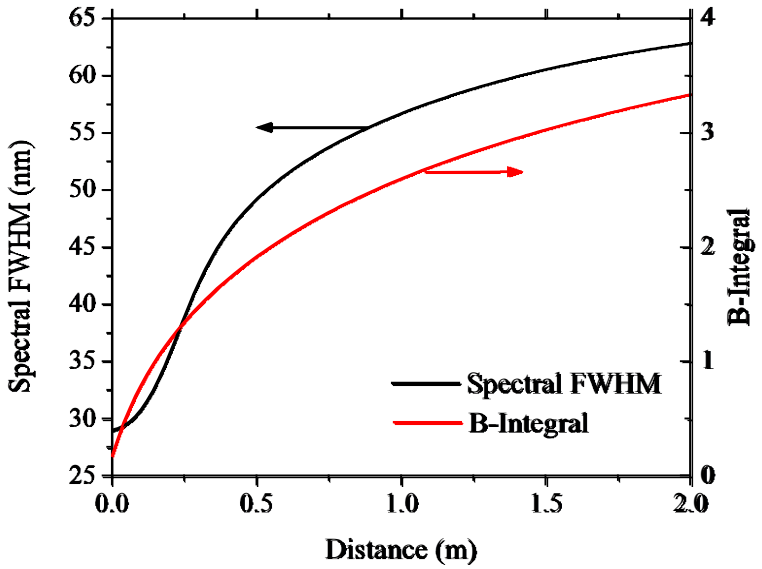


*Figure 59: Spectral Broadening and B-integral as functions of length in the propagation of 150 fs pulse in UHNA fiber.*

## 5.2 CPA System with CBG Stretching and Compression

### *5.2.1 System Design*

5.2.1.1 Mode-Locked Oscillator

In this system pulses were generated from a slightly different amplifier than discussed previously. Femtosecond pulses were generated in an all-fiber ring cavity pumped by an Er:Yb fiber laser. The oscillator, shown in Figure 60, contains sections of SMF28E passive fiber and a ~1-m long section of non-PM 10/130 Tm fiber (Nufern, Inc) doped fiber. The oscillator was passively mode-locked using a single-walled carbon nanotube saturable absorber fiber taper [104] (KPhotonics, LLC) and polarization controllers in the system. Mode-locking is

achieved by turning pump power from the Er:Yb above laser threshold and by rotating the polarization controllers to initiate mode-locking. If the system does not contain the polarization controllers it is not possible to mode-lock, therefore we believe this system is mode-locked using nonlinear polarization evolution that is partially induced by the SWCNT SA. Time-bandwidth limited pulses were output from the 90/10 tap coupler with pulse durations of ~800 fs and 5 nm (FWHM) spectral bandwidth centered at 1975 nm. Due to the anomalous dispersion of the fibers in the cavity, the oscillator operated in the soliton regime with pulse energy limited to 40 pJ at 60 MHz. The mode-locked spectrum exhibits Kelly-side bands typically associated with soliton pulses; therefore a pumped SSFS amplifier was used, shown in Figure 61

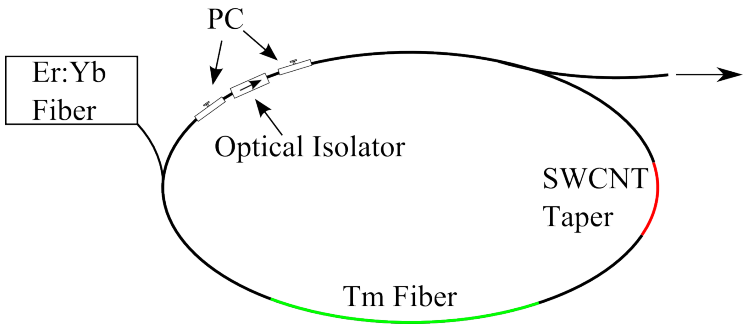


*Figure 60: Schematic of a mode-locked ring laser containing polarization controllers (PC) and SWCNT [130]*

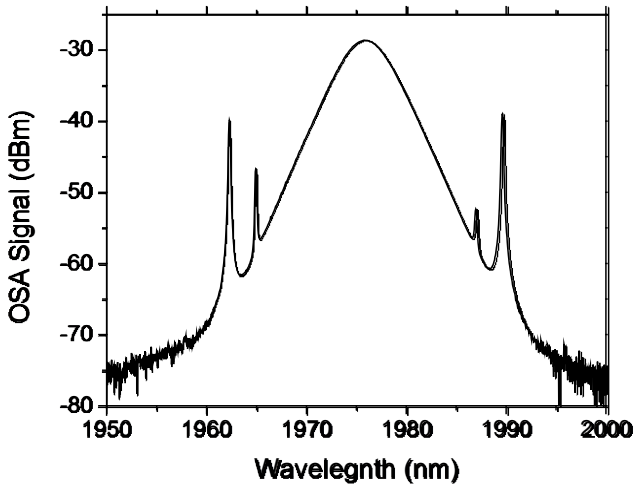


*Figure 61: Output spectrum from the mode-locked oscillator from an OSA. The spectrum exhibits a 5 nm bandwidth and Kelly side bands [130].*

5.2.1.2 Soliton-Self Frequency Shift Amplifier

Output from the mode-locked oscillator propagated through a free space isolator and half-wave plate before being coupled into the single-mode PM 10/130 fiber input port of a 2+1 x 1 taper fiber bundle (TFB) (ITF Labs/3S Photonics), as shown in Figure 3. The TFB was pumped with a 35 W, 793 nm diode (DILAS Diodenlaser GmbH) with 100 μm diameter delivery fiber, and spliced to a ~5 m long section of PM 10/130 Tm doped fiber. This amplifier utilized a Raman-soliton self-frequency shift, where the output signal was tunable from 1980 to 2100 nm depending on the diode pump power. The output of this system produced an amplified pulse with a clean spectrum, red-shifted in wavelength from the oscillator center wavelength of 1975 nm. The total output power was split between the residual oscillator pulse and the frequency shifted pulse, with ~60% of power in the shifted pulse. Figure 2 shows both the spectral and temporal characteristics of the amplified pulse corresponding to 3 nJ energy in the shifted soliton. The

pulse spectral width was 30 nm (FHWM) and the autocorrelation confirms a transform-limited pulse width of 150 fs (FWHM).

5.2.1.3 CBG Stretching and Single-Mode Amplifier

In order to amplify further, the pulses were temporally stretched in a CBG purchased from Optigrate Corp. The CBG reflectivity has 52 nm bandwidth centered at 2020.5 nm, with both surfaces anti-reflection coated for 1900-2200 nm. The reflectivity averages 82% across the full reflection bandwidth, and has a calculated group velocity dispersion of 12.3 $ps^2$ [122]. At this time, we are not able to directly measure the stretched pulse directly but we estimate it to be ~160 ps.

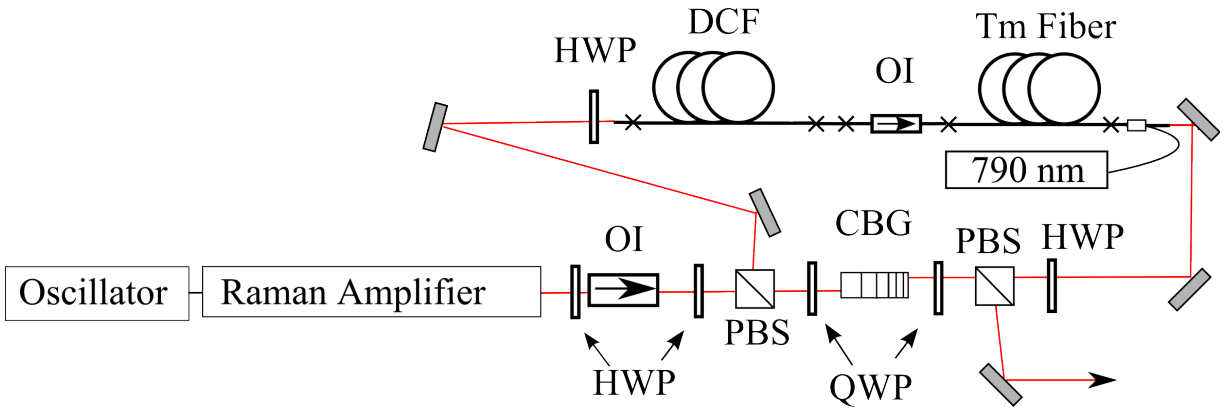


*Figure 62: Schematic showing the setup for the CBG based CPA system [130].*

The schematic for the CPA stage of this laser system is shown in Figure 62. The Raman-soliton was free space coupled to the amplifier stage after the pulse was stretched using the CBG. Using a quarter-wave plate (QWP), upon reflection from the CBG the polarization orientation was rotated 90º so that the stretched signal was output through the side facet of a polarizing beam splitter (PBS). The residual signal from the oscillator pulse centered at 1975 nm was not reflected by the CBG and was therefore not amplified.

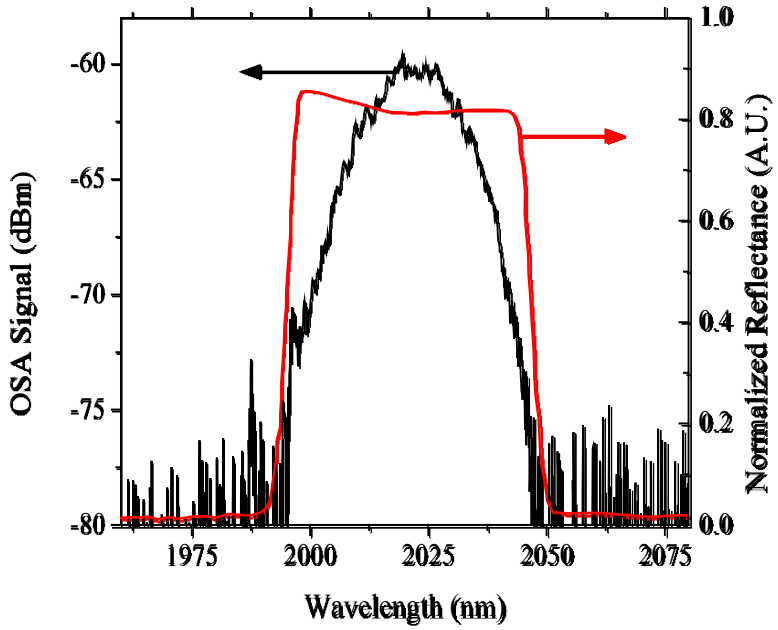


*Figure 63: Pulse spectrum following the CBG. The red curve shows the reflectance of the CBG [130].*

In order the compress the pulse to the minimum duration, a section of normal dispersion fiber was inserted to compensate the anomalous dispersion of the fiber in the amplifier; without the UHNA the minimum compressed pulse duration was 4 ps. The UHNA fiber was the same fiber as discussed in Section 5.1.3. Due to the small mode-field diameter of the UHNA, a mode field adaptor (MFA) was fabricated to couple the UHNA to SM2000, a non-PM single-mode fiber with an 11/125 μm geometry, to maximize seed coupling into the amplifier. A ~9 m section of DCF, bookended by MFAs was inserted prior to the amplifier, introducing ~1 dB loss. The SM2000 fiber was spliced to the undoped fiber pigtail (PM 10/130) of a polarization dependent fiber-coupled optical isolator (Shinkoshsa Co.) to prevent any feedback from the amplifier and insure linear polarization of light prior to amplification. The isolator was spliced to a 4 m section of Tm-doped PM 10/130 fiber that was wrapped around a water-cooled mandrel for thermal

management during amplification. Counter-propagating pump light was coupled into the amplifier using a 2+1:1 TFB. A final section of undoped PM 10/130 was spliced to the output single port of the TFB and cutback to fine balance the dispersion of the DCF and anomalous fiber in the cavity. The pulse was compressed in the CBG using the opposite facet from that for pulse stretching via polarization dependent transmission (input) and reflection (output) from a PBS.

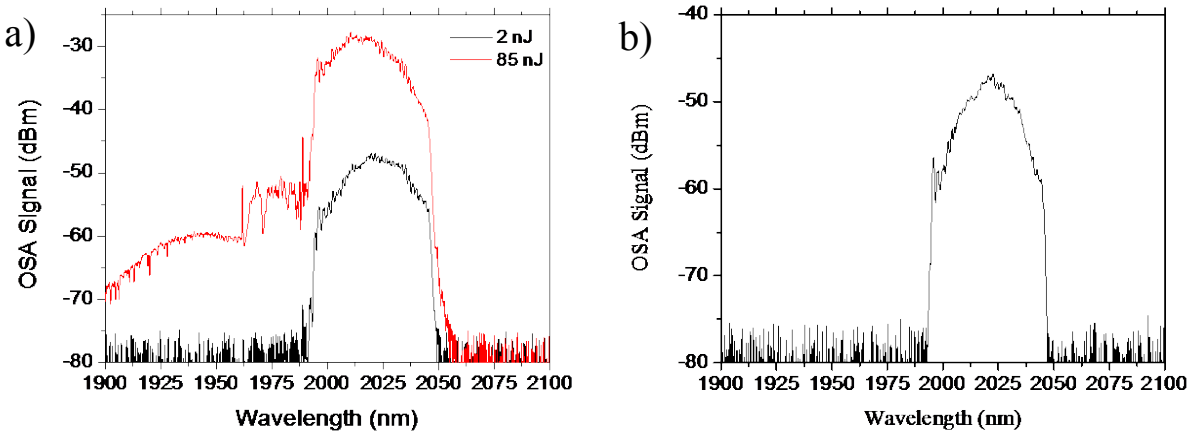


*Figure 64: a) The spectral output of the single-mode amplifier at both low and high energy prior compression with the CBG. b) The spectral output of the compressed pulses [130]*

### *5.2.2 Chirped Pulse Amplification Results*

After stretching in the CBG, the power was ~120 mW. Due to coupling losses from the CBG into the DCF and losses from the DCF and fiber isolator, we estimate the average power injected into the Tm:fiber was ~50 mW. This was amplified to a maximum average power of 5.8 W with 10% power in ASE, and was re-compressed to as short as 400 fs pulse duration. As shown in , there was a slight increase in pulse duration from 400 to 550 fs during amplification to 85 nJ, which we attribute to further truncation of the optical spectrum during compression. As

shown in Figure 7, there was a slight roll-off in the slope efficiency suggesting that ~20 dB is the maximum gain possible for this single-stage single-mode fiber amplifier. The OSA traces in Figure 64 a) shows spectra after amplification. There is no evidence of spectral modulation due to self-phase modulation and only a slight blue-shift of the center wavelength towards the ASE peak near 1950 nm. Figure 64b) shows the final spectrum of the compressed beam at 85 nJ. The output appears narrower than the corresponding case in Figure 8a) because the beam is slightly spatially chirped; therefore collection with the single mode fiber for the OSA does not capture the full spectrum.

One of the major limitations of fiber CPA systems is the maximum amount of nonlinear phase that can be accumulated before proper pulse compression is impossible, as quantified by the B-integral. We have modeled, using FiberDesk, the pulse evolution in the single-stage amplifier through a split-step Fourier transform and calculated the B-integral to be ~1.3 radians. Assuming a B-Integral limit of $\pi$ radians, it should be possible to reach ~0.9 μJ in a single-mode amplifier with this stretch pulse duration, which would be acceptable for recompression without signification nonlinear phase degradation.

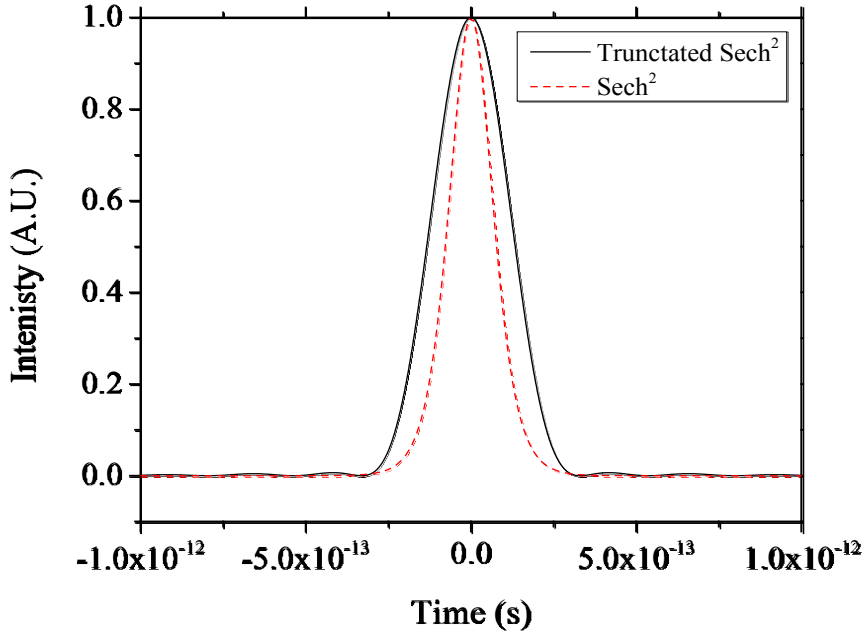


*Figure 65: Fourier transform of a hyperbolic secant function and a truncated hyperbolic secant. This graph simulates the transform limited pulses expect with compression using a CBG [130].*

The CBG is a simple and compact device providing temporal reciprocity when stretching and recompressing. We use normal dispersion fiber to compensate the GVD of the amplifier fiber has; however, residual TOD and higher order dispersion are not cancelled. Additionally, the bandwidth of the Raman soliton and the reflectivity bandwidth of the CBG limit the minimum compressible pulse duration. The CBG has a rectangular shaped spectrum spanning 52 nm and the Raman soliton has a FWHM of 30 nm with a corresponding full width bandwidth >52 nm. Thus, portions of the spectral wings of the input seed are truncated and the compressed pulse cannot be recompressed to the input pulse duration. Figure 65 shows a computer simulation of the Fourier transform of a truncated hyperbolic secant and the initial hyperbolic secant pulse. The transform limited pulse duration (FWHM) increases from 150 fs to 272 fs between the hyperbolic secant and the truncated spectrum. Using the ideal case of a hyperbolic

secant pulse shape without truncated spectrum the time bandwidth product of low energy pulses and 400 fs pulse duration is 0.704 and 0.98 at higher energies. The pulses at low energy are double the transform limit while higher energy pulses are about triple the transform limit of a hyperbolic secant. Taking into account the truncated spectrum, at high energy the pulse duration is double the time-bandwidth limit.

### *5.2.3 System Model*

Using FiberDesk, the CBG based system was modeled to compare the experimental results for both a truncated pulse and a non-truncated pulse to gain insight on the behavior of the CPA system. Input pulses matched the Raman-soliton in duration and energy but ignored the residual dispersive wave, therefore pulses with 150 fs pulse duration, 3 nJ energy were seeded into the model. In one case pulses were spectrally filtered with the envelope seen in Figure 66 and in another case the pulse were not spectrally filtered. The dispersion of the CBG was calculated as 12.3 $ps^2$ from the parameters supplied by Optigrate and pulse were stretched with a positive values of $\beta_2$. The rest of the system followed as outlined in 5.2.1 with 9 m of UHNA fiber with a dispersion of + 0.04 $ps^2$/m. This value for dispersion is an estimate for the value because we do not have an accurate measurement of the dispersion. By assuming the 10/130 fiber has - 0.085 $ps^2$/m value and the amount of UHNA fiber that compensated the 10/130 was a ratio of 2:1, we estimate the value to be +0.04 $ps^2$/m. The system then contained 0.5 m undoped 10/130, 3.6 m of gain fiber and 0.15 m of undoped 10/130 as the output from the gain fiber. The gain in the system was estimated as uniform across the spectrum. We examined when pulses were amplified to 20 nJ and 85 nJ.

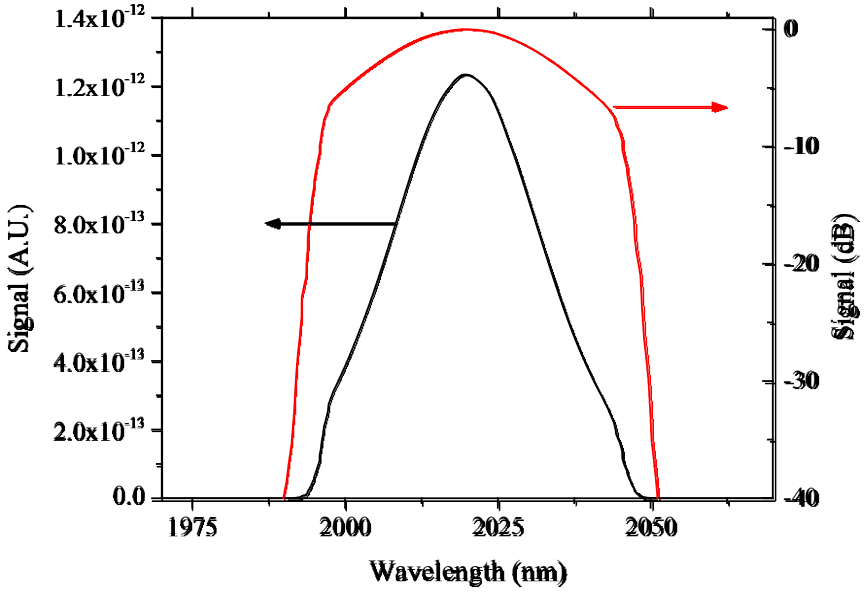


*Figure 66: FiberDesk model of the spectrally filtered hyperbolic secant pulse after propagation through the CBG. This graph has both the linear scale and logarithmic.*

The model, including the CBG as a spectral filter, CBG matches closely to the experimental results. There are minor differences most likely due the estimations of dispersion values, fiber lengths, and not taking into account TOD in the CBG and UHNA fiber. Figure 67 shows truncated pulses as they appear in both linear and dB scale. The last section of 0.15 m of fiber was modified optimize the pulse duration at 20 nJ to 475 fs, matching the pulse duration of system. The gain of the fiber was then increased to amplify pulses to 85 nJ and the final pulse durations were compared. In this case the pulse durations increased to 525 fs.

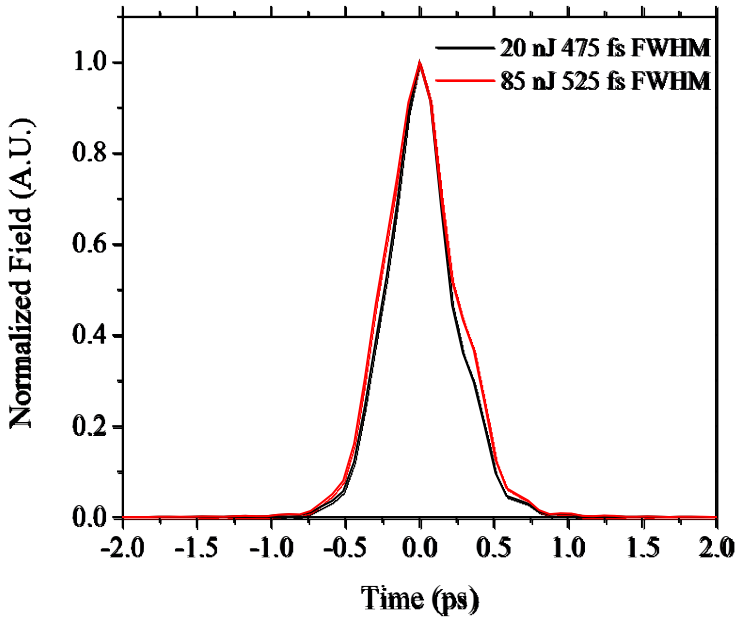


*Figure 67: Simulation of CPA system using parameters for experimental setup.*

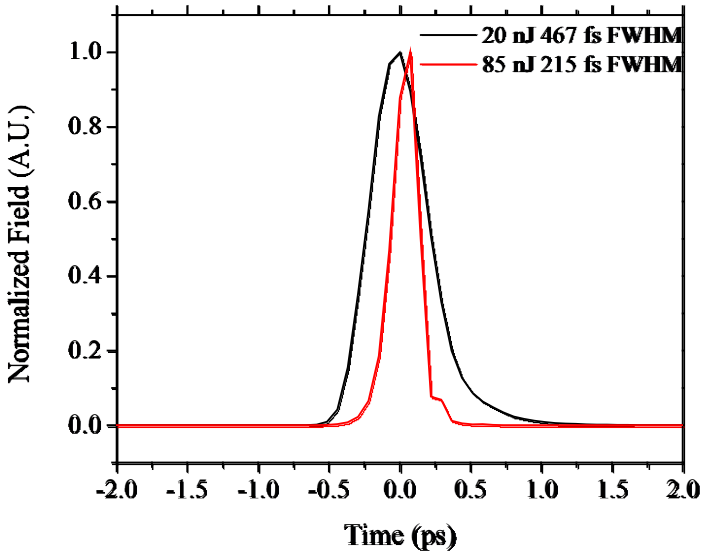


*Figure 68: Final pulse durations from a fiber desk model of hyperbolic secant pulse shape amplified to 20 and 85 nJ.*

The same simulation was completed with a hyperbolic secant pulse shape that was not truncated by a spectral filter to compare the final pulse durations and the amount of SPM accumulation. In this case to compensate dispersion, all fibers were exactly the same except the last fiber that was extended to 0.6 m so that pulses amplified to 20 nJ were 467 fs. Final compressed pulses decreased to 215 fs in this setup with the hyperbolic secant pulse shape. This value is less than the minimum possible with truncated spectrum, which could produce pulses with a minimum duration of 270 fs.

Using these two cases of the actual truncated spectrum vs. a hypothetically hyperbolic secant pulse shape the B-integral was compared as a function of propagation distance. Using this simulation the SPM accumulation of the truncated pulse shape was less than the full pulse shape. The results are shown in Figure 69.

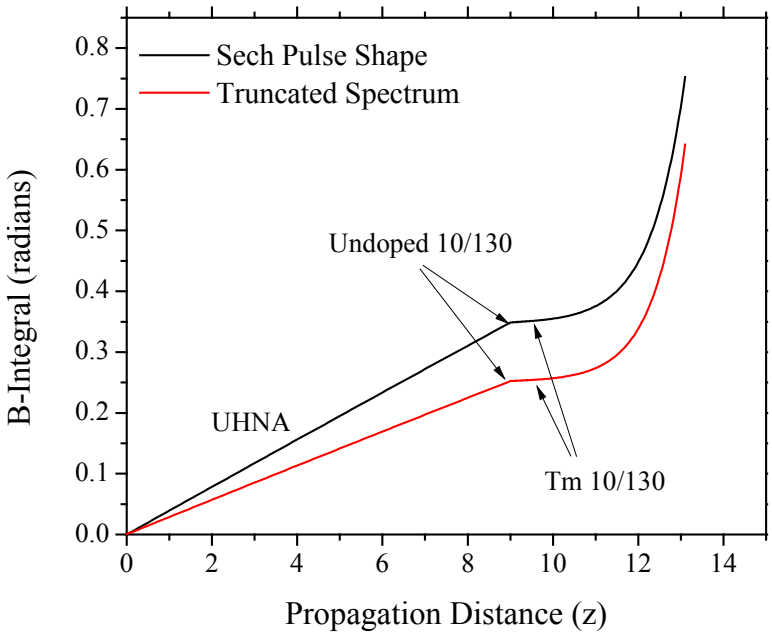


*Figure 69: B-Integral as a function of propagation distance for the CBG based CPA system.*

## 5.3 MW Peak Power CPA

### *5.3.1 System Design*

Amplifying pulses to high peak powers requires the ability to control the pulse repetition rate and dispersion more finely. In this work we use the system described in Section 5.2 as the front end for a higher peak power system. The front end contains the all-fiber oscillator, a Raman SSFS amplifier, CBG for stretching, and a single-mode preamplifier Figure 70. Essentially this is the same system aside from using the CBG as a compression element. Pulses from the preamplifier are propagated through an electro-optic modulator (EOM) capable of picking the pulse repetition rate down from 60 MHz to a maximum of 100 kHz. Due to the addition of EOM there is factor of ~1000x reduction in average power due to the change in duty cycle and loss through the EOM. Therefore, a single-mode Tm preamplifier is used to increase the energy of the pulse. This preamplifier contains ~5m of 10/130 PM Tm:fiber. This active fiber is pumped by two 35 W 790 nm diode lasers through a 2+1:1 pump combiner. The output of this preamplifier is spliced to a polarization sensitive fiber isolator (Shinkohsa Co Ltd.). In order provide a compact system and reduce the issue of free-space coupling into a LMA fiber the isolator is spliced to a MFA that couples light from the 10/130 fiber to 25/400 PM fiber. Using the MFA does not lead to spectral fluctuations due to launching of higher order modes as seen in Figure 56.

The undoped MFA fiber is spliced directly to a 3.5 m section of Tm-doped PM 25/400 PM fiber. This splice was coated with a high index epoxy (n=1.56) to strip cladding modes due to the splice and prevent residual pump light traveling in the cladding from possibly damaging

the isolator during amplification. The Tm:fiber was wrapped around a water cooled mandrel and spliced to a 6+1:1 pump combiner that pumped the counter propagating direction. Only one of the pump fibers of the 6+1:1 was used for pumping with a 70 W 200 μm 790 nm diode laser. On the output there was a section of fiber that was window stripped and coated with a high index epoxy to strip any cladding modes propagating.

Compression of the pulses was completed using a folded Treacy grating compressor with two 2 inch gold-coated copper substrate diffraction gratings. The grating period of these gratings was 600 ln/mm. Gratings provide more flexibility in compression than the CBG as the distance between gratings can be changed. It would be possible to follow a similar system as described previously where normal dispersion fiber was used for compensation of the anomalous dispersion in the amplifiers, however, with the approximate ratio of 2:1 for normal to anomalous fiber ~ 30 m of the UHNA fiber will be needed to compensate the dispersion of the amplifiers. Using this much fiber will increase the amount of nonlinear phase drastically prior to amplification therefore did not seem feasible for producing a high peak-power system.

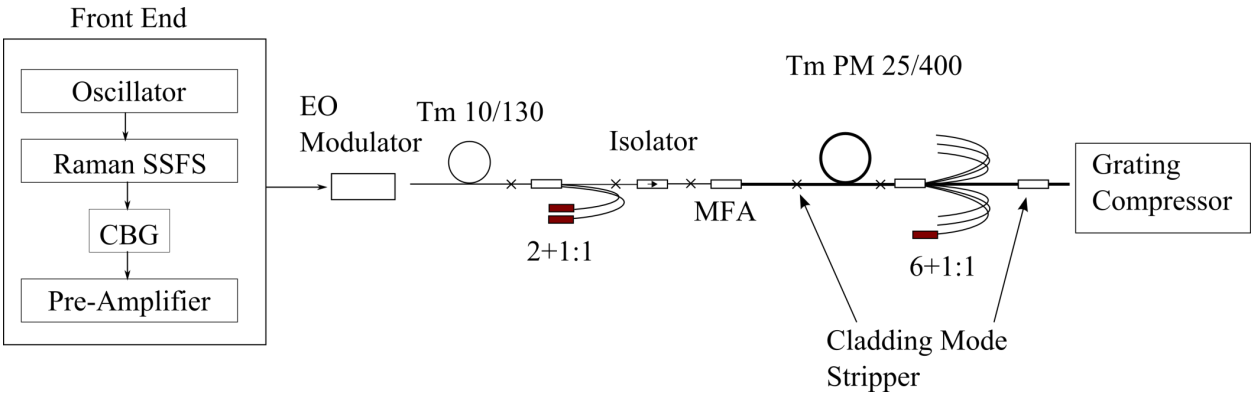


*Figure 70: Schematic for high peak power system.*

### *5.3.2 System Results*

#### *5.3.2.1 Single Mode Amplification*

The nonlinear limitations to amplification in Tm:fiber have not been discussed in literature; therefore, we use a series of single-mode amplifiers, in conjuction with both high and low repetition rate systems explore these limitations. To better determine these limitations a ~7 m section of PM 10/130, both active and passive fiber, was spliced into the system. Figure 70 shows the schematic for the full amplifier system however, in this experiment the LMA final amplifier was exchanged for the 7 m single-mode amplifier. Compared to the CBG based CPA system this system was designed to determine nonlinear limitations associated with the > 12 m additional single-mode fiber and provides the additional amplification necessary for operation at 100 kHz repetition rate system. In order to look at the limitations of single-mode amplification an OSA with both single-mode and multimode collection fibers was used to measure the spectrum and an interferometric autocorrelator measured the pulse duration.

Using the single-mode amplifier, pulses are amplified to energies up to 95 nJ, however examination of pulse degradation for the energy levels does not give conclusive answers. The OSA trace in Figure 71 shows an extremely noisy and spectrally broadened long wavelength edge of the spectrum. The data in the figure iss collected with a 50 μm multimode fiber to ensure that nonlinearities were generated in the amplifier fiber. In this figure there are also small peaks near 2370 nm, which are three times the pump wavelength. These can be removed with a pump filter, and are therefore not associated with the amplifier. Figure 72 show three autocorrelation traces covering a range of 20 ps. As the energy increases, the autocorrelation

baselines become increasingly noisy, but no satellite pulses are observed and the ratio remains 8:1.

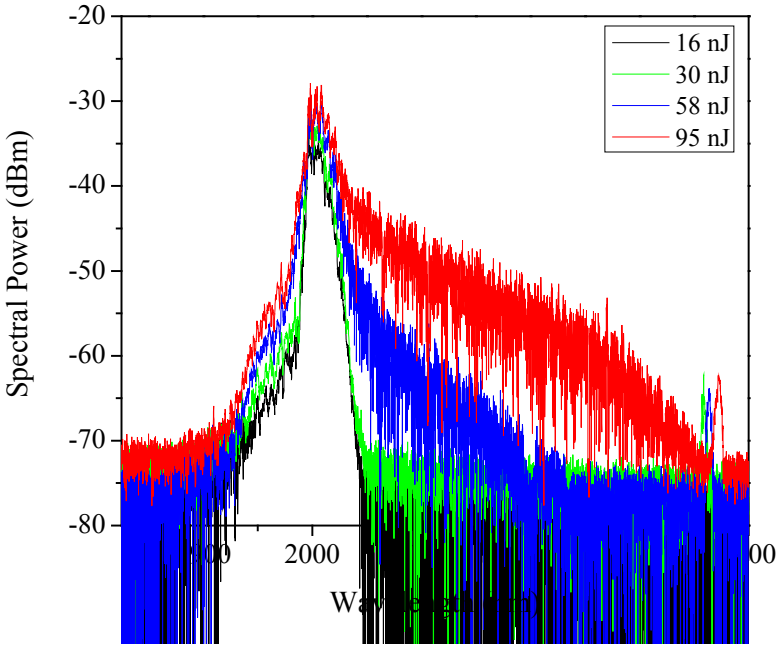


*Figure 71: OSA measurements of spectral broadening in single-mode Tm amplifiers. As energy in the fiber increases the long wavelength tail emerges. Peaks at ~2370 nm are due to measurement of residual pump light.*

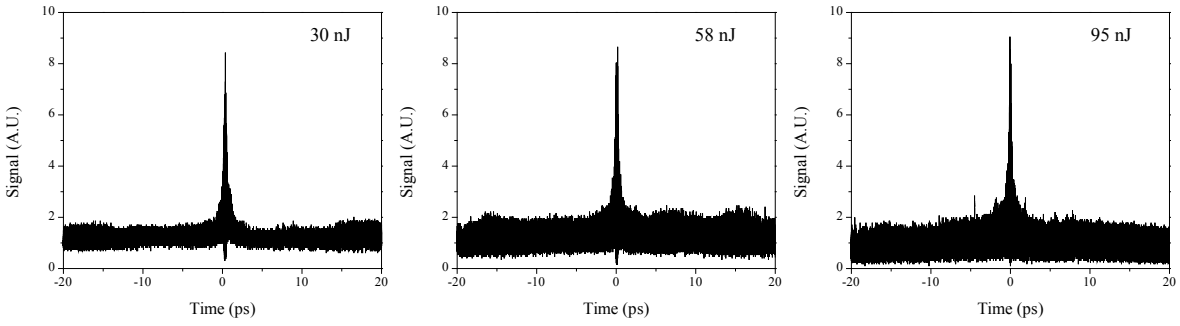


*Figure 72: Interferometric autocorrelation traces of three energy levels after amplification.*

The results from the single-mode amplifier remain inconclusive to the exact limitations for amplifying in Tm:fiber. The results show the emergence of spectral broadening on the long

wavelength side of the dopant suggesting the amplification may be limited due to processes such as modulation instability as opposed to self-phase modulation. The autocorrelations progressively become noisier; however, they do not show a substantial change in the pulse duration. The noise of the autocorrelation also limits the ability to examine the wings of the pulse in case self-phase modulation causes broadening or modification of the wings of the pulse. In order to understand the dynamics of the pulse better pulse techniques such as frequency resolved optical gating (FROG) need to be utilized to fully characterize the output.

#### *5.3.2.2 LMA Amplification*

Increasing the core diameter from 10 μm to 25μm decreases the nonlinear parameter from 0.00102 W/m to 0.000215 W/m therefore higher energy amplification is possible before the nonlinear phase accumulation limits the compression of a pulse. Using the system shown in Figure 70, compressed pulses were amplified to energy values up to 1 μJ with pulse durations ~ 300 fs with 100 kHz repetition rate. At the time of submission for publication, this represents the highest energy and highest peak power output from an ultrashort Tm systemwith sub-picosecond pulse duration.

As stated previously, the pulse picker reduced the repetition rate of the system from 60 MHz to 100 kHz reducing the average power by a factor of 30 dB. The pulse picker also has a contrast ratio of ~ 20 dB, therefore, using this value we estimate that ~15% of the total energy is contained within the pulses at 100 kHz. Thus, the final compressed energy in the 'main' pulses was estimated by measuring the average power, dividing by the repetition rate and imposing conditions for 15% energy in the pulse.

Pulses with a repetition rate of 100 kHz were amplified in single mode pre-amplifier to to 50 nJ level prior to amplification in the LMA fiber. Using the LMA fiber, the energy after compression was amplified up to 1 μJ. Figure 73 shows the compressed energy as a function of launched pump power with no roll off at the higher energies, suggesting further amplification is possible. The compressor efficiency was ~55%; therefore, pulses out of the fiber contained 2.6 μJ energy corresponding to 16 kW of peak power in the amplifier. In order to filter ASE from the output, a knife edge was used as a spectral filter in the Fourier plane of the compressor to remove spectral content with wavelengths shorter than ~1990 nm. Figure 74 a) shows the OSA trace of spectral output from the CPA system in linear and logarithmic scales. The figure shows a highly modulated spectral output that originates in the coupling of light into the LMA fiber. Therefore, the corresponding autocorrelation trace in Figure 74 b) has some modulations near the base of the base of the pulse. These modulations appear because of the multi-mode interference (MMI).

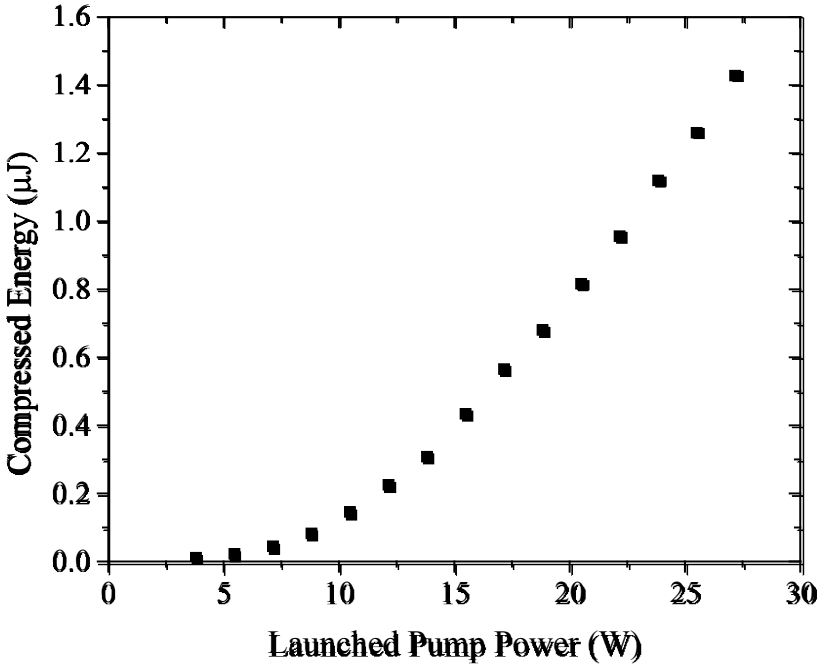


*Figure 73: Compressed Energy as a function of launched pump power for amplification in the LMA fiber*

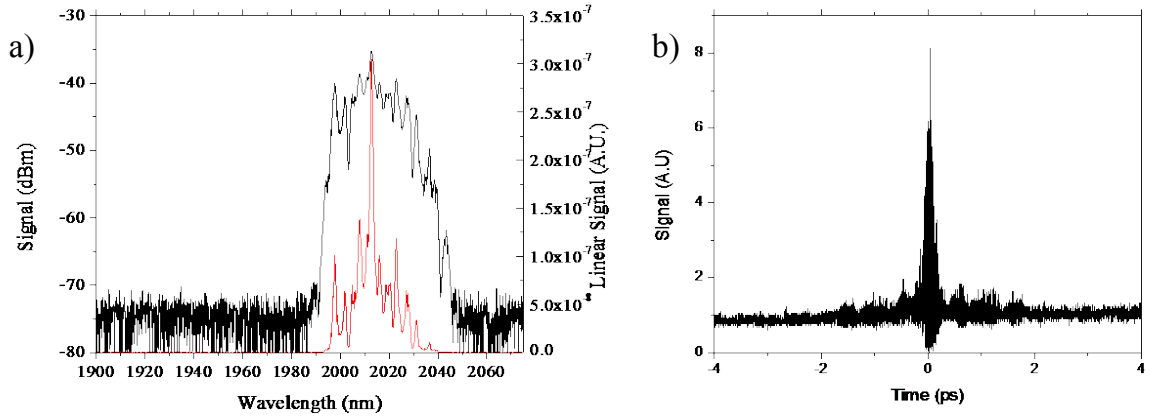


*Figure 74: a) Spectral traces in both linear and logarithmic scale of a spectrally filtered compressed pulse at 1 μJ energy. b) This figure shows the corresponding interferometric autocorrelation trace.*

The spectral modulation shown in Figure 74a) is similar to that of Figure 56, and is the result of higher order mode propagation in the amplifier fiber. In Figure 74 a) the linear scale shows a sharp peak at 2012 nm that has a 2 nm FWHM originated because of the multimode interference in the LMA fiber. Using computation software, OriginLab, the amount of energy was compared between this peak and the rest of the spectrum using an integral function. Using this method we calculate that there was 18% energy in this spectral feature, corresponding to the 2 ps base in the autocorrelation. In Figure 75 three separate autocorrelation traces are shown for different energy levels. The autocorrelation traces show that the pulse contained satellite pulses that extend to 2 ps, however with increasing amplification values the amount of energy in the satellite pulses does not increase. Using Originlab to integrate the amount of energy in the 300 fs main pulse compared to the energy in the satellite pulses we show that greater than 75% was in the main pulse and this is consistent at each energy level. Due to this consistency among energy levels we do not believe that SPM degradation is occurring in the LMA amplification.

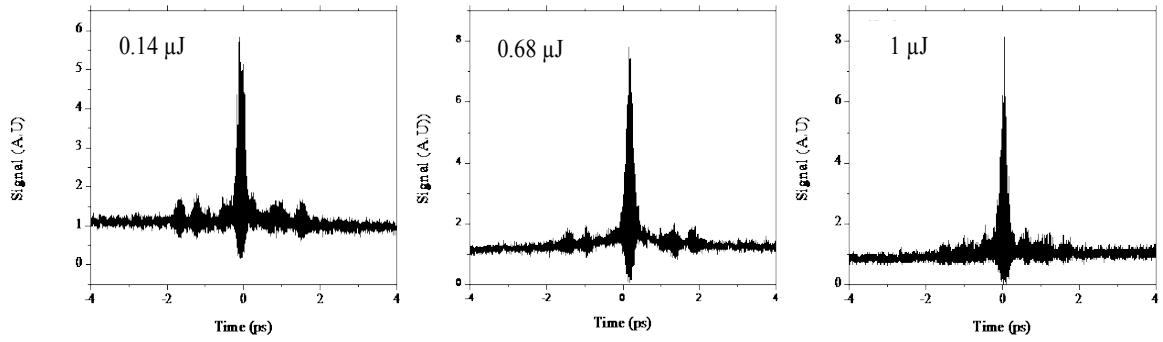


*Figure 75: Autocorrelation traces at different energy levels. The satellite pulses extend to 2 ps but do not increase with energy.*

Figure 76 shows a schematic starting at the fiber optical isolator and compares the spectrum at successive splice point; after the MFA and after the gain fiber. For spectral analysis prior to the optical isolator, Figure 64 shows the output after the first preamplifier. In this system the logarithmic scale shows a relatively smooth output after the optical isolator and mode field adapter, but the splice from the LMA passive fiber to the Tm doped fiber increases the spectral modulation drastically. This splice is also recoated with a UV cure epoxy with a refractive index of 1.5 to function as cladding light stripper. Thus, spectral modulations should not originate from higher order modes in the cladding causing spectral interference but rather the $LP_{11}$ and $LP_{02}$ mode are being excited in the splice coupling. The splice between the Ge-doped fiber and the Tm:Al doped fiber causes the mode mismatch because the difference in thermal diffusion between the two fibers, thus different MFD after splicing [131]. Figure 77 shows the spectral modulation at 0.14 μJ and 0.68 μJ energies to demonstrate that the amplification process is not affecting the spectral quality of the pulse due to SPM in the LMA fiber during amplification.

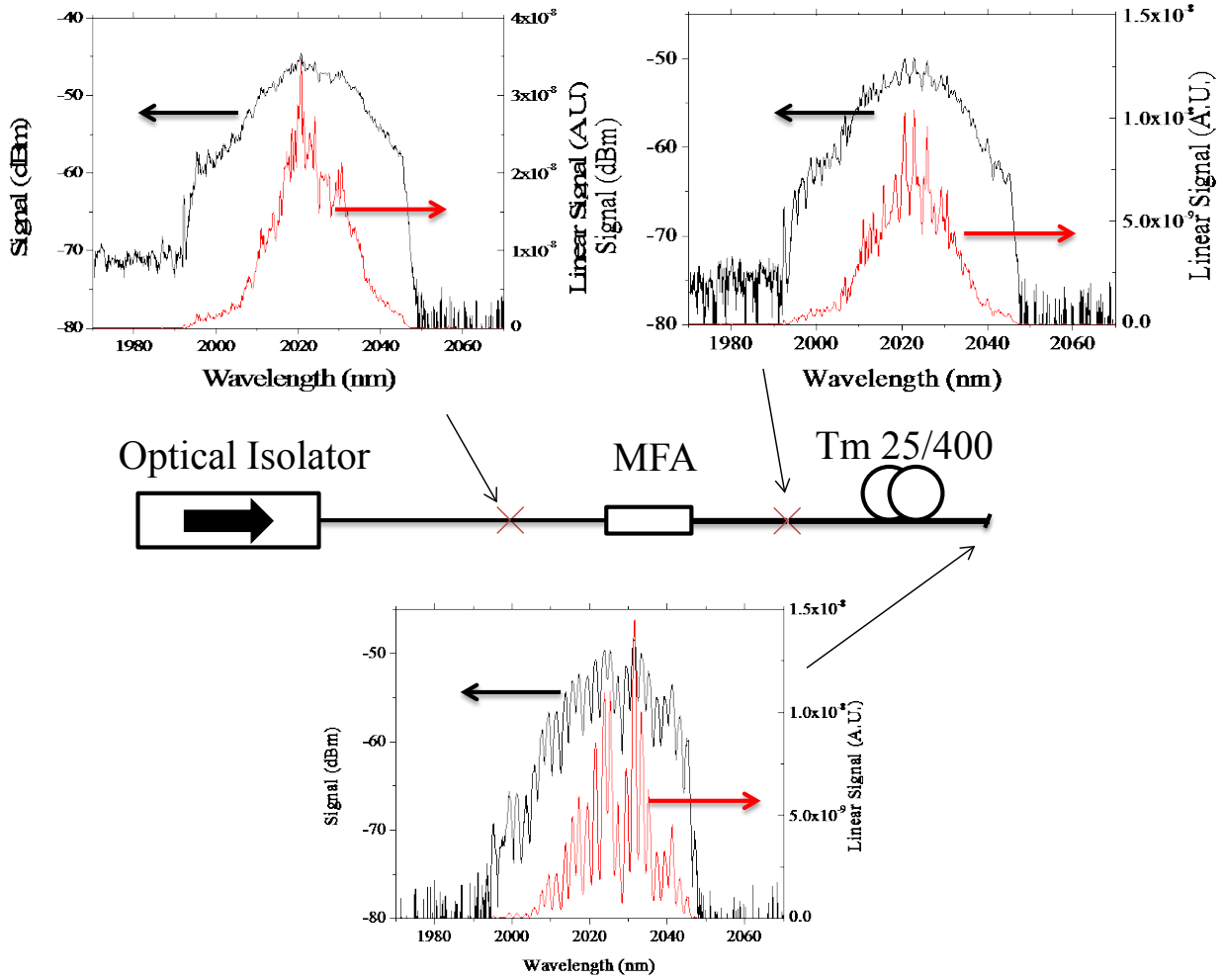


*Figure 76: Spectral comparison of different points in the LMA system to show origin of spectral modulation.*

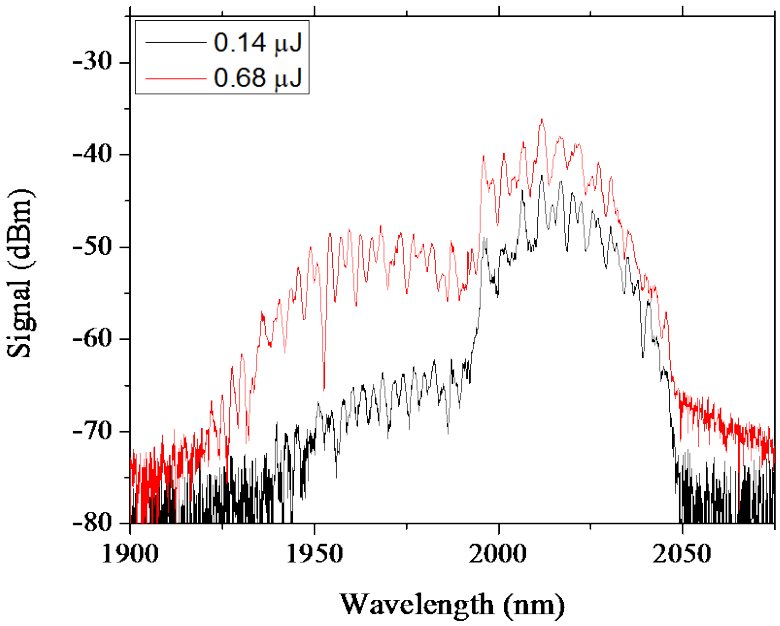


*Figure 77: Spectral modulations at two energy levels shows in that amplification is not drastically changed*

### *5.3.3 High Peak Power Model*

The high peak power system was computationally modeled using FiberDesk to compare with the results from the experimental setup. In the FiberDesk model a uniform gain was used so ASE is not present in the model. Also, the input pulse was approximated with a hyperbolic secant shape and was not spectrally modulated as was the case with the experimental setup. Output pulses from the Raman SSFS amplifier were spectrally filtered and stretched to 167 ps. Pulses were input into the UHNA and preamplifier stage with 0.8 nJ of energy and amplified to 10 nJ of energy in this first preamplifier stage. At this point in the experimental system pulses pass through the pulse picker, however in the computational model the repetition rate cannot be modified and maintain the nonlinear phase on the pulse. The repetition rate in the software has no effect on the amount of energy or peak power in a pulse, therefore, the repetition rate was not

modified at this point rather a linear loss to take in to account both the contrast ratio and duty cycle change was inserted at this point. After these linear loss elements were implement 1.525 nJ was input into the second single-mode preamplifier stage. The preamplifier amplified pulses to 100 nJ and then a LMA fiber was modeled with pulses amplified to 2.55 μJ.

The primary results from the model include the amount of nonlinear phase accumulation through the B-integral and the compressed pulse duration. The simulation for the B-Integral throughout the full CPA system is shown in Figure 78. After amplification in the LMA fiber to 2.55 μJ energy the B-Integral increased to 4 radians. This represents a value greater than π radians where SPM accumulation shoud affect the amount of energy in the compressed pulse. However, in the experimental work it does not appear we have reached the SPM limits of the system, although this is difficult to precisely determine with the modulations on the spectral output. One difference between the experimental and computational results is that the stretched pulse duration is estimated using the given parameter for the CBG, however the actual stretch pulse duration has not been measured. The autocorrelator delay is not long enough to measure >80 ps pulses and the fast photodiode, ET-5010F (Electro-Optics Technology, Inc), does not contain enough bandwidth to be used with a sampling oscilloscope to directly measure the pulse duration. Figure 79 shows the intensity of the compressed pulse duration in FiberDesk with the simulated autocorrelation shown. The pulse has modulation extending to positive 10 ps due to the TOD build up in the fibers and in the Treacy compressor.

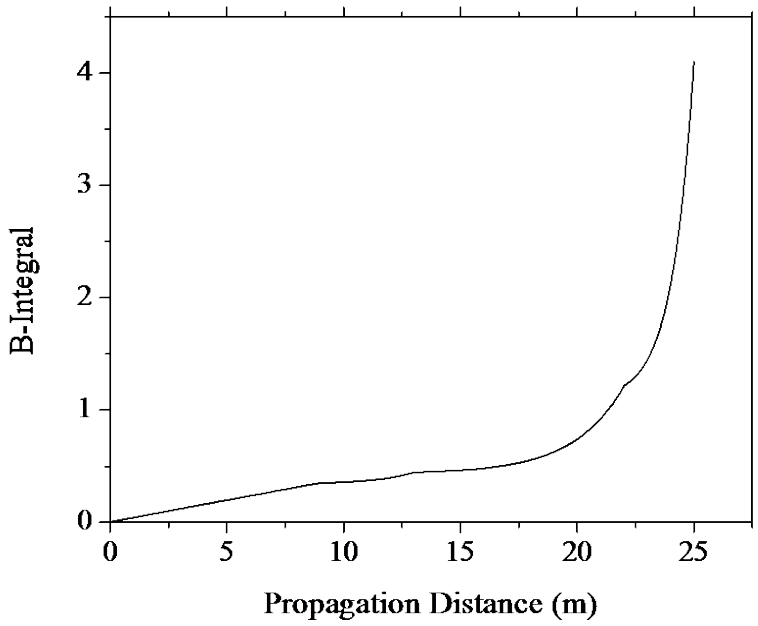


*Figure 78: B-Integral modeled in FiberDesk as a function of propagation distance in the high peak power CPA system.*

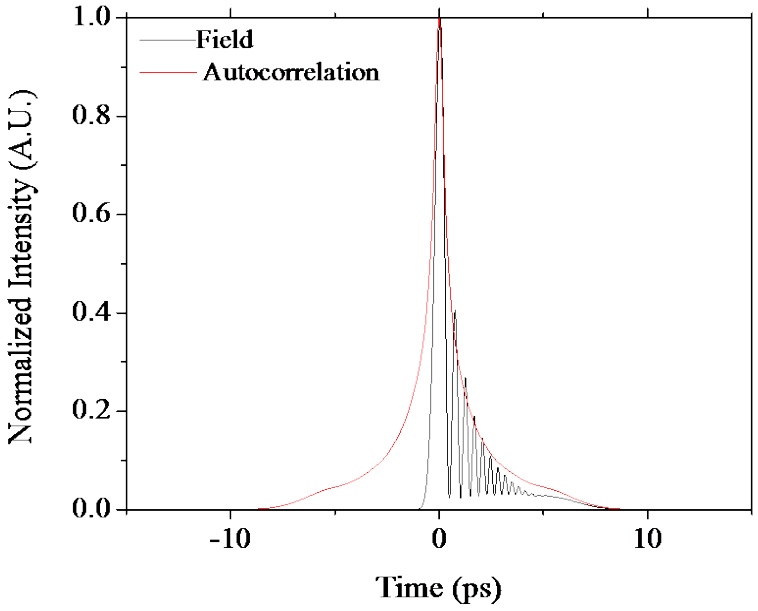


*Figure 79: FiberDesk model of the compressed pulse from an LMA amplifier operating at 2.6 μJ. The red line shows the intensity autocorrlation.*

# CHAPTER 6: MID-IR SUPERCONTINUUM WITH THULIUM CPA SOURCE

## 6.1 Theory

Supercontinuum generation is a process of broadening of spectral profile of a propagating pulse due to interplay between different nonlinear and linear effects in the pulse propagating medium. Different pulse regimes and dispersion profiles of the media lead to different characteristic mechanism of spectral broadening. In this section we will use the CPA source described in section 5.2 with CBG stretching and compressing to pump highly nonlinear fibers. We will demonstrate spectral broadening in tellurite fiber and supercontinuum generation in tapered chalcogenide fiber

### *6.1.1 Anomalous Dispersion Pumping*

The spectral characteristics of supercontinuum generation are dependent on a fibers nonlinearity and the position of the pump wavelength. More importantly it is the wavelength of the pump in comparison to the zero dispersion wavelength (ZDW) that dictates whether the broadening occurs through solitonic or non-solitonic behavior. In this section pump wavelengths in the anomalous dispersion regime will be introduced, however full descriptions can be found in [32,58].

Pulses that are in the anomalous regime with high enough peak power will form higher-order solitons that are perturbed by TOD and intra-pulse Raman scattering as described in Equation (21). Due to the perturbation from these effects these higher-order solitons will break apart into sub-pulses with lower-amplitude. Through intra-pulse Raman scattering higher frequency components will pump lower frequency components and cause a wavelength shift of

the constituent solitons from the soliton fission process. On the anomalous side of the ZDW these pulses that have undergone a Raman induced frequency shift produce the spectral broadening. However, on the normal dispersion side nonsolitonic radiation broadens the spectrum to shorter wavelengths. These frequencies appear because higher-order dispersion terms can transfer energy to narrow-band resonances in the normal regime and is determined by phase matching conditions [32,58].

### *6.1.2 Normal Dispersion Pumping*

The generation of supercontinuum in the anomalous regime is primarily instigated by soliton effects leading to very broad bandwidths; however, there are fluctuations in relative intensity and phase that lead to a low temporal coherence source [132–134]. The temporal coherence of a source is determined by the energy of input pulses, pulse width and wavelength. Pumping of fibers in the normal regime does not lead to soliton fission processes to achieve broadening unless near the ZDW. SPM processes lead to the broadening in the normally dispersive regime and lead to a temporally coherent spectrum. In this work we do not expect to be pumping in the region; however the use of fibers that allow broad coherent spectrum generation are important for developing single-cycle optical sources and generation of Mid-IR frequency combs [135].

## 6.2 Experimental Results

The laser system using CBG stretching and compressing emitted enough peak power (>10 kW) to generate spectral broadening. Two collaborations were setup to demonstrate

spectral broadening and supercontinuum generation in highly nonlinear tellurite and chalcogenide fiber.

### *6.2.1 Tellurite*

Extruded tellurite fibers with low OH content were prepared at the Institute for Photonics and Advanced Sensing in Adelaide, Australia by Heike Ebendorff-Heidepriem and Tanya Monro [136]. Two extruded samples were developed with a suspended core fiber design where the core sizes were 5 and 3.1 μm. The initial samples that were sent were in non-polymer coated rods that were ~ 30 cm, but during the shipping process were fragmented into pieces that were ~ 2.5 cm and 5 cm long for the 5 and 3.1 μm diameter, respectively.

Using the 5 μm, 2.5 cm long sample has a calculated nonlinear parameter $\gamma$ of 0.1539, an SEM image is seen in Figure 80. Coupling light into this fiber resulted in17% transmission of light through the fiber, however due to the relatively short length and larger diameter spectral broadening was not seen for input energies up to 20 nJ. Tests concluded at this value because the mechanical stability and thermal stability of the fiber was not known and we wished to avoid damaging the fiber.

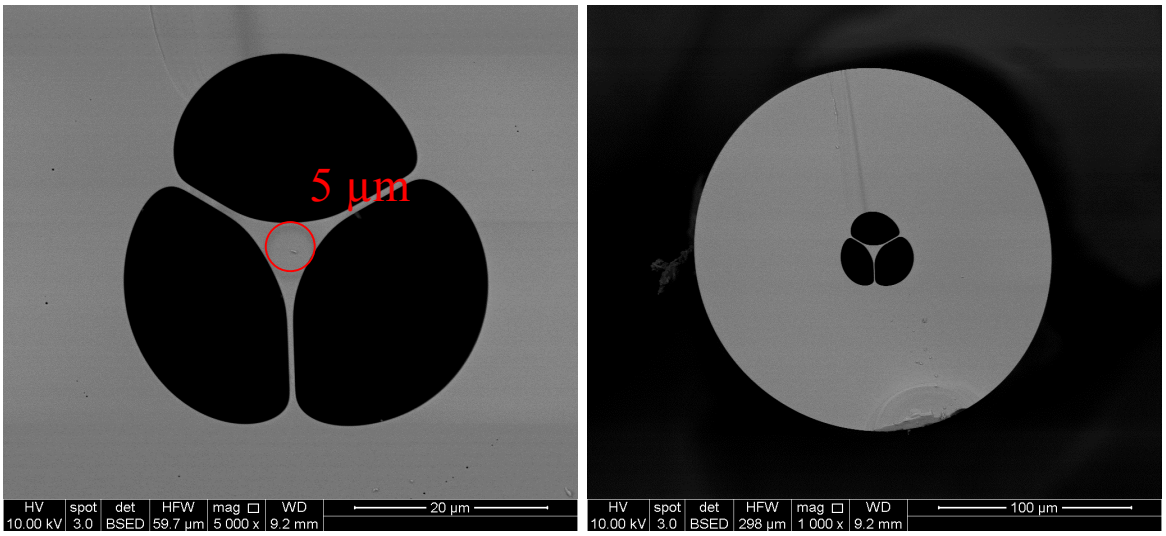


*Figure 80: SEM image of 5 µm extruded tellurite fiber with a suspended core.*

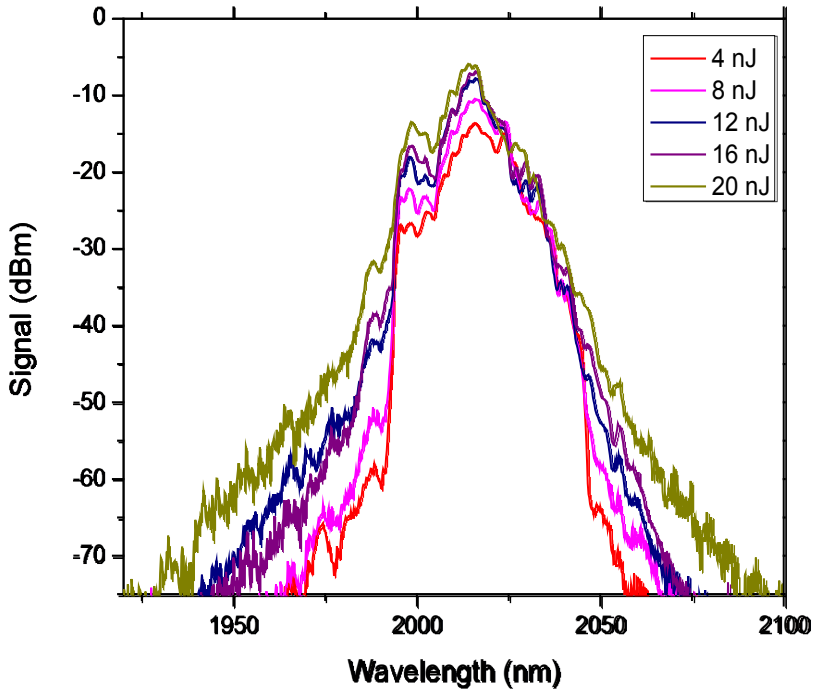


*Figure 81: Spectral output for different input energies with the 5 µm tellurite fiber.*

The 5 µm core sample was not an optimal sample due to the larger core area and relatively short length. However, using the 3.1 µm sample the core area increases the nonlinear

parameter to 0.4005 and the fiber length is ~5 cm. Using a 40x microscope objective light was coupled into this fiber with 12% transmission through. The optimal microscope objective for coupling into this fiber core diameter was a 60x objective however the clear aperture of the 60x objectives limited the energy of the beam into the fiber. Compressed pulses were coupled into the tellurite fiber with ~10% coupling efficiency at input energies of 2 nJ and 14 nJ corresponding to ~ 0.2 nJ and ~1.4 nJ in the fiber, respectively. Figure 10 shows the output spectra for these two energies. Using these coupling loss estimations, we estimate the maximum peak power in the fiber was ~3.5 kW, at which we observed spectral broadening from 1850 – 2300 nm at the -20 dB level. Simulation have shown that pumping similar $TeO_2$ fibers with 75 kW peak power at 1.93 µm, near the zero dispersion wavelength, spectral broadening should generate a supercontinuum from <1 µm to >4 µm [137].

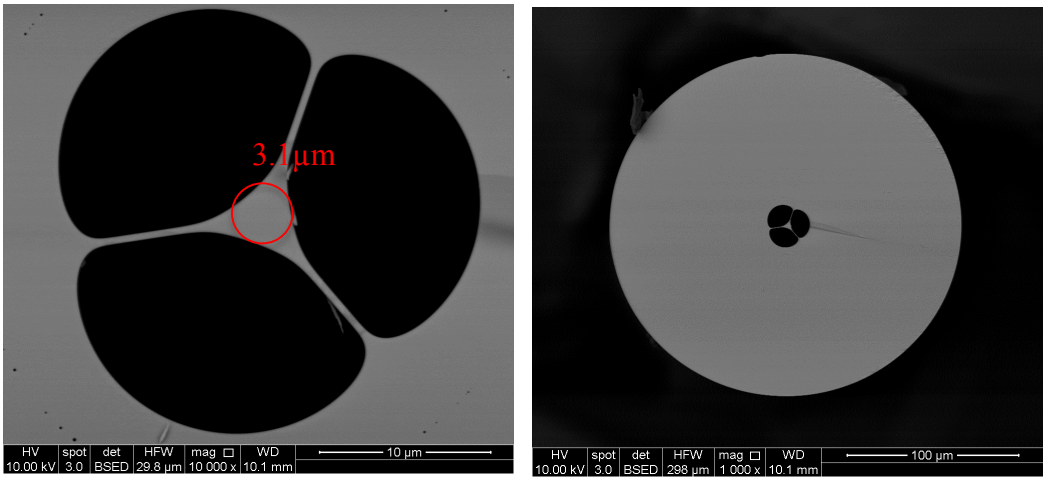


*Figure 82: SEM image of the 3 µm core diameter tellurite fiber.*

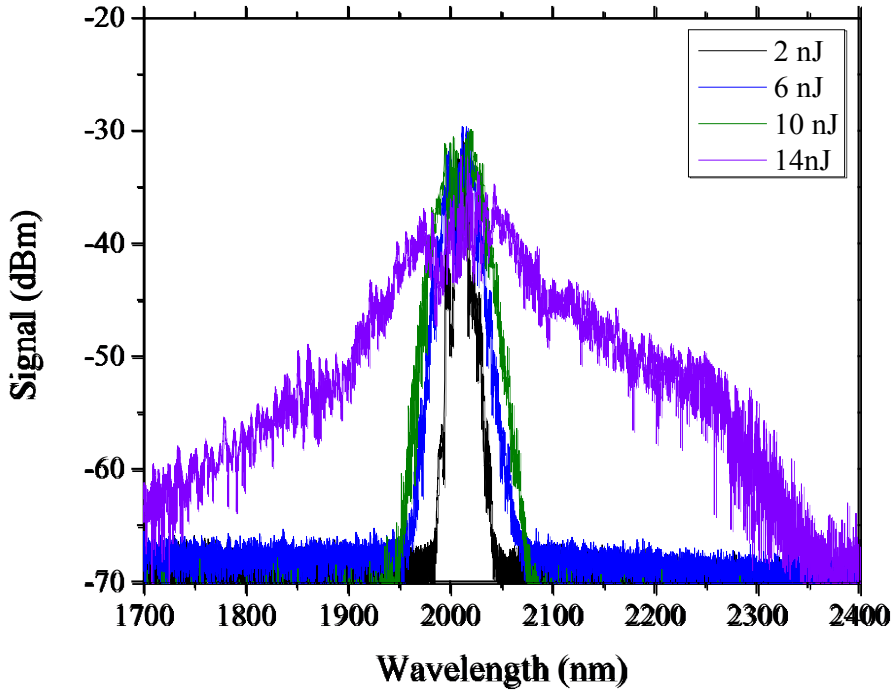


*Figure 83: Spectral broadening from a 3.1 m core diameter tellurite fiber [130].*

6.2.2 Chalcogenide

Chalcogenide core/clad structures were prepared by the multi-material optical fiber devices group at UCF headed by Prof. Ayman Abouraddy. The chalcogenide glasses and fibers were fabricated by Guangming Tao, while the tapers and the nonlinear measurements were performed by Soroush Shabahang [138]. This chalcogenide fiber contained an $As_2Se_{1.5}S_{1.5}$ core and $As_2S_3$ clad glasses and was tapered to a minimum diameter of 250 nm [139]. The fiber used was 6.8 cm long. Approximately 5 nJ was launched into the fiber with 9.8 kW of peak power with 450 fs pulses. Using this highly nonlinear fiber supercontinuum spanned from 1000-3150 nm 20dB from the peak. In order to measure this broad spectrum 2 optical spectrum analyzers spanning 900-2400 nm were used. For the wavelengths > 2.4 μm an amplified PbS and PbSe

detectors were used in conjunction with a monochometer to measure long wavelengths. While the PbS and PbSe detectors respond at these Mid-IR wavelengths the noise floor is relatively high compared to liquid nitrogen cooled InSb or MCT detectors. Therefore, it is possible that the spectrum extends further than 3150 nm and the noise in the detector limits the detection. In order to taper the chalcogenide fiber to the 250 nm diameter there is a polymer coating around the cladding that also limits the generated spectrum due to absorption of light.

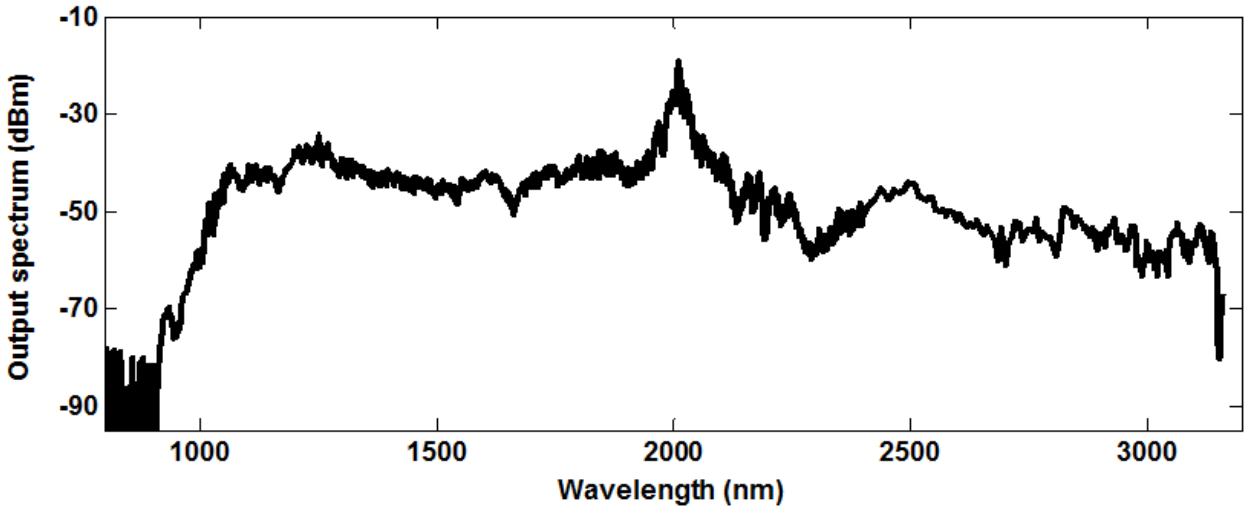


*Figure 84: Supercontinuum spanning 1- 3.1 µm pumped by a 2um CPA system.*

# CHAPTER 7: CONCLUSIONS AND PERSPECTIVES

Advancements in Tm doped fiber have shown the dopant's potential as a source for high average power applications in both absorptive regions and transmissive regions of the atmosphere due to its large tuning range. This large tuning range also corresponds to a wide gain bandwidth capable of producing and amplifying ultrashort pulses.

High average power systems are limited by thermal and nonlinear constraints that will hinder the amount of average power out of a single aperture. Thulium doped fibers, while high efficiencies are possible, have a large quantum defect heating that will provide the main limitation to producing kW class systems, for non-single frequency systems. In this thesis spectral beam combining was posed as a method to both combine diffraction-limited fiber lasers and deliver light in regions of the atmosphere with high transmission.

We utilized meta-optic filters to lock the wavelength and polarization of multiple Tm:fiber MOPA systems and used bandpass filters to combine lasers with 5 nm wavelength spacing. This wavelength spacing is presently the primary limitation to massively combining many lasers in this transmissive wavelength region. The use of filter technologies and polarized laser sources allows for polarization combining as well as spectral beam combining. In this work we combined three laser channels operating with ~100 W per channel to a combined power of 253 W with 89% coupling efficiency. At these powers, we observed no signs of thermal or mechanical degradation; therefore, power scaling via SBC should be possible into the multi-kW regime.

Recently the generation and amplification of ultrashort pulses in Tm has drawn more attention due to the ability of using novel materials for broadband Mid-IR generation and OPAs. This increased attention has confirmed some of the promise of Tm:fiber based systems but there are still many unanswered questions about the full extent to which Tm can be used as a high peak power source.

As part of this thesis, a Tm ultrashort pulse system was designed and constructed from the oscillator through multiple stages of amplification utilizing relatively long pulse duration stretching CPA. Development of the oscillator led to a laser that produced 800 fs pulses with low energy that seeded a nonlinear amplifier to generate tunable pulses through a soliton self-frequency shift process, with 3 nJ energy with 150 pulse duration. Using this source numerous pathways for amplification were examined including examination of gain narrowing in an amplifier, developing a modest powered CPA system using CBGs for stretching and compressing, and finally a high peak power system that examined the nonlinear limitations of amplifying in Tm.

One of the more promising features of Tm doped in silica fiber is its large bandwidth amplification of ultrashort pulses. In this work we showed amplification of pulses with 60 nm of bandwidth with minimal gain narrowing. Pulses with this bandwidth are capable of generating sub-100 fs pulse and with the possibility of amplifying these pulses a CPA system approaching GW peak powers could be feasible. Presently the highest peak power systems and average power system at 1 μm have only been able to amplify and compress pulses to sub-500 fs with gain narrowing being a primary limitation.

In order design a system with sub-100 fs compressed pulse durations that approaches GW peak powers a few of the limitations have been shown in this dissertation, but a much more concerted effort to overcome these challenges is necessary. Presently, advances in fiber types allow for mode-field diameters approaching 80 μm in rod-type PCF with thulium as a dopant; thus, nonlinear limitations by the actual gain stage should be low with long stretched pulse durations. Generating pulses with sub-100 fs pulse duration requires improvements to the oscillator, specifically moving to designs that operate in the stretched-pulse regime. Alternatively, it is possible to pump a fiber in the normally dispersion regime to attain coherent spectral broadening, as was presented in this thesis to generate >60 nm bandwidth.

Management of this bandwidth through the amplification and compression process becomes the primary concern to developing this type system. In order to achieve GW peak powers both fine control over the higher-order phase terms and large stretch and compression durations are necessary. The spectral phase terms can be controlled using an acousto-optic programmable dispersive filter to help cancel out TOD and higher order terms. To amplify pulses to the mJ energy it is expected that nanosecond pulse durations are necessary. However, while possible in 2 μm laser system gratings will need to be optimized to 800 ln/mm line densities and large enough to handle the spatial distribution after dispersion. The stretcher and compressor are limitations because the amount of physical space needed to stretch pulses and maintain the full bandwidth on a grating. These precautions and limitations mentioned are related to the engineering limitations of this system thus can be overcome. The main scientific question related to this type of system is what is the maximum bandwidth that can be uniformly amplified

in Tm:fiber. A fiber based system with these parameters is useful for use in high harmonic generation and possible can produce higher peak powers than system operating at 1 μm.

Develop of femtosecond sources at 2 μm has gained interest in the past few years but many questions about the extent to a Tm:fiber systems maximum energy and bandwidth are still answerable. The results showing 60 nm bandwidth amplification and amplification to 1 μJ while maintaining sub-500 fs pulses after compression without taking into account TOD provide a basis that mJ energies and sub-100 fs pulses are possible. With these achievable goals and through the use of robust fiber packages extremely high peak power systems should be possible in the future.

# REFERENCES


1. A. Yariv, *Optical Electroncs in Modern Communications*, 5th ed (Oxford University Press, 1997).

2. C. J. Koester and E. Snitzer, "Amplification in a Fiber Laser," Applied Optics **3**, 1182 (1964).

3. E. Snitzer, "Optical Maser Action of Nd^{+ 3} in a Barium Crown Glass," Physical Review Letters **7**, 444–446 (1961).

4. J. Stone, "Neodymium-doped silica lasers in end-pumped fiber geometry," Applied Physics Letters **23**, 388 (1973).

5. E. Snitzer, H. Po, and F. Hakimi, "Double clad, offset core Nd fiber laser," Optical Fiber Sensors 1–4 (1988).

6. J. C. Knight, "Photonic crystal fibres.," Nature **424**, 847–51 (2003).

7. a Tünnermann, T. Schreiber, F. Röser, A. Liem, S. Höfer, H. Zellmer, S. Nolte, and J. Limpert, "The renaissance and bright future of fibre lasers," Journal of Physics B: Atomic, Molecular and Optical Physics **38**, S681–S693 (2005).

8. L. Fu, H. a McKay, and L. Dong, "Extremely large mode area optical fibers formed by thermal stress.," Optics express **17**, 11782–93 (2009).

9. O. Schmidt, J. Rothhardt, T. Eidam, F. Röser, J. Limpert, a Tünnermann, K. P. Hansen, C. Jakobsen, and J. Broeng, "Single-polarization ultra-large-mode-area Yb-doped photonic crystal fiber.," Optics express **16**, 3918–23 (2008).

10. F. Stutzki, F. Jansen, A. Liem, C. Jauregui, J. Limpert, and A. Tunnermann, "26 mJ, 130 W Q-switched fiber-laser system with near-diffraction-limited beam quality," Optics Letters **37**, 1073–1075 (2012).

11. J. Limpert, N. Deguil-Robin, I. Manek-Hönninger, F. Salin, F. Röser, a Liem, T. Schreiber, S. Nolte, H. Zellmer, a Tünnermann, J. Broeng, a Petersson, and C. Jakobsen, "High-power rod-type photonic crystal fiber laser.," Optics express **13**, 1055–8 (2005).

12. J. C. Baggett, T. M. Monro, K. Furusawa, V. Finazzi, and D. . Richardson, "Understanding bending losses in holey optical fibers," Optics Communications **227**, 317–335 (2003).

13. C. Liu, G. Chang, N. Litchinitser, and A. Galvanauskas, "Effectively Single-Mode Chirally-Coupled Core Fiber," 1–3 (2007).

14. A. Siegman, "Gain-guided, index-antiguided fiber lasers," JOSA B **24**, 1677–1682 (2007).

15. L. Dong, X. Peng, and J. Li, "Leakage channel optical fibers with large effective area," Journal of the Optical Society of America B **24**, 1689 (2007).

16. F. Gonthier and L. Martineau, "High-power All-Fiber component:- The missing link for high-power fiber lasers," Proceedings of SPIE Photonics West (2004).

17. "ITF Labs," http://www.3spgroup.com/ITFLabs/Home.php?Line_no=11&locale=en.

18. M. E. Fermann, "Single-mode excitation of multimode fibers with ultrashort pulses.," Optics letters **23**, 52–4 (1998).

19. M. Kihara, S. Tomita, and M. Matsumoto, "Loss characteristics of thermally diffused expanded core fiber," IEEE Photonics Technology Letters **4**, 1390–1391 (1992).

20. M. Faucher and Y. K. Lize, "Mode Field Adaptation for High Power Fiber Lasers," 2007 Conference on Lasers and Electro-Optics (CLEO) 1–2 (2007).

21. A. Alves, R. Romero, M. Photonics, R. Eng, and F. Ulrich, "Mode Field Adapters for application in High Power Fiber Lasers," **248**, 4470 (2007).

22. T. Uchida and A. Ueki, "Optical Isolator," (1979).

23. L. Ng and E. Taylor, "Thulium-doped tellurite fiber for S-band amplification," in *28th European Conference on Optical Communication* (2002), Vol. 2, pp. 30–31.

24. S. Jiang, J. Wu, Z. Yao, and J. Zong, "104 W Highly Efficient Thulium Doped Germanate Glass Fiber Laser," 11–13 (2007).

25. S. D. Jackson, "The spectroscopic and energy transfer characteristics of the rare earth ions used for silicate glass fibre lasers operating in the shortwave infrared," Laser & Photonics Review **3**, 466–482 (2009).

26. S. D. Jackson and S. Mossman, "Efficiency dependence on the Tm3+ and Al3+ concentrations for Tm3+-doped silica double-clad fiber lasers.," Applied optics **42**, 2702–7 (2003).

27. T. Ehrenreich, R. Leveille, I. Majid, K. Tankala, G. Rines, and P. Moulton, "1 kW, All-Glass Tm:fiber laser," in *SPIE Photonics West* (2010).

28. P. G. Wilcox, W. E. Torruellas, M. L. Dennis, J. W. Warren, G. P. Frith, T. S. McComb, and B. Samson, "Comprehensive model of double cladding Thulium-doped fibers pumped at 795 nm," in *SPIE Photonics West* (2009).

29. S. Jackson, "Cross relaxation and energy transfer upconversion processes relevant to the functioning of 2 μm Tm3+-doped silica fibre lasers," Optics Communications **230**, 197–203 (2004).

30. J. Faist, F. Capasso, D. L. Sivco, C. Sirtori, A. L. Hutchinson, and A. Y. Cho, "Quantum Cascade Laser," 1–4 (1986).

31. F. Capasso, "High-performance midinfrared quantum cascade lasers," Optical Engineering **49**, 111102 (2010).

32. J. M. Dudley, G. Genty, and S. Coen, "Supercontinuum generation in photonic crystal fiber," Reviews of Modern Physics **78**, 1135–1184 (2006).

33. F. Lu, Y. Deng, and W. H. Knox, "Generation of broadband femtosecond visible pulses in dispersion-micromanaged holey fibers.," Optics letters **30**, 1566–8 (2005).

34. J. Herrmann, U. Griebner, N. Zhavoronkov, a. Husakou, D. Nickel, J. C. Knight, W. J. Wadsworth, P. S. J. Russell, and G. Korn, "Experimental Evidence for Supercontinuum Generation by Fission of Higher-Order Solitons in Photonic Fibers," Physical Review Letters **88**, 1–4 (2002).

35. A. V. Husakou and J. Herrmann, "Supercontinuum Generation of Higher-Order Solitons by Fission in Photonic Crystal Fibers," Physical Review Letters **87**, 85–88 (2001).

36. "http://www.nktphotonics.com/supercontinuum_sources," http://www.nktphotonics.com/supercontinuum_sources.

37. J. H. V. Price, T. M. Monro, H. Ebendorff-Heidepriem, F. Poletti, P. Horak, V. Finazzi, J. Y. Y. Leong, P. Petropoulos, J. C. Flanagan, G. Brambilla, X. Feng, and D. J. Richardson, "Mid-IR Supercontinuum Generation From Nonsilica Microstructured Optical Fibers," IEEE Journal of Selected Topics in Quantum Electronics **13**, 738–749 (2007).

38. E. M. Vogel, M. J. Weber, and D. M. Krol, "Nonlinear optical phenomena in glass," Physics and chemistry of glasses **32**, 231–254 (n.d.).

39. S. Fujino and K. Morinaga, "Material Dispersion and its compositional parameter of oxide glasses," Journal of Non-Crystalline Solids **222**, 316–320 (1997).

40. J. M. Harbold, F. O. Ilday, F. W. Wise, J. S. Sanghera, V. Q. Nguyen, L. B. Shaw, and I. D. Aggarwal, "Highly nonlinear As-S-Se glasses for all-optical switching," Optics Letters **27**, 119–121 (2002).

41. J. Fatome, C. Fortier, T. Chartier, F. Smektala, K. Messaad, B. Kibler, S. Pitois, G. Gadret, C. Finot, J. Troles, F. Desevedavy, P. Houizot, G. Renversez, L. Brilland, and N. Traynor, "Linear and Nonlinear Characterizations of Chalcogenide Photonic Crystal Fibers," Journal of Lightwave Technology **27**, 1707–1715 (2009).

42. B. Ung and M. Skorobogatiy, "Chalcogenide microporous fibers for linear and nonlinear applications in the mid-infrared.," Optics express **18**, 8647–59 (2010).

43. "www.ipgphotonics.com," .

44. G. Goodno, L. Book, and J. Rothenberg, "Low-phase-noise, single-frequency, single-mode 608 W thulium fiber amplifier," Optics letters **34**, 1204–1206 (2009).

45. S. D. Jackson, "Power scaling method for 2-mm diode-cladding-pumped Tm 3 + -doped silica fiber lasers that uses Yb 3 + codoping," **28**, 2192–2194 (2003).

46. M. Meleshkevich, N. Platonov, D. Gapontsev, A. Drozhzhin, V. Sergeev, and V. Gapontsev, "415 W Single-Mode CW Thulium Fiber Laser in all-fiber format," in *The European Conference on Lasers and Electro-Optics* (2007).

47. D. J. Richardson, J. Nilsson, and W. A. Clarkson, "High power fiber lasers : current status and future perspectives [ Invited ]," America **27**, (2010).

48. D. Y. Shen, J. I. Mackenzie, J. K. Sahu, W. A. Clarkson, and S. D. Jackson, "High-Power and Ultra-Efficient Operation of a Tm 3+ -doped Silica Fiber Laser," 516–520 (2005).

49. W. a Clarkson, N. P. Barnes, P. W. Turner, J. Nilsson, and D. C. Hanna, "High-power cladding-pumped Tm-doped silica fiber laser with wavelength tuning from 1860 to 2090 nm.," Optics letters **27**, 1989–91 (2002).

50. G. Frith, D. G. Lancaster, and S. D. Jackson, "85 W Tm 3þ -doped silica fibre laser," **41**, 3–4 (2005).

51. D. C. Brown and H. J. Hoffman, "Thermal, stress, and thermo-optic effects in high average power double-clad silica fiber lasers," Quantum Electronics, IEEE Journal of **37**, 207–217 (2001).

52. J. W. Dawson, M. J. Messerly, R. J. Beach, M. Y. Shverdin, E. a Stappaerts, A. K. Sridharan, P. H. Pax, J. E. Heebner, C. W. Siders, and C. P. J. Barty, "Analysis of the

scalability of diffraction-limited fiber lasers and amplifiers to high average power.," Optics express **16**, 13240–66 (2008).

53. W. F. Krupke, M. D. Shinn, J. E. Marion, J. A. Caird, and S. E. Stokowski, "Spectroscopic , optical , and thermomechanical properties of gadolinium scandium gallium garnet," **3**, 102–114 (1986).

54. D. E. Gray, *American Institute of Physics Handbook*, 3rd editio (McGraw-Hill, 1972).

55. W. Koechner, *Solid-State Laser Engineering*, 5th ed. (Springer, 2006).

56. G. D. Goodno, L. D. Book, J. E. Rothenberg, M. E. Weber, and S. Benjamin Weiss, "Narrow linewidth power scaling and phase stabilization of 2-μm thulium fiber lasers," Optical Engineering **50**, 111608 (2011).

57. S. C. Tidwell, J. F. Seamans, M. S. Bowers, and A. K. Cousins, "Scaling CW Diode-End-Pumped Nd : YAG Lasers to," **28**, (1992).

58. G. P. Agrawal, *Nonlinear Fiber Optics*, 4th ed. (Academic Press, 2007).

59. T. Y. Fan, "Laser beam combining for high power, high-radiance sources," IEEE J. Sel. Top. Quantum Eletron. **11**, 567–577 (2005).

60. S. J. Mcnaught, C. P. Asman, H. Injeyan, A. Jankevics, A. M. F. Johnson, G. C, H. Komine, J. Machan, J. Marmo, M. Mcclellan, R. Simpson, J. Sollee, M. Valley, M. Weber, and S. B. Weiss, "100-kW Coherently Combined Nd:YAG MOPA Laser Array," Power 2–3 (2009).

61. M. C. Farries, A. C. Carter, G. G. Jones, and I. Bennion, "Tunable Multiwavelength semiconductor laser with single fibre output," Electronics Letters **27**, 1498–1499 (1991).

62. C. C. (MIT L. L. Cook and T. Y. Fan, "Spectral Beam Combining of Yb-doped Fiber Lasers in an External Cavity," in *OSA/ASSL* (OSA, 1999), pp. 163–166.

63. C. Wirth, O. Schmidt, I. Tsybin, T. Schreiber, R. Eberhardt, J. Limpert, A. Tünnermann, K. Ludewigt, M. Gowin, E. ten Have, and M. Jung, "High average power spectral beam combining of four fiber amplifiers to 8.2 kW.," Optics letters **36**, 3118–20 (2011).

64. C. Wirth, O. Schmidt, I. Tsybin, T. Schreiber, T. Peschel, F. Brückner, T. Clausnitzer, J. Limpert, R. Eberhardt, a Tünnermann, M. Gowin, E. ten Have, K. Ludewigt, and M. Jung, "2 kW incoherent beam combining of four narrow-linewidth photonic crystal fiber amplifiers.," Optics express **17**, 1178–83 (2009).

65. P. Madasamy, D. R. Jander, C. D. Brooks, T. H. Loftus, A. M. Thomas, P. Jones, and E. C. Honea, "Dual-Grating Spectral Beam Combination of High-Power Fiber Lasers," IEEE Journal of Selected Topics in Quantum Electronics **15**, 337–343 (2009).

66. O. Andrusyak, V. Smirnov, G. Venus, V. Rotar, and L. Glebov, "Spectral Combining and Coherent Coupling of Lasers by Volume Bragg Gratings," IEEE Journal of Selected Topics in Quantum Electronics **15**, 344–353 (2009).

67. K. Regelskis, K.-C. Hou, G. Raciukaitis, and A. Galvanauskas, "Spatial-dispersion-free spectral beam combining of high power pulsed Yb-doped fiber lasers," 2008 Conference on Lasers and Electro-Optics 1–2 (2008).

68. O. Schmidt, C. Wirth, D. Nodop, J. Limpert, T. Schreiber, T. Peschel, R. Eberhardt, and a Tünnermann, "Spectral beam combination of fiber amplified ns-pulses by means of interference filters.," Optics express **17**, 22974–82 (2009).

69. W. A. Clarkson, V. Matera, A. M. Abdolvand, T. M. J. Kendall, D. C. Hanna, J. Nilsson, and P. W. Turner, "SBC of Cladding Pumped Tm Doped Fiber Lasers," in *QEP* (2001).

70. T. Erdogan, "Cladding-mode resonances in short- and long-period fiber grating filters," Journal of the Optical Society of America A **14**, 1760 (1997).

71. T. Erdogan, "Fiber Grating Spectra," **15**, 1277–1294 (1997).

72. K. O. Hill and G. Meltz, "Fiber Bragg grating technology fundamentals and overview," Journal of Lightwave Technology **15**, 1263–1276 (1997).

73. J. Thomas, E. Wikszak, T. Clausnitzer, U. Fuchs, U. Zeitner, S. Nolte, and a. Tünnermann, "Inscription of fiber Bragg gratings with femtosecond pulses using a phase mask scanning technique," Applied Physics A **86**, 153–157 (2006).

74. J. W. Kim, P. Jelger, J. K. Sahu, F. Laurell, and W. A. Clarkson, "High-power and wavelength-tunable operation of an Er,Yb fiber laser using a volume Bragg grating," Opt. Lett. **33**, 1204–1206 (2008).

75. W. Mohammed and X. Gu, "Fiber Bragg grating in large-mode-area fiber for high power fiber laser applications.," Applied optics **49**, 5297–301 (2010).

76. Y. J. Zhang, W. Wang, S. F. Song, and Z. G. Wang, "Ultra-narrow linewidth Tm 3+ -doped fiber laser based on intra-core fiber Bragg gratings," Laser Physics Letters **6**, 723–726 (2009).

77. Y. J. Zhang, B. Q. Yao, S. F. Song, and Y. L. Ju, "All-fiber Tm-doped double-clad fiber laser with multi-mode FBG as cavity," Laser Physics **19**, 1006–1008 (2009).

78. Z. Yun-Jun, W. Wei, Z. Ren-Lai, S. Shi-Fei, T. Yi, and W. Yue-Zhu, "Narrow Linewidth Tm 3+ -Doped Large Core Fiber Laser Based on a Femtosecond Written Fiber Bragg Grating," Chinese Physics Letters **27**, 074214 (2010).

79. Y. Tang, C. Huang, S. Wang, H. Li, and J. Xu, "High-power narrow-bandwidth thulium fiber laser with an all-fiber cavity," Optics Express **20**, 358–360 (2012).

80. L. B. Glebov, "Photosensitive Glass for phse hologram recording," Glass Science and Technology **71C**, 1998 (1998).

81. P. Jelger, P. Wang, J. K. Sahu, F. Laurell, and W. a Clarkson, "High-power linearly-polarized operation of a cladding-pumped Yb fibre laser using a volume Bragg grating for wavelength selection.," Optics express **16**, 9507–12 (2008).

82. T. McComb, V. Sudesh, and M. Richardson, "Volume Bragg grating stabilized spectrally narrow Tm fiber laser.," Optics letters **33**, 881–3 (2008).

83. T. S. McComb, R. A. Sims, C. C. C. Willis, P. Kadwani, V. Sudesh, L. Shah, and M. Richardson, "High-power widely tunable thulium fiber lasers," Appl. Opt. **49**, 6236–6242 (2010).

84. a. Hessel and a. a. Oliner, "A New Theory of Wood's Anomalies on Optical Gratings," Applied Optics **4**, 1275 (1965).

85. S. S. Wang and R. Magnusson, "Theory and applications of guided-mode resonance filters," Appl. Opt. **32**, 2606–2613 (1993).

86. A. a. Mehta, R. C. Rumpf, Z. a. Roth, and E. G. Johnson, "Guided Mode Resonance Filter as a Spectrally Selective Feedback Element in a Double-Cladding Optical Fiber Laser," IEEE Photonics Technology Letters **19**, 2030–2032 (2007).

87. R. A. Sims, T. Dax, Z. Roth, T. S. McComb, L. Shah, V. Sudesh, M. Poutous, E. Johnson, and M. Richardson, "Spectral narrowing and stabilization of thulium fiber lasers using guided-mode resonance filters," in *Fiber Lasers VII: Technology, Systems, and Applications*, K. Tankala, ed. (SPIE, 2010), Vol. 7580, p. 75800F.

88. R. A. Sims, Z. Roth, T. McComb, L. Shah, V. Sudesh, P. Menelaos, E. Johnson, and M. C. Richardson, "Guided Mode Resonance Filters as Stable Line-Narrowing Feedback Elements for Tm Fiber Lasers," in *Conference on Lasers and Electro-Optics/International Quantum Electronics Conference* (Optical Society of America, 2009), p. CThN2.

89. R. A. Sims, Z. a Roth, C. C. C. Willis, P. Kadwani, T. S. McComb, L. Shah, V. Sudesh, M. Poutous, E. G. Johnson, and M. Richardson, "Spectral narrowing and stabilization of

thulium fiber lasers using guided-mode resonance filters.," Optics letters **36**, 737–9 (2011).

90. L. Shah, R. A. Sims, P. Kadwani, C. C. C. Willis, J. B. Bradford, A. Pung, M. K. Poutous, E. G. Johnson, and M. Richardson, "Integrated Tm:fiber MOPA with polarized output and narrow linewidth with 100 W average power," Optics Express **20**, 20558 (2012).

91. T. S. McComb, P. K. Kadwani, R. A. Sims, L. Shah, C. C. C. Willis, G. Frith, V. Sudesh, B. Samson, and M. Richardson, "Atmospheric Transmission Testing Using a Portable, Tunable, High Power Thulium Fiber Laser System," in *Advanced Solid-State Photonics*, W. A. Clarkson, N. Hodgson, and R. K. Shori, eds. (Optical Society of America, 2010), Vol. 49, p. JThJ5.

92. R. A. Sims, C. C. C. Willis, P. Kadwani, T. S. McComb, L. Shah, V. Sudesh, Z. Roth, M. K. Poutous, E. G. Johnson, and M. Richardson, "Spectral beam combining of 2μm Tm fiber laser systems," Optics Communications **284**, 1988–1991 (2011).

93. T. S. Mccomb, "Power scaling of large mode area thulium fiber lasers in various spectral and temporal regimes," Power (2009).

94. E. C. Cheung, J. G. Ho, T. S. McComb, and S. Palese, "High density spectral beam combination with spatial chirp precompensation.," Optics express **19**, 20984–90 (2011).

95. "www.fiberdesk.com," .

96. M. E. Fermann, V. I. Kruglov, B. C. Thomsen, J. M. Dudley, and J. D. Harvey, "Self-Similar Propagation and Amplification of Parabolic Pulses in Optical Fibers," Phys. Rev. Lett. **84**, 6010–6013 (2000).

97. V. I. Kruglov, a C. Peacock, J. M. Dudley, and J. D. Harvey, "Self-similar propagation of high-power parabolic pulses in optical fiber amplifiers.," Optics letters **25**, 1753–5 (2000).

98. H. A. Haus, "Theory of Mode Locking with a Slow Saturable Absorber," IEEE Journal of Quantum Electronics **11**, 736–746 (1975).

99. A. M. Weiner, *Ultrafast Optics*, 1st ed. (John Wiley & Sons, Inc, 2009).

100. S. Iijimia, "Helical microtubules of graphitic carbon," Nature **354**, 56–58 (1991).

101. S. Y. Set, H. Yaguchi, Y. Tanaka, and M. Jablonski, "Ultrafast Fiber Pulsed Lasers Incorporating Carbon Nanotubes," IEEE Journal of Selected Topics in Quantum Electronics **10**, 137–146 (2004).

102. T. Hasan, Z. Sun, F. Wang, F. Bonaccorso, P. H. Tan, A. G. Rozhin, and A. C. Ferrari, "Nanotube Polymer Composites for Ultrafast Photonics," Advanced Materials **21**, 3874–3899 (2009).

103. J. W. Nicholson, R. S. Windeler, and D. J. Digiovanni, "Optically driven deposition of single-walled carbon-nanotube saturable absorbers on optical fiber end-faces.," Optics express **15**, 9176–83 (2007).

104. K. Kieu and M. Mansuripur, "Femtosecond laser pulse generation with a fiber taper embedded in carbon nanotube/polymer composite," Optics Letters **32**, 2242–4 (2007).

105. K. Kieu and F. W. Wise, "Soliton Thulium-Doped Fiber Laser With Carbon Nanotube Saturable Absorber," IEEE Photonics Technology Letters **21**, 128–130 (2009).

106. M. Hofer, M. E. Fermann, F. Haberl, M. H. Ober, and a J. Schmidt, "Mode locking with cross-phase and self-phase modulation.," Optics letters **16**, 502–4 (1991).

107. G. P. Agrawal, *Application of Nonlinear Fiber Optics*, 2nd ed. (Academic Press, 2008).

108. M. Fermann and M. Andrejco, "Passive mode locking by using nonlinear polarization evolution in a polarization-maintaining erbium-doped fiber," Optics letters **18**, 894–896 (1993).

109. S. Zhou, L. Kuznetsova, A. Chong, and F. Wise, "Compensation of nonlinear phase shifts with third-order dispersion in short-pulse fiber amplifiers.," Optics express **13**, 4869–77 (2005).

110. J. P. Gordon, "Theory of the soliton self-frequency shift.," Optics letters **11**, 662–4 (1986).

111. P. Beaud and W. Hodel, "Ultrashort pulse propagation, pulse breakup, and fundamental soliton formation in a single-mode optical fiber," IEEE Journal of Quantum Electronics **QE-23**, 1938–1946 (1987).

112. D.-H. Kim, J. U. Kang, and J. B. Khurgin, "Cascaded Raman self-frequency shifted soliton generation in an Er/Yb-doped fiber amplifier," Applied Physics Letters **81**, 2695 (2002).

113. G. Imeshev and M. Fermann, "230-kW peak power femtosecond pulses from a high power tunable source based on amplification in Tm-doped fiber," Optics Express **13**, 7424–31 (2005).

114. S. Kivisto and T. Hakulinen, "Tunable Raman soliton source using mode-locked Tm–Ho fiber laser," IEEE Photonics Technology Letters **19**, 934–936 (2007).

115. N. Leindecker, A. Marandi, R. L. Byer, K. L. Vodopyanov, I. Hartl, M. Fermann, and P. G. Schunemann, "Octave-spanning ultrafast OPO with 2.6-6.1 μm instantaneous bandwidth pumped by femtosecond Tm-fiber laser," Optics Express **20**, 7046–7053 (2012).

116. P. Maine, D. Strickland, P. Bado, M. Pessot, and G. Mourou, "Generation of ultrahigh peak power pulses by chirped pulse amplification," IEEE Journal of Quantum Electronics **24**, 398–403 (1988).

117. J. Limpert, F. R, D. N. Schimpf, E. Seise, T. Eidam, S. H, and J. Rothhardt, "High Repetition Rate Gigawatt Peak Power Fiber Laser Systems : Challenges , Design , and Experiment," IEEE J. of Sel. Top. Quantum Electron. **15**, 159–169 (2009).

118. F. Haxsen, D. Wandt, U. Morgner, J. Neumann, and D. Kracht, "Pulse energy of 151 nJ from ultrafast thulium-doped chirped-pulse fiber amplifier," Optics Letters **35**, 2991–3 (2010).

119. L.-M. Yang, P. Wan, V. Protopopov, and J. Liu, "2 μm femtosecond fiber laser at low repetition rate and high pulse energy," Optics Express **20**, 5683–5688 (2012).

120. O. E. Martinez, "3000 Times Grating Compressor with Positive Group Velocity Dispersion : Application to Fiber compensation in 1.3-1.6 um region," Quantum Electronics, IEEE Journal of **23**, 59–64 (1987).

121. E. Treacy, "Optical pulse compression with diffraction gratings," Quantum Electronics, IEEE Journal of **5**, 454–458 (1969).

122. F. Ouellette, "Dispersion cancellation using linearly chirped Bragg grating filters in optical waveguides.," Optics letters **12**, 847–9 (1987).

123. K.-H. Liao, M.-Y. Cheng, E. Flecher, V. I. Smirnov, L. B. Glebov, and A. Galvanauskas, "Large-aperture chirped volume Bragg grating based fiber CPA system.," Optics express **15**, 4876–82 (2007).

124. K. O. Hill, F. Bilodeau, B. Malo, T. Kitagawa, S. Thériault, D. C. Johnson, J. Albert, and K. Takiguchi, "Chirped in-fiber Bragg gratings for compensation of optical-fiber dispersion.," Optics letters **19**, 1314–6 (1994).

125. R. A. Sims, P. Kadwani, L. Shah, and M. Richardson, "Generation and amplification of femtosecond pulses in Tm:fiber," in *Laser Technology for Defense and Security VII*, M. Dubinskii and S. G. Post, eds. (SPIE, 2011), Vol. 7914, p. 80390K.

126. S. Kivisto, T. Hakulinen, M. Guina, and O. G. Okhotnikov, "Tunable Raman soliton source using mode-locked Tm-Ho fiber laser," IEEE Photon. Technol. Lett **vol**, 19no12pp934–936 (n.d.).

127. R. Sims, P. Kadwani, L. Shah, and M. Richardson, "All Thulium Fiber CPA System with 107 fs Pulse Duration and 42 nm Bandwidth," in *Advanced Solid-State Photonics* (Optical Society of America, 2011), p. ATuD4.

128. R. A. Sims, P. Kadwani, L. Shah, and M. Richardson, "182 nJ All Thulium Fiber CPA System," in *CLEO:2011 - Laser Applications to Photonic Applications* (Optical Society of America, 2011), p. JWA31.

129. D. N. Papadopoulos, Y. Zaouter, M. Hanna, F. Druon, E. Mottay, E. Cormier, and P. Georges, "Generation of 63 fs 4.1 MW peak power pulses from a parabolic fiber amplifier operated beyond the gain bandwidth limit.," Optics letters **32**, 2520–2 (2007).

130. R. A. Sims, P. Kadwani, H. Ebendorff-Heidepriem, L. Shah, T. M. Monro, and M. Richardson, "Chirped pulse amplification in single mode Tm:fiber using a chirped Bragg grating," Applied Physics B: Lasers and Optics (2012).

131. A. D. Yablon, *Optical Fiber Fusion Splicing* (Springer, 2005).

132. L. E. Hooper, P. J. Mosley, a C. Muir, W. J. Wadsworth, and J. C. Knight, "Coherent supercontinuum generation in photonic crystal fiber with all-normal group velocity dispersion.," Optics express **19**, 4902–7 (2011).

133. J. M. Dudley and S. Coen, "Coherence properties of supercontinuum spectra generated in photonic crystal and tapered optical fibers.," Optics letters **27**, 1180–2 (2002).

134. A. Heidt, "Pulse preserving flat-top supercontinuum generation in all-normal dispersion photonic crystal fibers," Journal of the Optical Society of America B **27**, 550–559 (2010).

135. A. Ruehl, M. Martin, K. Cossel, L. Chen, H. McKay, B. Thomas, C. Benko, L. Dong, J. Dudley, M. Fermann, I. Hartl, and J. Ye, "Ultrabroadband coherent supercontinuum frequency comb," Physical Review A **84**, 3–6 (2011).

136. H. Ebendorff-Heidepriem, K. Kuan, M. R. Oermann, K. Knight, and T. M. Monro, "Extruded tellurite glass and fibers with low OH content for mid-infrared applications," Optical Materials Express **2**, 432 (2012).

137. D. Buccoliero, H. Steffensen, O. Bang, H. Ebendorff-Heidepriem, and T. M. Monro, "Thulium pumped high power supercontinuum in loss-determined optimum lengths of tellurite photonic crystal fiber," Applied Physics Letters **97**, 061106 (2010).

138. S. Shabahang, M. P. Marquez, G. Tao, M. U. Piracha, and D. Nguyen, "Octave-spanning infrared supercontinuum generation in robust chalcogenide nanotapers using picosecond pulses," **37**, 4639–4641 (2012).

139. G. Tao, S. Shabahang, E.-H. Banaei, J. J. Kaufman, and A. F. Abouraddy, "Multimaterial preform coextrusion for robust chalcogenide optical fibers and tapers.," Optics letters **37**, 2751–3 (2012).